

4-22-2013

Orbital Debris Removal Technologies: A Hybrid Electrodynamic Tether and Ion Beam Shepherd Satellite Design for Fuel Efficient Contactless Debris Removal

Jorn Mumme

Embry-Riddle Aeronautical University - Daytona Beach

Follow this and additional works at: <https://commons.erau.edu/edt>



Part of the [Aerospace Engineering Commons](#)

Scholarly Commons Citation

Mumme, Jorn, "Orbital Debris Removal Technologies: A Hybrid Electrodynamic Tether and Ion Beam Shepherd Satellite Design for Fuel Efficient Contactless Debris Removal" (2013). *Dissertations and Theses*. 108.

<https://commons.erau.edu/edt/108>

This Thesis - Open Access is brought to you for free and open access by Scholarly Commons. It has been accepted for inclusion in Dissertations and Theses by an authorized administrator of Scholarly Commons. For more information, please contact commons@erau.edu.

**ORBITAL DEBRIS REMOVAL TECHNOLOGIES: A HYBRID
ELECTRODYNAMIC TETHER AND ION BEAM SHEPHERD
SATELLITE DESIGN FOR FUEL EFFICIENT CONTACTLESS DEBRIS
REMOVAL**

THESIS

**Presented to the MSEP Graduate Committee
Of Embry-Riddle Aeronautical University
In Partial Fulfillment of the Requirements**

For the Degree of

Master of Science in Engineering Physics

By

JÖRN MUMME B.S. IN AEROSPACE ENGINEERING

**Daytona Beach
April 22, 2013**

Copyright by Jörn Mumme 2013, All rights reserved.

ORBITAL DEBRIS REMOVAL TECHNOLOGIES:
A HYBRID ELECTRODYNAMIC TETHER AND ION BEAM SHEPHARD
SATELLITE DESIGN FOR FUEL EFFICIENT CONTACTLESS DEBRIS
REMOVAL

by

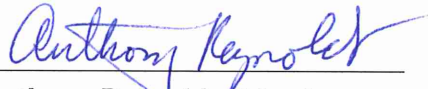
JÖRN MUMME

This thesis was prepared under the direction of the candidate's thesis committee chair,
Dr. Aroh Barjatya, Department of Physical Sciences, and has been approved by the
members of his thesis committee. It was submitted to the Department of Physical
Sciences and was accepted in partial fulfillment of the requirements for the Degree of
Master of Science in Engineering Physics

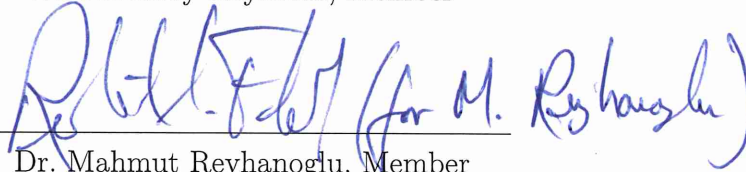
THESIS COMMITTEE:



Dr. Aroh Barjatya, Chair



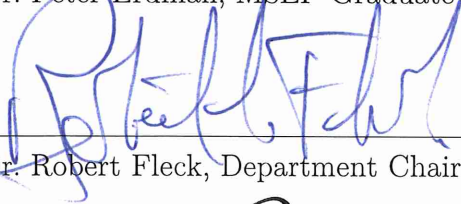
Dr. Anthony Reynolds, Member



Dr. Mahmut Reyhanoglu, Member



Dr. Peter Erdman, MSEP Graduate Program Coordinator



Dr. Robert Fleck, Department Chair, Physical Sciences



Dr. Robert Oxley, Associate V.P. for Academics

4-29-13

Date

Abstract

Space debris poses a serious threat to humanities efforts at space exploration as well as the expanding uses for earth-orbiting satellites. This thesis investigates the proposed technologies for the debris's removal both large and small. Focus is applied to the large debris removal technologies since the small size category is dominated by the ORION laser system. Furthermore, the large debris objects pose the most destructive threat upon impact to satellites. Electrodynamic tethers (EDT) as well as their control strategies, ion-beam shepherds (IBS), and tradition thruster methods are investigated for effectiveness and feasibility. Hybrid combinations of these technologies are investigated in hopes of reducing time and cost of the de-orbiting mission. A new control strategy for the EDT is outlined which is used for orbital rendezvous with debris. Results show that a hybrid technology between EDT and IBS far outperforms the individual technologies of similar mass as it utilizes the strengths of both in order to overcome each of their weaknesses. Furthermore, scaling down the hybrid system to 200kg total mass to avoid parasite fuel mass could potentially increase the effectiveness to de-orbit six large debris pieces within 200 days. Possible ion-beam plasma instabilities are hypothesized, but not investigated and are recommended for further research. A full systems analysis is recommended to determine a feasible dry mass, which can then lead to more accurate simulation results.

Acknowledgements

I would like to thank Embry-Riddle Aeronautical University for providing me with a world-class education in aerospace engineering and engineering physics. I would also like to thank my advisor, Dr. Aroh Barjatya, for his guidance in preparing this thesis. I would like to thank my classmates including Dominic Seremet, Thomas Moore, and Cody Chambers for making my graduate school a more fulfilled life experience. Lastly, even though we were separated by a large distance, I would like to thank my parents for their continued support and for giving me the opportunity of a lifetime: to pursue my dreams.

Table of Contents

1. Introduction	1
1.1 History of Space Debris: The Space Surveillance Network (SSN).....	2
1.2 Political Efforts.....	5
1.3 Debris Physical Characteristics	5
1.4 Debris Altitude Distribution and Evolution.....	12
1.5 Thesis Overview	22
2. Orbital Debris Removal Technologies.....	27
2.1 Orion Laser	27
2.1.1 Technical Aspects of Operation.....	29
2.1.2 Implementation.....	34
2.1.3 Advantages	37
2.1.4 Disadvantages	37
2.2 Electrodynamic Tether	38
2.2.1 Technical Aspects of Operation.....	38
2.2.2 Implementation.....	45
2.2.3 Advantages	49
2.2.4 Disadvantages	50
2.3 Dust Cloud	51
2.3.1 Technical Aspects of Operation.....	52
2.3.2 Implementation.....	53
2.3.3 Advantages	54
2.3.3 Disadvantages	55
2.4 Ion Beam Shepherd	55
2.4.1 Technical Aspects of Operation.....	56
2.4.2 Implementation.....	58
2.4.3 Advantages	60

2.4.4	Disadvantages	60
2.5	Satellite Rendezvous with modular de-orbit device.....	61
2.5.1	Technical Aspects of Operation.....	61
2.5.2	Implementation.....	62
2.5.3	Advantages	64
2.5.4	Disadvantages.....	64
3.	Analysis and Design.....	65
3.1	Impulsive Maneuvers.....	65
3.2	Astrodynamics of Satellites with thrust	67
3.3	EDT Forces	69
3.4	EDT Current Laws and Control/Guidance Scheme.....	71
3.4.1	Slewing Maneuver of EDT	73
3.4.2	Position-Optimal EDT orbit rendezvous	76
3.5	Dynamics and fuel costs of de-orbiting debris using an ion beam.....	83
3.6	Ion Beam Physics	88
3.6.1	Ion Beam far-field plume divergence	88
3.6.3	CEX Collisions.....	96
3.6.3	Beam-plasma instabilities.....	102
3.7	State-feedback control system for relative position holding and rendezvous	107
3.7.1	Control system simulation results using LQR gain matrix.....	113
3.7.2	Control system simulation results using $H\infty$ gain matrix.....	117
3.8	Attitude Control.....	119
3.9	Active debris removal technology tradeoff simulation results.....	127
3.9.1	Descent Rate and Fuel Burn for varying debris size and altitude.....	127
3.9.2	Multiple debris object de-orbit mission analysis.....	134
3.10	Proposed Small Satellite using Ion Beam and Electrodynamic Tether technologies	

4. Summary148
Works Referenced.....153

Table of Figures

Figure 1: USSTRATCOM's Space Surveillance Network from the NASA-Handbook 8719.14 [2]. This figure illustrates the global effort and capability distributed amongst different partnering nations around the globe..... 3

Figure 2: Flux Comparison between multiple radars at an altitude of 600-800km[3]. The x-axis represents the statistically average diameter of the debris, and the y-axis represents the cummalitve flux of the debris. The flux of the debris is a metric used to measure the debris population..... 4

Figure 3: Debris flux in $1/m^2/yr$ at varying debris diameters in the ISS's orbit using ORDEM2010 (NASA)..... 6

Figure 4: "The feature measures $\sim 5mm$ in diameter and was located on a ram-facing portion of an aluminum Z-frame that was covered with a Teflon layer [9]." Ram-Facing implies the Z-frame's surface was perpendicular to the velocity vector..... 8

Figure 5: Critical object diameter with respect to impact velocity for single and double wall thickness [8]. 11

Figure 6: ISS risk reduction due to change in attitude using BUMPER-II [10]. 12

Figure 7: Current Spatial Density distribution from MASTER-2009 (ESA). The black curve is a sum of all the different debris population constituents, and each colored line underneath this curve represents the debris population for a specific type of debris defined in the legend below the figure. 13

Figure 8: Average Spatial density at varying altitudes and the critical density. The debris population is said to be unstable where the average critical density $>$ actual density. An unstable debris population implies that the frequency of collisions is so high that the rate at which the existing population collides with itself to produce more debris is greater than the rate at which the existing population descends into a terminal orbit. This results in an exponentially growing debris population. This figure was reproduced from Kessler (1991) [11]..... 16

Figure 9: Adjusted Critical Spatial density at varying altitudes and the critical density. The debris population is said to be unstable where the adjusted critical density $>$ actual density. This figure was reproduced from Kessler (1991) [11]. 17

Figure 10: The LEO debris environment in 2007 and 2010; the Iridium and Fengyun-1C incidents contribute the majority of the change [14]. 18

Figure 11: ADR 5, 10, and 20 objects per year [16].	21
Figure 12: Optimal Coupling Intensity [18]. On a Log-Log scale the coupling coefficient, a measure of the efficiency of the momentum transfer, is related to the laser intensity reaching a maximum peak value at around $2.4E8 \text{ W/cm}^2$. The pulse width is kept to 22ns at a wavelength of 248nm. The functions of the coupling coefficient to the laser intensity either side of the peak are given by the two formulas near the bottom of the figure.	30
Figure 13: Optimal Incident Fluence for varying pulse widths [18]. This figure shows that the incident fluence is a function of pulse duration, which in turn will affect the optimal coupling coefficient; making this a 2 variable optimization problem to find the most efficient combination of laser intensity and incident fluence.	31
Figure 14: EDT Double-strand configuration.	45
Figure 15: EDT Mission Phases.	46
Figure 16: Round trip time for variable tether length during orbit-rise phase for Globalstar and ADEOS spacecraft.	48
Figure 17: In-Plane tether angle vs. angle propagation in the earth frame.	48
Figure 18: Tension in the tether for Case D vs. angle propagation in earth frame.	49
Figure 19: Debris impact on a Hubble Space Telescope Antenna resulting from an object of diameter $<1\text{cm}$ [23].	51
Figure 20: Dust cloud in polar orbit surrounding the orbital debris, acting as a 'snow plow' lowering the altitude of the debris [23].	54
Figure 21: Ion Beam Shepherd (IBS) Operational Concepts [19].	57
Figure 22: Time required for a transfer of varying debris masses from 1000km to 300km [19]. The force (x-axis) is related to the IBS mass as can be seen below in Figure 24.	59
Figure 23: IBS mass for varying thrust and debris masses for a de-orbit from 1000km to 300km [19]. The time required for the force-mass configuration can be obtained from Figure 22.	59
Figure 24: Operational objectives of the rendezvous satellite [25].	61
Figure 25: Spacecraft design. 1: Debris 2: Nozzle extension 3: Expanding Umbrella 4: Thruster 5: Front Arm 6: Rear Arm.	62
Figure 26: Spacecraft mass as objects are removed from orbit.	63
Figure 27: Satellite coordinate system and variable definition for flexible appendage slewing maneuver.	73

Figure 28: EDT Tip coordinate and EDT base angle with respect to time for a 90 degree slewing maneuver	75
Figure 29: EDT current control scheme.....	78
Figure 30: Sample simulation of the current control laws for a change in the semi-major axis of -2km and a time step of 10 seconds.....	80
Figure 31: Sample test of the current control laws for an inclination change of -0.1 degrees and a time step of 1 second.....	81
Figure 32: EDT Rendezvous Control Strategy.	82
Figure 33: Parks and Katz model of far-field plume divergence via MATLAB simulation.	91
Figure 34: Ion density cross section at $z=0$	93
Figure 35: Ion density cross section at $z=5m$	93
Figure 36: 2 sigma radius vs. axial distance of the plume.	94
Figure 37: Neutral Density Profile.....	99
Figure 38: Ratio of Ion Densities with CEX to without CEX.	100
Figure 39: CEX density with respect to axial distance at $r=0$	101
Figure 40: Two-stream instability initial conditions [39].	102
Figure 41: Dispersion relation for the two-stream instability [39].	103
Figure 42: beam driven ion-acoustic-unstable velocity space distribution [40].	104
Figure 43: Ion-beam plasma instability ($t=120/wp_0$), $m_i/m_e=1000$, $L=3$ wavelengths [42].	105
Figure 44: IBS-Debris problem formulation [44].	108
Figure 45: Simulink block diagram for state-feedback system using LQR for relative spacecraft position control.	112
Figure 46: 3-component response for the state-feedback control system using the LQR gain matrix.....	115
Figure 47: 3-component thruster force response for the state-feedback control system using the LQR gain matrix.....	115
Figure 48: Cumulative fuel mass consumption for the controller using the LQR gain matrix.....	116
Figure 49: 3-D path of chaser satellite relative to target satellite (red) using the LQR gain matrix.....	116

Figure 50: 2-D path of chaser satellite relative to target satellite (red) using the LQR gain matrix.....	116
Figure 51: 3-component response for the state-feedback control system using the H^∞ gain matrix.....	117
Figure 52: 3-component thruster force response for the state-feedback control system using the H^∞ gain matrix.....	118
Figure 53: Cumulative fuel mass consumption for the controller using the H^∞ gain matrix.....	118
Figure 54: 3-D path of chaser satellite relative to target satellite (red) using the H^∞ gain matrix.....	119
Figure 55: 2-D path of chaser satellite relative to target satellite (red) using the H^∞ gain matrix.....	119
Figure 56: Unstable gravity gradient configuration.	123
Figure 57: Gravity Gradient Torques.	123
Figure 58: SC Euler angles with active attitude control.....	124
Figure 59: SC Momentum wheel angular momentum.....	124
Figure 60: SC Momentum wheel RPM.	125
Figure 61: Libration angles without control [48].....	126
Figure 62: Libration angles with active on-off switch control [48].....	126
Figure 63: Propellant mass required to de-orbit orbital debris of different masses from a series of orbital altitudes to a perigee of 200km using instantaneous thrusters.....	128
Figure 64: Time required de-orbiting debris from varying altitudes. This plot is independent of debris mass because the maneuvers are 'impulsive' and therefore share an instantaneous common transfer orbit to 200km perigee.	128
Figure 65: Propellant mass required to de-orbit orbital debris of different masses from a series of orbital altitudes to a perigee of 200km using an Ion Beam with constant thrust of 200mN.....	129
Figure 66: Time required de-orbiting orbital debris of different masses from a series of orbital altitudes to a perigee of 200km using an Ion Beam with constant thrust of 200mN.	130
Figure 67: Time required to de-orbit orbital debris of different masses from a series of orbital altitudes to a perigee of 200km using an Electrodynamic Tether of length 5km and max current of 5 amps.	131

Figure 68: Propellant mass required to de-orbit debris of varying mass from an orbit of 1000km to a perigee of 200km using the three technologies.132

Figure 69: Time required to de-orbit debris of varying mass from an orbit of 1000km to a perigee of 200km using the three technologies.133

Figure 70: Rendezvous mission algorithm.....137

Figure 71: Spacecraft mass vs. waypoint number comparing the different technology combinations.138

Figure 72: Perigee and inclination evolution over time for the EDT+Ion Beam System.141

Figure 73: A breakdown of the orbital maneuvers.....141

Figure 74: Spacecraft mass varying over time.143

Figure 75: Spacecraft mass vs. waypoint for EDT+IBS system assuming $m_0=200\text{kg}$144

Figure 76: Spacecraft mass vs. time for EDT+IBS system assuming $m_0=200\text{kg}$145

Figure 77: Spacecraft mass vs. time for EDT+IBS system assuming $m_0=200\text{kg}$ for 5km, 10km, and 15km tether lengths.....146

Chapter 1

Introduction

In an effort to further explore our universe, mankind has been undertaking endeavors into space starting with the 1957 launch of Sputnik-1. Much progress has been made in the recent decades, including manned spaceflight resulting in over 4000 rocket launches [1]. Amongst all of our achievements, however, we have neglected to address a sleeping giant in the world of hazards for space missions: orbital debris. The earth is surrounded by many forms of natural orbital debris such as meteoroids; however, there is also an ever-growing amount of manmade debris orbiting the earth. This debris forms a self-colliding medium consisting of old rocket boosters, old spacecraft, parts resulting from spacecraft collisions, etc. We know that this threat exists; however, we are still unaware of when this threat will become an economical problem for earth's space exploration, how to remove the current debris, and how to prevent future debris from forming. The economics of the situation is a very complicated and still underdeveloped field since most technologies proposed are experimental and estimating a cost metric is purely hypothetical. On the other hand, political measures have been taken to establish international rules to increase awareness and hopefully prevent future collisions. Therefore, this report will focus on investigating current orbital debris removal

technologies, outlining their limitations and finally proposing a new resource-effective and low-risk method for orbital debris removal.

The most logical place to start when analyzing any technology would be the purpose; what problem is it trying to fix? Therefore, the subsequent sections of this chapter outline the history of the space debris problem, why space debris poses a threat to spacecraft missions, as well as the characteristics of the space debris environment and how it is simulated for current and future scenarios. Thereafter, this chapter concludes with an outline for the remainder of the thesis based on addressing the technological aspects of the National Research Council's 2011 findings and recommendations for NASA's orbital debris program.

1.1 History of Space Debris: The Space Surveillance Network (SSN)

Since 1959, the United States Strategic Command (USSTRATCOM) has been tracking satellites using the SSN. The SSN, shown in Figure 1, consists of several radars and optical telescopes worldwide dedicated to discovering and tracking orbital debris.

In order to detect debris as small as 2 mm in diameter, three main radars have been used: JPL Goldstone Deep Space Network, MIT Haystack LRIR, and the MIT HAX where each radar is specifically tuned for a certain altitude region.

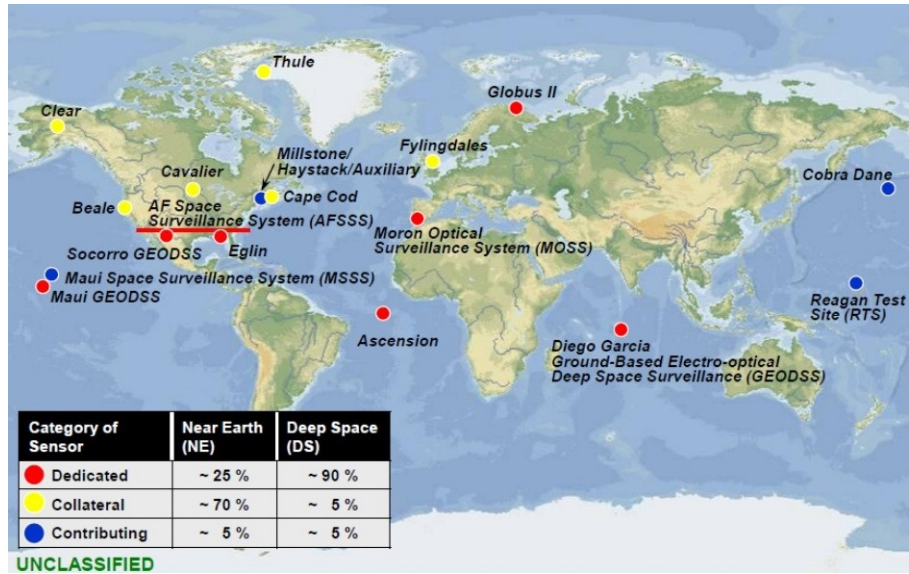


Figure 1: USSTRATCOM's Space Surveillance Network from the NASA-Handbook 8719.14 [2]. This figure illustrates the global effort and capability distributed amongst different partnering nations around the globe.

The Goldstone radar observes objects between 300km and 3200km, and the Haystack/HAX radars usually detect within the altitude region of 350km to 1800km. Each radar's observations vary slightly but can be averaged using statistical analysis to provide insight on the debris populations. Figure 2 shows a sample comparison between the radars between the ranges of 600-800km for 2001. Very small debris particles, such as paint flakes are very hard to track with current technology and are therefore mostly unaccounted for.

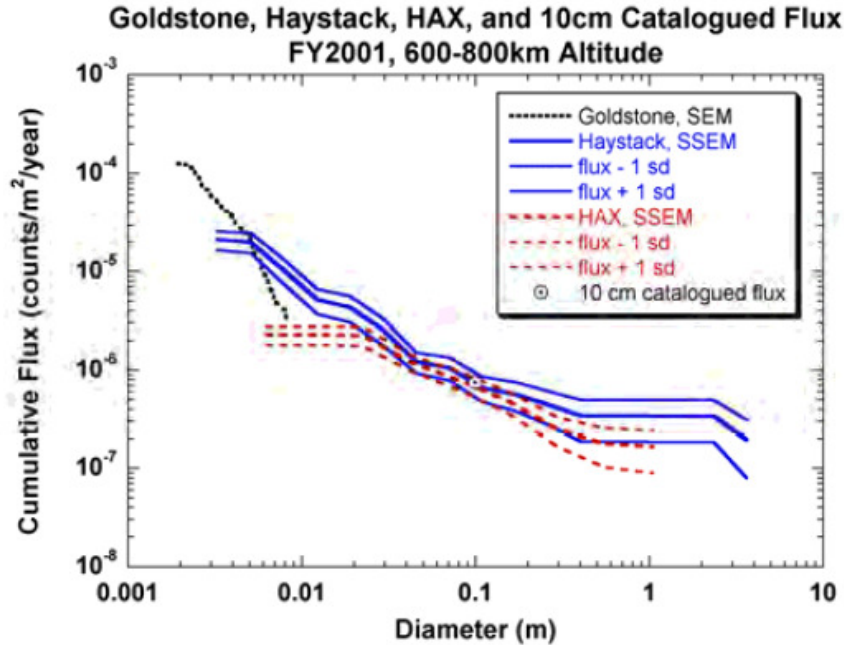


Figure 2: Flux Comparison between multiple radars at an altitude of 600-800km [3]. The x-axis represents the statistically average diameter of the debris, and the y-axis represents the cummalitve flux of the debris. The flux of the debris is a metric used to measure the debris population.

The statistical average of the number of particles, their size, velocities, and trajectories are continuously recorded and tracked to provide the best overall discrete data set for the orbital debris environment. This information can then be fed into software developed especially for assessing mission risk to orbital debris such as NASA's Orbital Debris Engineering Model (ORDEM) or ESA's Meteoroid and Space Debris Terrestrial Environment Reference (MASTER). For further detail on the ORDEM model please refer to Krisko (2010) [4].

1.2 Political Efforts

In order to prevent future debris impact events, the IADC (Inter-Agency Space Debris Coordination Committee) has published guidelines in 2002 on space debris operations. The IADC guidelines outline concepts such as post-mission disposal, preventing on-orbit collisions, and minimizing the potential for breakups during normal operations. However, all of the efforts put forth by the IADC are still subject to political subjectivity, making them truly ‘guidelines’ rather than ‘rules’. However, political pressure due to the growing awareness of the orbital debris problem will hopefully solidify these guidelines so that further introduction of debris into the environment can be minimized.

1.3 Debris Physical Characteristics

The debris itself can be categorized into three main sizes with corresponding potential risk and number of objects, shown in Table 1. Figure 3 illustrates the flux distribution for the ISS orbiting at a mean altitude of 387.4km [4] using the ORDEM2010 model.

The question remains of how much of a threat these debris particles pose. Therefore, NASA launched the Long Duration Exposure Facility (LDEF) in 1984, with a lifetime of 69 months, to investigate the potential dangers from small sized debris impacts as well as other aspects of the space environment.

Table 1: Debris size classification, number, and potential damage [5], giving an introductory insight into the relative size and quantity of debris as well as their impact.

Size	Number of objects	Potential risk to satellites
>10cm	19,000+	Complete destruction
1-10cm	Several hundred thousand	Complete to partial destruction
< 1cm	Several hundred million	Degradation, loss of certain sensors or subsystems

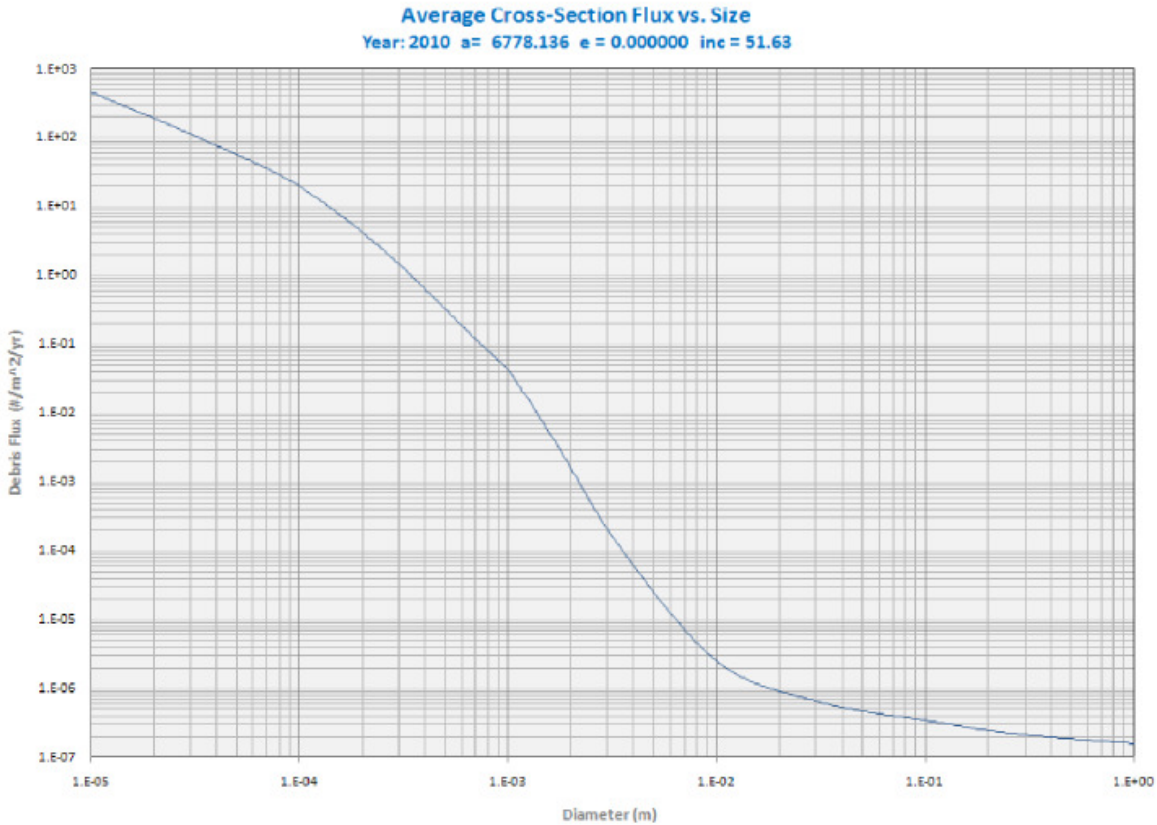


Figure 3: Debris flux in 1/m²/yr at varying debris diameters in the ISS's orbit using ORDEM2010 (NASA).

The LDEF was a gravity gradient stabilized spacecraft with a viscous damper so that one side of the spacecraft was always facing in the direction of the velocity vector. An interesting finding from the LDEF was that more than 30% of the impacts on the trailing edge of the spacecraft were from debris, implying that there is a large population of debris in highly elliptical orbits [6] [7].

More than 34,000 impacts were investigated ranging in size from 50 μ m to 0.57cm, and have lead to empirical formulas to determine crater size based on impact velocity, angle, and size [6]. Figure 4 shows the largest impact crater from the LDEF with a diameter of about 0.5 cm, showing the reality of impact threats to space systems.

Impacts from objects such as this pose a serious threat to subsystem components resulting in damage or failure. The methods used to deduce the damage of orbital debris are briefly outlined below to help bring a numerical significance to the effect of debris impacts. To help design spacecrafts to withstand these impacts, the maximum survivable critical projectile diameter for a single sheet of monolithic material is given by Equation 1.1, where the appropriate constants vary by author and are outlined in Table 2 [8]. Debris flux simulations, such as those in Figure 3, along with Equation 1.1 can help determine the thickness of the shielding material such that the critical diameter falls above the probable exposed flux diameter. However, it should be noted that these efforts are for small debris only. In the case of large debris (>1m) colliding with a satellite, there

is going to be catastrophic damage regardless of the shielding material. In fact, if the particle diameter is greater than

$$d_p \leq d_{p,lim} = \left[\frac{t_t}{K_1 \rho_p^\beta \rho_t^k v_p^\gamma (\cos \alpha_p)^\xi} \right]^{\frac{1}{\lambda}} \quad (1.1)$$

the collision could be catastrophic [8] where d_p is the particle diameter, $d_{p,lim}$ is the catastrophic diameter limit, t_t is the wall thickness, and the rest of the variables are constants defined in Table 2.

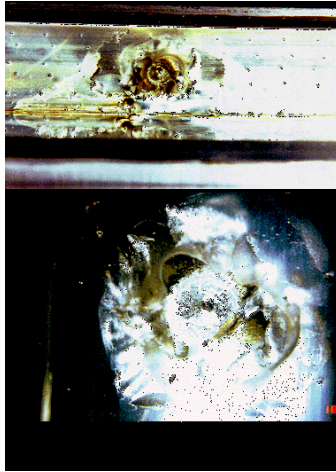


Figure 4: "The feature measures ~5mm in diameter and was located on a ram-facing portion of an aluminum Z-frame that was covered with a Teflon layer [9]." Ram-Facing implies the Z-frame's surface was perpendicular to the velocity vector.

Table 2: Parameters for critical debris diameter equations from different sources and targets [8].

Equation	Target	K_1						
ESA	Thick plate	0.36-0.99	1.056	0.519	2/3	2/3	0	
ESA	Thin plate	0.26-0.64	1.056	0.519	0.875	0.875	0	
Pailer & Gruen	Any	0.77	1.212	0.737	0.875	0.875	-0.5	
Frost	Any	0.43	1.056	0.519	0.875	0.875	0	
Naumann et al.	Any	0.65	1.056	0.5	0.875	0.875	-0.5	
Naumann	Any	0.326	1.056	0.499	2/3	2/3	0	
McHugh et al.	Thick glass	1.18-4.48	1.2	0	2/3	2/3	0.5	
Cour-Palais	Thick glass	0.98-3.17	1.06	0.5	2/3	2/3	0	

Using formula 1.1 for maximum debris impact diameter, a probability of survivability can be calculated, denoted Probability of No Penetration (P_{PNP}), using the impact flux of critical debris diameters, the collision cross section A of the target, and the exposure time based on Poisson Statistics.

$$P_{PNP} = \exp(-F(d \geq d_{p,lim})A\Delta t) \quad (1.2)$$

where $F(d \geq d_{p,lim})$ is the flux of debris particles with diameter less than the catastrophic limit, A is the collision cross sectional area, and Δt is the exposure time.

The probability of failure or risk denoted $P_{n \geq 1}$, is then simply calculated by the compliment of this probability

$$P_{n \geq 1} = 1 - P_{PNP} \quad (1.3)$$

This analysis is simplistic in the fact that it is only one material type of one given thickness, and for a complex spacecraft all components must be taken into consideration. Similar equations can be developed for complex wall configurations such as honeycomb, ceramic, and bumper configurations. The trends for single and double wall configurations are shown in Figure 5.

Given that different surfaces of the spacecraft will yield different critical diameters, and the spacecraft is not necessarily in a constant attitude, and different attitudes expose different surfaces, finite element analysis has to be done over the entire surface of the spacecraft to be able to determine overall mission risk. NASA and ESA use software (BUMPER-II and DRAMA respectively) to analyze complex space missions, which has resulted in a change of the mated attitude of the space shuttle after STS-107 to reduce the critical penetration risk from 1 in 78 to 1 in 151, shown in Figure 6.

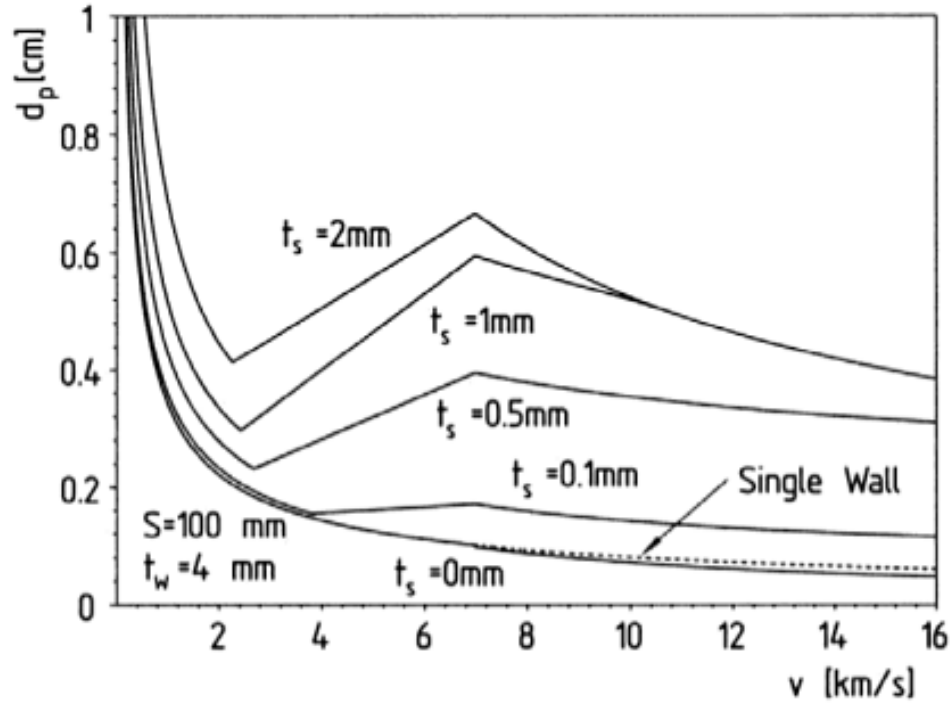


Figure 5: Critical object diameter with respect to impact velocity for single and double wall thickness [8].

According to the single wall equation given in Equation 1.1 and Figure 5, we can see that the velocity and the critical diameter of impacting debris are inversely proportional and asymptotic to 0. This makes sense since the energy of the impact is related to both the mass and velocity, which can in turn be related to the diameter and velocity making an assumption of average density. Therefore, assuming that the critical energy of the impact is defined as a constant value, and the velocity of the impacting particle increases, the diameter of the impacting debris must be smaller in order to conserve the impact energy at the critical value.

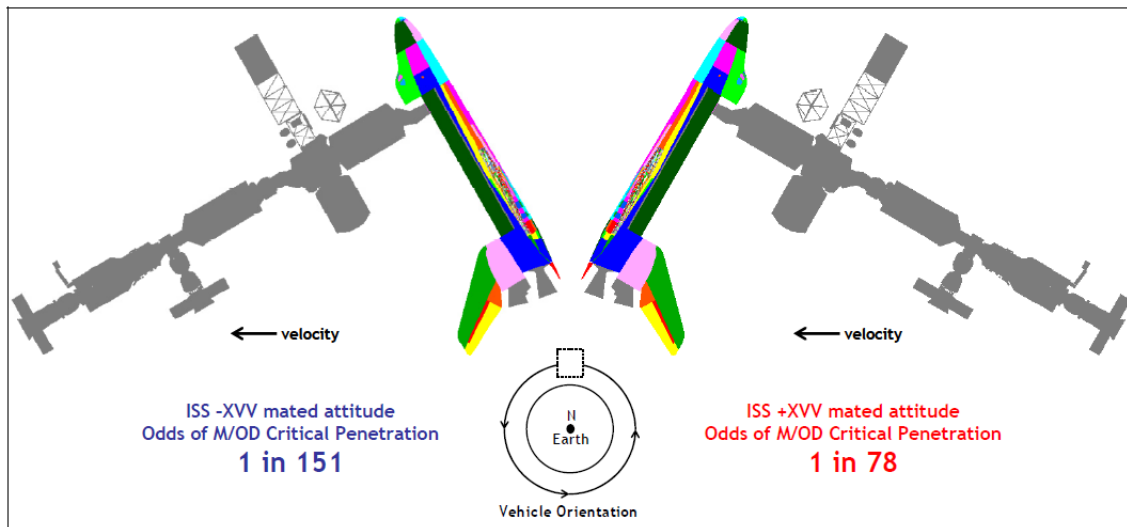


Figure 6: ISS risk reduction due to change in attitude using BUMPER-II [10].

The effects of debris impacts can be seen to be remarkably significant, as shown in Figure 4, and thanks to BUMPER-II and DRAMA we can help spacecraft survive in a small-debris environment. Even though this is not a solution for large debris impacts, this is a great step towards dealing with the problem since the majority of space debris is in the small category, which will be outlined in the following section.

1.4 Debris Altitude Distribution and Evolution

Several modern programs exist that use statistically known data and tracking of large debris objects in order to obtain a reasonable estimate of the debris flux for a given diameter at given orbital parameters. To obtain a more general picture of *where* the

debris are located, the debris fluxes at varying orbital parameters such as inclination and eccentricity can be averaged to obtain a profile solely dependent on the altitude of the orbit. This yields plots such as Figure 7 which can be useful when discussing design criteria for removal missions since it helps us define an operating altitude. Unfortunately, the orbital debris environment is not inherently stable; it depends on the spatial density of the current debris, similar to a typical population growth

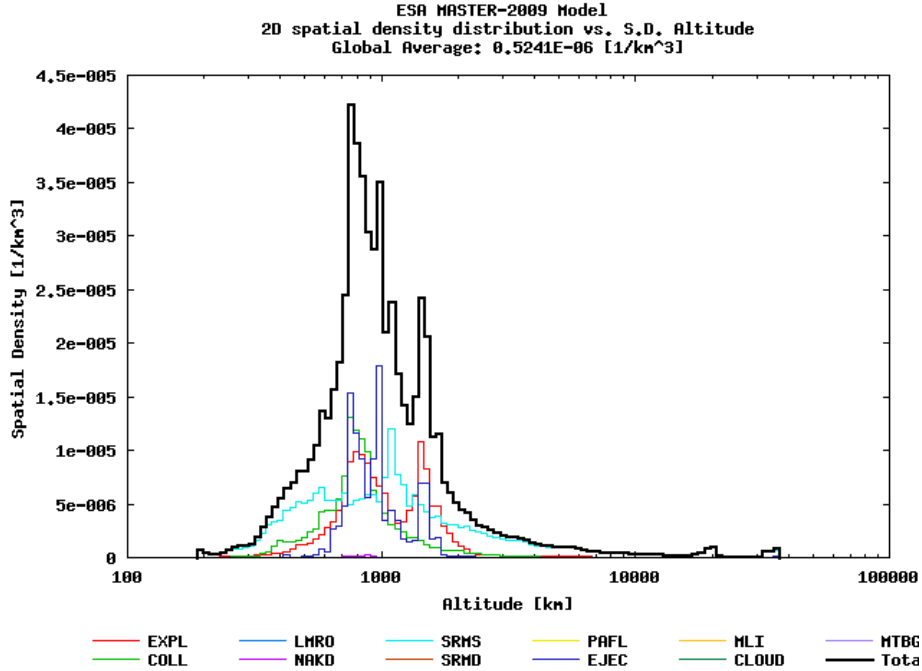


Figure 7: Current Spatial Density distribution from MASTER-2009 (ESA). The black curve is a sum of all the different debris population constituents, and each colored line underneath this curve represents the debris population for a specific type of debris defined in the legend below the figure.

problem. Kessler first predicted the scenario of a self-colliding orbital debris environment in 1991.

"By definition, a critical population density is reached when that population will produce fragments from random collisions at an increasing rate and at a rate that is greater than the rate of removal by natural processes." [11]

To show mathematical details on the evolution of the space debris problem, which in turn stresses its urgency, Kessler's evolution formulae and major recent growth events are outlined below.

The satellite breakup rate due to random collisions ($\frac{dB}{dt}$) is a function of spatial density and is given by

$$\frac{dB}{dt} = \frac{1}{2} S^2 V \sigma \Delta U = \sum_{i=1}^N \sum_{j=i+1}^{n-1} \int_{Volume} S_i S_j V_{ij} \sigma_{ij} dU \quad (1.4)$$

where B is the total number of satellite breakups, S_i is the spatial density of the i^{th} object, S_j is the spatial density of the j^{th} object, N is the total number of objects in orbit, n is the subset of N that excludes $N = i$, V_{ij} is the relative velocity between the two objects, and σ_{ij} is the collision cross section between the two objects in the volume differential element dU . Using satellite dimensions obtained from catalogued objects and radar cross section, a collision rate can be calculated by computing the appropriate sums.

After a collision occurs, some of the resulting fragments transition into higher orbits and some transition into lower orbits, causing the decay in spatial density ($S_B(t)$) at the break-up altitude to be expressed as

$$S_B(t) = \frac{S_0 \left(e^{-\frac{t}{\tau_1}} + e^{-\frac{t}{\tau_2}} \right)}{2} \quad (1.5)$$

where S_0 is the initial spatial density at the time of breakup, t is time, and τ_1 and τ_2 are constants that are controlled by the atmospheric density at the breakup altitude and the atmospheric density at the altitude of interest respectively. Assuming, each mean-life is approximately inversely proportional to the atmospheric density at the breakup altitude, then the equilibrium spatial density of the breakup fragments (\bar{S}_B) is given by

$$\bar{S}_B = \frac{dB}{dt} \frac{\bar{N}_0}{\Delta U} \tau \quad (1.6)$$

simplifying and assuming that half of the catalogued objects are intact and half are breakup fragments yields the average critical density (S)

$$S = \frac{1}{V\tau\sigma\bar{N}_0} \quad (1.7)$$

where V is a chosen volume element, σ is the collision cross section, and \bar{N}_0 is the average number of particles within the chosen volume element, and τ which is proportional to the atmospheric density at the altitude of interest. This is an average of all of the catalogued objects and their respective altitudes, which yields a function that is a function

of only τ and hence is inversely proportional to the atmospheric density shown in Figure 8.

Equation 1.7, however, assumes that the satellite size and orbital inclination distributions can be averaged over all altitudes, which is not accurate. For example, larger spacecraft are usually launched at lower altitudes. By performing the above calculation for smaller altitude ranges and taking into consideration the satellite size and inclination, the average collision velocity and impact cross section can be calculated as a function of altitude, yielding an adjusted critical spatial density, which is shown in Figure 9.

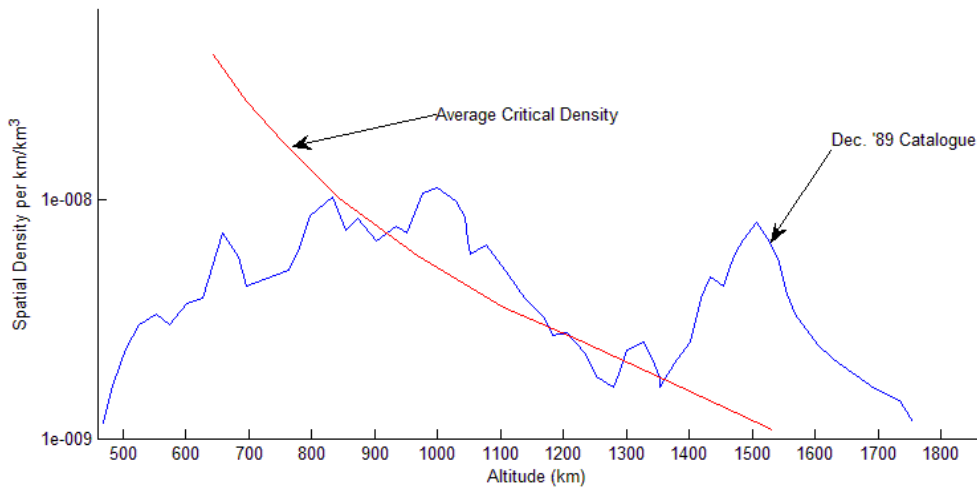


Figure 8: Average Spatial density at varying altitudes and the critical density. The debris population is said to be unstable where the average critical density > actual density. An unstable debris population implies that the frequency of collisions is so high that the rate at which the existing population collides with itself to produce more debris is greater than the rate at which the existing population descends into a terminal orbit. This results in an exponentially growing debris population. This figure was reproduced from Kessler (1991) [11].

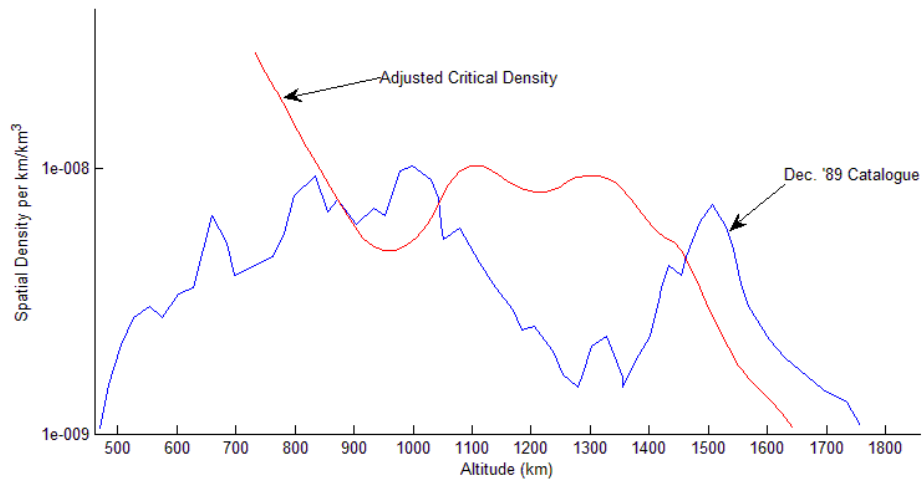


Figure 9: Adjusted Critical Spatial density at varying altitudes and the critical density. The debris population is said to be unstable where the adjusted critical density > actual density. This figure was reproduced from Kessler (1991) [11].

Kessler concluded that the regions of 900-1000km and 1400+km are already unstable in 1991, and that this region of instability will grow if actions are not taken as soon as possible. In addition to the already existing debris growth from collisions, we are introducing more and more debris every year in the form of new manmade satellites. Inherently, as time goes on, the probability of collision between two pieces of debris increases, which can result in events such as the 2009 collision between an Iridium satellite and Cosmos 2251. Furthermore, intentional collisions such as the 2007 destruction of the Fengyun-1C satellite to demonstrate anti-satellite missile technology has created over 2500 orbital debris pieces [12]. These two events are only the most recent

of many on-orbit collisions creating orbital debris and have dramatically changed the LEO environment as can be seen in Figure 10.

In terms of future collisions and their effect on the spacial density of debris, NASA uses the LEGEND tool to predict future debris environments which uses the same collision probability as outlined in Kessler (1991) [11]. After the collision, the generation of new debris was calculated using the NASA standard breakup model and statistical solar activity. If the energy of the collision is greater than or equal to 40J/g then the collision is considered catastrophic [13]. Some of the basic mathematical concepts of LEGEND are demonstrated below for completeness.

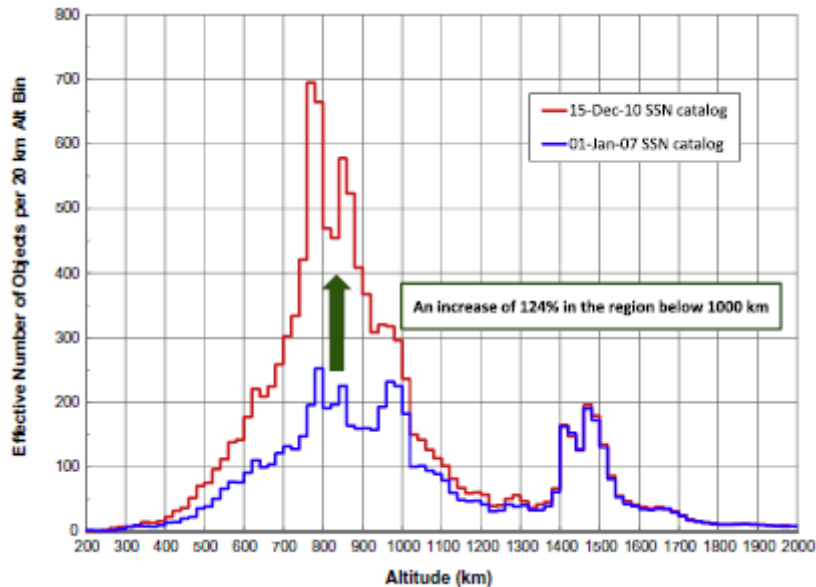


Figure 10: The LEO debris environment in 2007 and 2010; the Iridium and Fengyun-1C incidents contribute the majority of the change [14].

The number of fragments generated from such a collision ($N(Lc)$) is given by

$$N(Lc) = 0.1(M)^{0.75}(Lc)^{-1.71} \quad (1.8)$$

In the case of a catastrophic collision, M is defined as the sum of the two colliding objects' mass in kg and Lc is the characteristic length in meters. In the case of a non-catastrophic collision, M is defined as the product of mass of the smaller object (kg) and the square of the velocity (m/s). For objects smaller than 8cm in diameter, the area to mass ratio distribution function ($D_{\frac{A}{M}}^{SOC}(\lambda_c, x)$) is given by

$$D_{\frac{A}{M}}^{SOC}(\lambda_c, x) = N[x; \mu^{SOC}(\lambda_c), \sigma^{SOC}(\lambda_c)] \quad (1.9)$$

where N is a normal distribution in x about the mean value of μ^{SOC} with standard deviation σ^{SOC} , where λ_c, x, μ^{SOC} , and σ^{SOC} are given by

$$\lambda_c = \log_{10} Lc \quad (1.10)$$

$$x = \log_{10} \frac{A}{M} \quad (1.11)$$

$$\mu^{SOC} = \begin{cases} -0.3 & \lambda_c \leq -1.75 \\ -0.3 - 1.4(\lambda_c + 1.75) & -1.75 \leq \lambda_c < -1.25 \\ -1.0 & \lambda_c \geq -1.25 \end{cases} \quad (1.12)$$

$$\sigma^{SOC} = \begin{cases} 0.2 & \lambda_c \leq -3.5 \\ 0.2 + 0.1333(\lambda_c + 3.5) & \lambda_c > -3.5 \end{cases} \quad (1.13)$$

For upper stage body fragments and spacecraft fragments with an Lc larger than 11cm, the equations respectively become

$$D_{\frac{A}{M}}^R(\lambda_c, x) = \alpha^R(\lambda_c)N[x; \mu_1^R(\lambda_c), \sigma_1^R(\lambda_c)] + (1 - \alpha^R(\lambda_c))N[x; \mu_2^R(\lambda_c), \sigma_2^R(\lambda_c)] \quad (1.14)$$

$$D_{\frac{S}{M}}^{\frac{S}{A}}(\lambda_c, x) = \alpha^{\frac{S}{c}}(\lambda_c)N\left[x; \mu_1^{\frac{S}{c}}(\lambda_c), \sigma_1^{\frac{S}{c}}(\lambda_c)\right] + (1 - \alpha^{\frac{S}{c}}(\lambda_c))N\left[x; \mu_2^{\frac{S}{c}}(\lambda_c), \sigma_2^{\frac{S}{c}}(\lambda_c)\right] \quad (1.15)$$

Where α and λ_c are constants. For completeness, the average cross-sectional area A_x is computed as

$$A_x = \begin{cases} 0.540424L_c^2, & L_c < 0.00167m \\ 0.556945L_c^{2.0047077}, & L_c \geq 0.00167m \end{cases} \quad (1.16)$$

The velocity distribution ($D_{\Delta V}(x, v)$) is categorized into explosion fragments and collision fragments respectively

$$D_{\Delta V}^{EXP}(x, v) = N[x; \mu^{EXP}(\lambda_c), \sigma^{EXP}(\lambda_c)] \quad (1.17)$$

$$D_{\Delta V}^{COLL}(x, v) = N[x; \mu^{COLL}(\lambda_c), \sigma^{COLL}(\lambda_c)] \quad (1.18)$$

All constants have been experimentally determined through hypervelocity impact tests and are outlined in Johnson (2001) [15]. Using the collision probability from Kessler (1991) [11] and historical explosions, along with a long-term F10.7 projection of the solar cycle, the future state of the debris environment can be calculated in a program such as LEGEND. The F10.7 projection corresponds to the solar radio flux per unit frequency ($W m^{-2} Hz^{-1}$) at a wavelength of 10.7cm.

Coming back to the big picture, a sensitivity study of the debris environment growth was conducted by Johnson (2007) [16] for general active debris removal of 5, 10,

and 20 objects removed per year. Only particles of size 10cm and greater were considered between 200 and 2000km altitude and the results are shown in Figure 10 and Figure 11.

An effective reduction factor (ERF) is defined as the total number of objects reduced by 2206 divided by the number of objects removed via active debris removal (ADR) through 2206. The year 2206 was chosen as a 200 year forecast from the time of the study. The ERF is a good measure of the effectiveness of an ADR technology; however, this sensitivity study does not correspond to any particular technology which allows it to remain objective in nature.

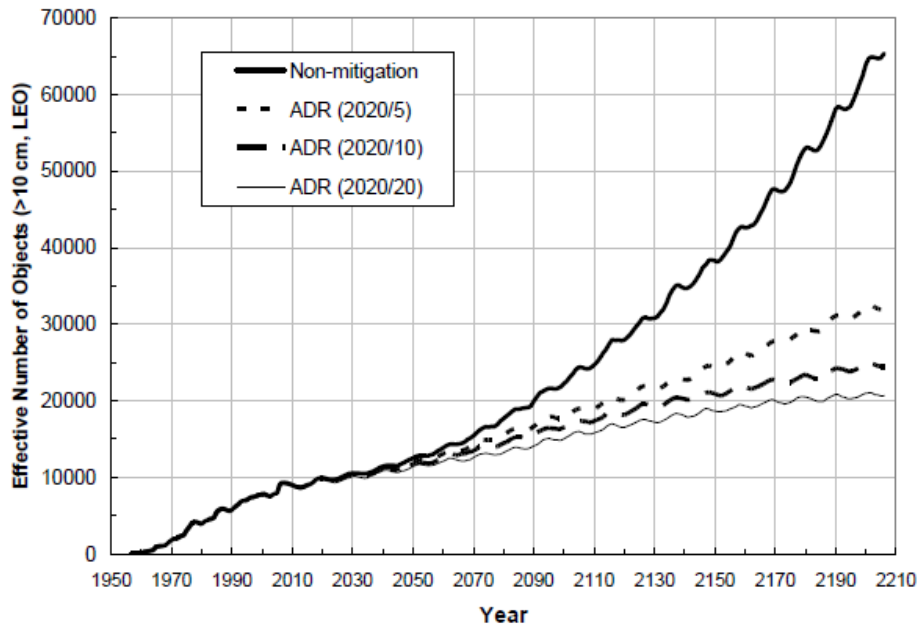


Figure 11: ADR 5, 10, and 20 objects per year [16].

The different ADR rates were chosen at convenient intervals to demonstrate the change in the environment. It will be beneficial to perform such an analysis once the ADR rate of specific technologies are determined, as the ERF factor will help determine the feasibility of a given removal technology.

1.5 Thesis Overview

In general, there are three main points of attack to the orbital debris problem: Mitigation, Avoidance, and Removal. If we minimize the amount of new debris (Mitigation), this simply slows down the problem as the current debris field is still self-evolving and poses a threat to our space missions. International policies and engineering design specifications courtesy of the LDEF have been developed to help reduce collision impact probability with new spacecraft (Avoidance). Therefore, the main topic of discussion remains the removal and subsequent technologies associated with the removal. To help bring a final level of urgency to the matter, below are two excerpts from the 2011 National Research Council release on space debris:

“Finding: Enhanced mitigation standards or removal actions are likely to be necessary to limit the growth in the orbital debris population. Although NASA’s orbital debris programs have identified the need for orbital debris removal, the necessary economic, technology, testing, political, or legal considerations have not

been fully examined, nor has analysis been done to determine when such technology will be required. [17]"

"Recommendation: NASA should join with other agencies to develop and provide more explicit information about the costs of debris avoidance, mitigation, surveillance, and response. These costs should be inventoried and monitored over time to provide critical information for measuring and monitoring the economic impact of the meteoroid and orbital debris problem, signaling when mitigation guidelines may need revision, and helping to evaluate investments in technology for active debris removal. [17]"

Chapter 2 will review the current proposed technology contenders in terms of theory of operation, as well advantages and disadvantages for both small and large debris removal. The systems that will be discussed include: the Orion laser project, Electrodynamic Tethers, an experimental dust cloud, the Ion-Beam Shepherd, and a satellite rendezvous with modular de-orbit devices.

Focusing on the large debris category, Chapter 3 will then analyze the Electrodynamic Tether (EDT) system and the Ion-Beam Shepherd (IBS) system in detail in order to examine the feasibility and effectiveness of a new hybrid design. Chapter 3 starts by investigating *'How'* these two technologies function. First, the force generated by

the EDT and the astrodynamics of a satellite exposed to these forces are investigated. Thereafter, the classical current control laws used for orbital maneuvers and the problems inherent to the EDT concept using these laws are outlined. A control method is introduced to independently change orbital elements using EDT and a new control scheme is outlined using both the classical and Tragesser control methods for speed and accuracy in the final state vector. Two sections are presented on theoretical case studies for final rendezvous and attitude control acting as proof of concepts. Chapter 3 then delves into the operating aspects of the IBS technology by investigating the fuel consumption of the satellite without the assumption that the mass of the spacecraft is much smaller than that of the debris, as is done in the reference literature. After arriving at an appropriate formulation for the fuel cost of the satellite, as well as optimum exhaust velocity, the fuel consumption is formulated in a numerical scheme.

Here we sidestep and investigate the plasma physics behind the IBS design in order to investigate *'How Well'* the design performs in terms of momentum transfer and the factors that affect its efficiency. The plasma physics of the ion beam divergence is investigated, and conclusions are made on the operating distance of the IBS with respect to the debris at which this becomes an issue. Suggestions of possible beam-plasma instabilities are found, and recommended for further research.

In order to compare the hybrid design with the current designs for large debris removal, a mission is outlined to de-orbit multiple satellites as was found in the reference literature. This will serve as a benchmark test for each technology in terms of how many satellites it can de-orbit before it runs out of fuel and in what timeframe. Four technology combinations are simulated to de-orbit a series of sequenced sun-synchronous debris objects of high importance. These combinations are: Thruster rendezvous with modular thruster de-orbit device, thruster rendezvous with IBS de-orbit, EDT rendezvous with EDT de-orbit, and EDT rendezvous with IBS de-orbit. A standard Runge-Kutta-4 (RK4) integration scheme was used to solve the classical equations of motion, and a dipole model was adopted for the earth's magnetic field. The simulation includes appropriate rendezvous with the target within a certain degree of error, as well as a successful de-orbit to a natural decay perigee altitude.

Typical errors in the state vector using the new control scheme are shown for the hybrid system, and several limitations of the EDT technology in sun-synchronous orbits were encountered and discussed. The results are compared in terms of fuel cost and time, and the co-dependent elements of the EDT maneuvers are analyzed. Lastly, a small 200kg variant of the IBS+EDT hybrid is simulated and discussed.

Chapter 4 contains a conclusion on the simulation results and analysis of the proposed result. The chapter concludes with recommendations for future work.

Chapter 2

Orbital Debris Removal Technologies

In order to understand and analyze the current space debris removal technologies, a thorough understanding of their technical functions, advantages and disadvantages is required. This section will focus on some of the more mature technologies found in the literature survey; the Orion Laser system, Electrodynamic Tethers (EDTs), Dust Cloud De-orbiting, Ion Beam Shepherds, and Satellite Rendezvous with modular external propulsion devices.

2.1 Orion Laser

In 1995, NASA and the U.S. Air Force Space Command initiated a feasibility study of removing the majority of space debris in LEO by irradiating it with a ground-based laser. In theory, the laser would melt a thin surface layer from the debris particles, causing plasma blow off. The resulting dynamics of the reaction from one or more laser hits is expected to lower the perigee of the orbit, which would increase drag and hasten reentry of the debris particle [18].

Based on models developed at the USAF Phillips Laboratory, NASA/MSFC, and NASA Johnson Space Center, a 200km altitude is defined as a successful irradiated de-orbit perigee. An example given in Campell (1996) [18] is a steel part having an average

cross sectional area to mass ratio of $0.15\text{cm}^2/\text{g}$ has an expected life in orbit of about 7 days at 200km, whereas this life is extended to 18 years at an altitude of 500km.

Two main strategies were developed for selecting which particles to hit with the laser labeled 'one pass, one de-orbit' and 'steady rain'. The first strategy waits for a particle to rise above the horizon, and then bombards it with laser pulses until its orbit has reached below the 200km threshold. Since the event occurs just as the debris rises above the horizon, the relative angle between the laser path and the debris velocity vector should be very small, resulting in a force primarily anti-parallel to the velocity vector. The second strategy involves engaging lower altitude particles before higher altitude ones. That is, particles between 200km and 300km would be addressed first and de-orbited to below 200km, then a particle between 300km and 400km can be lowered to the 200km-300km altitude band, and a particle from the 400km-500km band can be lowered to the 300km-400km band etc. This bottom up approach ensures that the number of debris particles at any given altitude does not increase as particles are de-orbited since any given particle simply fills a hole left by a previous de-orbit. This ensures that there is no temporary spike in risk to assets in any given orbit.

2.1.1 Technical Aspects of Operation

The effectiveness of the ORION system depends highly on its ability to change the momentum of a debris particle through high-energy interactions with its surface material. The coupling coefficient (C_m) is defined as the ratio of the momentum transfer to the energy delivered by the laser. It can be further defined as a non-linear function of laser intensity for given material properties, where intensity is the ratio of the beam power to its cross-sectional area. The peak of the C_m function defines the optimal operation parameters for the laser, where the momentum change is maximized for the least amount of energy input from the laser system, as shown in Figure 12. Figure 12 shows a C_m curve for Nylon using a KrF laser with a pulse duration fixed at 22ns. The most efficient laser intensity is shown to be around $2.5E8$ W/cm². An interesting note is that even if the laser intensity was reduced to 50% of the optimal value, the C_m is only reduced from 6.5 dyne s/J to 6 dyne s/J [18]. This illustrates that the momentum transfer is rather forgiving as long as the arriving intensity is around the optimal level, which is important given the uncertainties in the atmospheric effects of laser propagation. However, since the intensity of the pulse depends on the duration, assuming a given total energy, the C_m is also a function of pulse duration. As the pulse duration decreases, the intensity for peak efficiency decreases because less energy is conducted (lost) into lower layers of material.

The optimal incidence fluence for varying pulse durations, which define the available laser technologies, is shown in the Figure 13 for all materials and wavelength ranges.

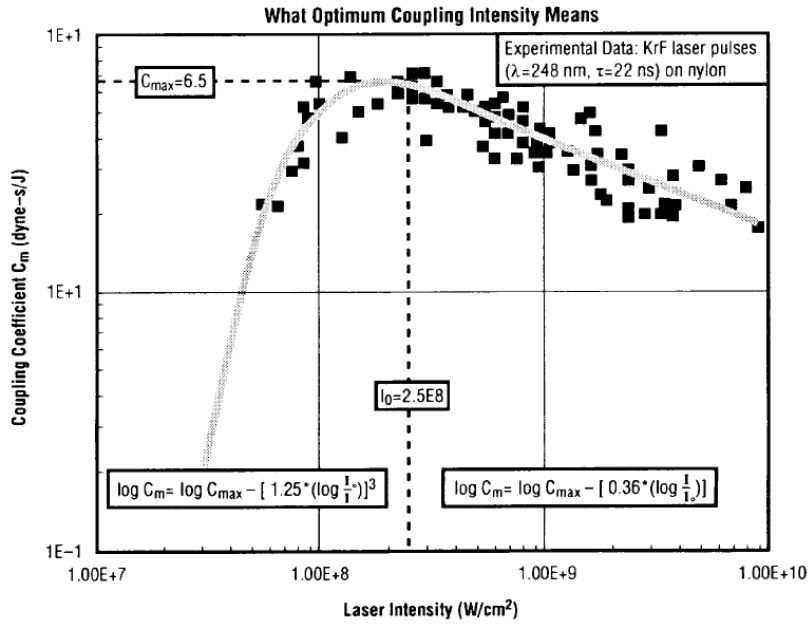


Figure 12: Optimal Coupling Intensity [18]. On a Log-Log scale the coupling coefficient, a measure of the efficiency of the momentum transfer, is related to the laser intensity reaching a maximum peak value at around $2.4E8$ W/cm^2 . The pulse width is kept to 22ns at a wavelength of 248nm. The functions of the coupling coefficient to the laser intensity either side of the peak are given by the two formulas near the bottom of the figure.

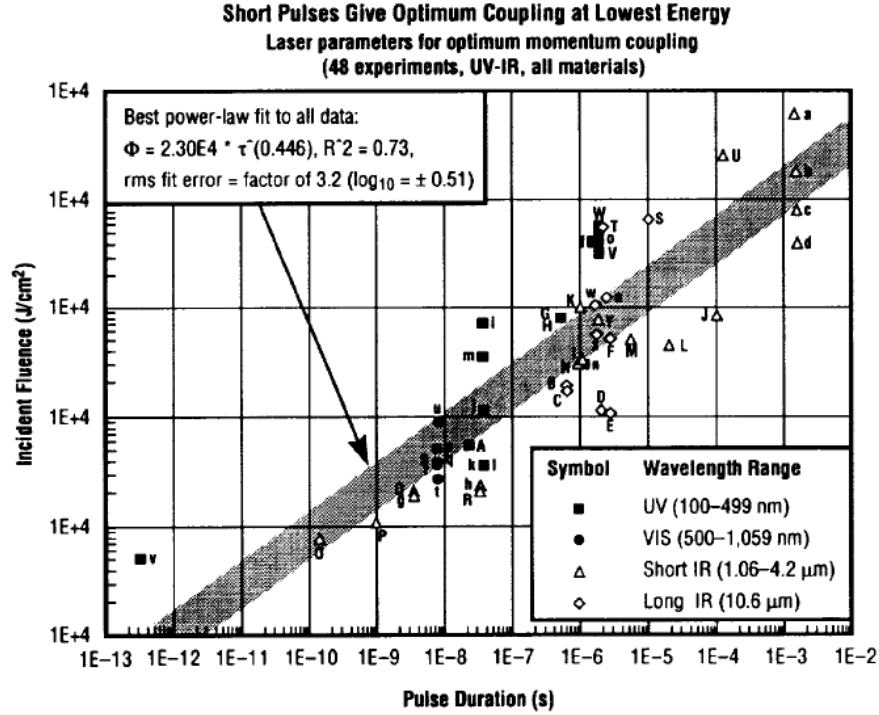


Figure 13: Optimal Incident Fluence for varying pulse widths [18]. This figure shows that the incident fluence is a function of pulse duration, which in turn will affect the optimal coupling coefficient; making this a 2 variable optimization problem to find the most efficient combination of laser intensity and incident fluence.

A major design constraint is finding a laser that can deliver the corresponding incident fluence at a given pulse duration. Furthermore, a sensor system is required to determine the particle's orbital parameters before and after engagement so that the desired momentum change can be achieved. The number of pulses required to de-orbit a particular debris particle is defined by the total change in velocity required to bring it to 200km altitude, where the change in velocity provided by a single laser pulse is given by

$$D_v = C_m F \frac{A}{M} \tag{2.1}$$

where C_m is the coupling coefficient, F is the incident fluence and $\frac{A}{M}$ is the area to mass ratio [18]. If the required change in velocity cannot be met in a single pass, then the particle might have to be de-orbited in more than one pass. This requires the sensor system to track the particle after each pass to ensure that risk to assets in lower orbits does not increase in between passes.

Two of the main design limitations of the ORION laser systems are the diffraction characteristics of the focusing mirror, and the atmospheric disruption of the laser such as absorption, turbulence, and nonlinear effects. Campbell (1996) [18] shows a sample calculation assuming a mirror size of 3.5m, a 500nm laser, and a maximum distance of 2000km. At these values, the spot size reaches a diameter of about 70cm, requiring a pulse energy of 20kJ to maintain the 4.6 J/cm² fluence at 10ns pulse width. This worst case scenario proves the feasibility of the Orion Laser system for orbital debris since existing technology can provide the required fluence for even the most distant and densest objects under consideration using current technology. Table 3 outlines some technology development improvements and consequences associated with this system.

Furthermore, to prevent the beam from spreading and losing coherence as it passes through the density variations in the atmosphere, an adaptive optics system is required.

Table 3: Technological Improvements to Orion System and consequences.

Technology	Improvement	Consequences
Smaller Spot Size	Reduces Power Requirements	Increased Tracking resolution Larger Mirror Size (If mirror >3.5m, aperture size becomes primary cost driver)
Shorter Wavelength Laser	Smaller Aperture size	Turbulence Issues Surface Accuracy of Mirror

Given that the atmosphere is highly absorptive for most wavelengths, the regions of operation are limited to 400nm to 1300nm, and 9500nm to 12000nm [18]. The mirror size required to produce a small spot size for the longer wavelength range is extremely large, therefore this technology is limited to the visible to near infrared wavelengths. Factoring in non-linear effects of the atmosphere such as its nonlinear refractive indexes, stimulated thermal Rayleigh scattering, stimulated Raman scattering, and Whole-Beam Thermal Blooming, defines a maximum intensity of $3E6$ W/cm² and maximum pulse width of 10ms [18].

Furthermore, some lasers might require guide stars in order to assure proper pointing. The requirements of the technology are therefore defined in Table 4.

Table 4: ORION Laser Requirements

Maximum Laser Near Field Intensity @1mm	3MW/cm ²
Maximum Laser Pulse Width @1mm	10ns
Incident Intensity	600-850 MW/cm ² @5-10ns Width
Required Total Incident Fluence for de-orbit	4 to 6 J/cm ² @5-10ns Width
Incident Altitude	800-1500km

2.1.2 Implementation

The technology tradeoff is shown in the Table 5, outlining the Nd (Neodymium) Solid State laser as the best option for the actual debris removal. The KrF laser from Figure 12 and Figure 13 has been ruled out as a possible implementation due to its wavelength of 248nm. The other half of the concept constraints are within the sensor system. Table 6 outlines the trade study performed by Campell (1996) [18], where the microwave radar and passive optics are the two sensors that perform the best for the sensing of the debris. Passive optics look at the general region of interest and wait for a signal to appear in the visible spectrum, such as sun reflections off the surface of the debris, or the emission given from plasma ignition on the surface of the debris after being shot by the laser. A note that must be taken into consideration is that the radar systems considered here have a minimum detection diameter of 1cm.

Table 5: ORION Laser System Tradeoff. Reproduced from Campell (1996) [18].

Rep-pulsed Laser Options	(m)	Beam size at 1500km (cm)	Laser Pulse Energy for Efficient Thrust (kJ)		Beam Fluence in Atmosphere (J/cm ²)		SRS-Safe Beam Fluence in Atmosphere (J/cm ²)		Guide-stars needed	Cost (\$M)		Laser Device Choice Basis
			1 s	10 ns	1 s	10 ns	1 s	10 ns		1 s	10 ns	
Nd Solid State	0.53	24	24	3.0	0.085	0.011	2	0.04	4* (difficult)	54	23	* Cheaper but Guide-star Kluge
Nd Solid State	1.06	48	97	12	0.34	0.043	2.5	0.05	1	100	40	Best Cost That Works
DF Chemical	4+-	180	1370	170	4.9	0.61	2.5	0.06	0	1920	290	High Cost Won't Work (SRS)
CO2 Gas	10.6	480	9700	1200	34	4.3	3	0.07	0	11400	1700	High Cost Won't Work (SRS)

CW Laser Option	(m)	1500 km Beam dia (cm)	Laser Power (kW)	Intensity in atmosphere (W/cm ²)	Blooming-safe Intensity (W/cm ²)	Guide-stars needed	Cost (\$M)	Basis for laser device choice
Iodine Gas	1.3 CW	59	3200	11	8?	1	68	Blooming? Beam Quality? Target Interaction? Next lower cost

Table 6: ORION Sensor System tradeoff. Reproduced from Campell (1996) [18].

Parameter	Microwave Radar	Passive Optics	Bistatic System	Laser Radar
Detection				
500 km	1 cm	1 cm	> 5 cm	1 cm
1000 km	1 cm	1 cm	> 10 cm	1 cm
1500 km	2 cm	1 cm	> 20 cm	1 cm
Tracking	Yes	Yes	No	Yes
Discrimination	Excellent	Good	Unknown	Excellent
Handover	Excellent	Excellent	NA	Excellent
Accuracy				
Damage Assessment	Excellent	Partial	No	Excellent
Utilization	24 h/day	< 4 hr/day	24 h/day	24 h/day
Availability	Exists	Buildable	New	ORION
Cost	Low for Haystrack	Low for Starfire	Unknown	ORION +
	High/New	Moderate/New		

The projected time to clear the space between 200km and 800km for normal radar (A2) and passive optics (A1), based on the availability time of the sensor system, the laser pulse rate, and the incident fluence, is 2 years and 3 years respectively with associated projected costs of \$100M and \$65M. The total number of particles removed is projected as 30,000. Furthermore, part of the costs for option A2 is allocated towards development of a new beam director (3.5m telescope). Further technologies have been outlined for the removal of debris up to 1500km within 3 years, but require the development of many more technologies and hence bear much higher costs (\$140M-\$240M).

Before the technology can be built and implemented on a large scale, the technology must be demonstrated with shuttle-deployed debris to show functionality. The estimated costs for the demonstrators are \$16-\$28M for A2 and \$13-\$23M for A1.

2.1.3 Advantages

The Orion Laser System proposes multiple advantages compared to traditional space-based removal methods.

- No Launch Cost other than initial debris deployment for functionality demonstration
- No risk of introducing more debris into the environment
- Estimated to clear space within three years
- Most of the technology already exists
- Easily accessible in case of maintenance or improvements
- Does not depend on solar energy or fuel for operation
- Small minimum cross section of debris of 1cm

2.1.4 Disadvantages

This system also has several disadvantages based off of the technology and operational requirements

- Complex tracking of very small debris particles
- Guide star tracking and position 'handoff'
- If more than one pass is required, complex radar handoff

- Very accurate surfaces on mirrors for smaller wavelength lasers
- Laser pointing for smaller spot sizes
- High testing and development cost
- Only removes debris up to 800km with higher altitude removal up to 1500km more than doubles the development cost
- Laser 'shadow' could ablate higher orbit satellites
- Ineffective for targets >20cm due to heavier mass [19]

2.2 Electrodynamic Tether

Electrodynamic tethers have been under investigation as an orbital debris removal tool for several years. The main concept involves generating a drag force by extending a long conducting tether which interacts with the earth's magnetic field to de-orbit a host spacecraft which has mated with a piece of debris using a subsatellite. This technology seems interesting for both debris-orbit as well as the 'tow-truck' service proposed by NRL and DARPA to carry debris into graveyard orbits [20].

2.2.1 Technical Aspects of Operation

The electrodynamic drag concept is a result of the Lorenz force produced by the interaction of the current flowing through the tether and the geomagnetic field. The drag force ($\overrightarrow{F_D}$) is defined as

$$\vec{F}_D = \int_0^L I \vec{dl} \times \vec{B} \quad (2.2)$$

where I is the current in the tether, \vec{dl} is the differential length element, and \vec{B} is the magnetic field vector. The current is either modulated or self-sustained by a potential difference (Φ) caused by the sweeping motion of the tether through the magnetic field lines given by the Hall effect

$$\Phi = \int_0^L (\vec{v} \times \vec{B}) \cdot \vec{dl} \quad (2.3)$$

where \vec{v} is the velocity vector, \vec{B} is the magnetic field vector, and \vec{dl} is the differential length element. Furthermore, the dissipated power by the drag force (P_D) can be written as

$$P_D = \vec{F}_D * \vec{v} \quad (2.4)$$

This is used to estimate the time required to change the orbital altitude of a debris object from altitude a_1 to a_2 assuming perfectly circular orbits throughout the maneuver (ΔT)

$$\Delta T = \int_{a_1}^{a_2} \frac{\mu_0 m}{2a^2 P_D} da \quad (2.5)$$

Important orbit parameters that affect the effectiveness of this technique are initial altitude and inclination. Objects at lower altitude decay faster than those at larger altitudes due to the increased currents sustained due to the higher density of ionospheric plasma. Furthermore, the potential difference generated by the relative motion of the

tether with respect to the earth's magnetic field is maximized at the equator and decreases with increasing inclination [21]. This conclusion is due to the assumption that a tethered spacecraft will be gravity gradient stabilized and drag stabilized such that the tether is nadir-pointing. Tether rigidity becomes an apparent problem with this assumption. In a realistic scenario, a tether spanning several kilometers could experience significant density gradients between the base and the tip. This would result in more drag at the tip than the base, causing the tether to flex. The normal component of the tether would then be a function of its length, causing the induced drag component of the EDT to no longer be in a uniform direction. This not only reduces the efficiency of the drag generated, but could also cause changes in other, undesired, orbital parameters. For implementation, a detailed analysis of tether rigidity needs to be performed. However, for simulation purposes, the tether is assumed to be rigid in the remainder of this paper.

The major design tradeoff of the electrodynamic tether concept is the length and configuration of the tether. Longer tethers will provide a shorter de-orbit time due to increased drag force. However, longer tethers come with the cost of increased mass, increased risk of arcing, and increased exposed surface area capable of being hit by other orbital debris. For typical LEO satellites the tether should have a length of 5-7.5km and a mass of 1-2% of the SC mass [21]. The de-orbit times to 250km for varying inclinations and altitudes for a 7.5km tether with 1% of the SC mass is compiled in Table 7. A note

that should be taken about this technology is that it requires a physical attachment to a debris object, and is therefore only appropriate for large debris such as inactive satellites or rocket bodies (objects > 10cm in diameter).

The main advantage of the EDT is that it does not require any propellant to de-orbit the debris object. This allows more room in the mass budget for larger tethers where other technologies would have to allocate a mass percentage for propellant (10-20%). In terms of future mitigation, this prevents spacecrafts from storing large amounts of propellant that remain unused until end of life. In terms of carrier spacecrafts, this will reduce the overall launch mass of the spacecraft, reducing its cost.

Table 7: EDT de-orbit times for varying orbits [21].

Initial altitude (km)	Orbit inclination			
	0°	25°	50°	75°
1400	170	220	325	EDT not effective
1300	140	185	280	
1200	120	155	230	
1100	95	125	185	
1000	70	95	140	375
900	55	70	110	280
800	45	55	80	200
700	30	40	55	140
600	20	30	40	80
500	15	20	25	40
400	10	15	15	20

On the other hand the main disadvantage is that the tethers are very long and thin, increasing the chances of accidental severing through manufacturing defects, system malfunctions, material degradation, vibrations, and contact with other spacecraft elements. Furthermore, the large cross-sectional area once deployed increases the risk of collision with other debris, turning your de-orbiting debris into a target with a relatively high density, which would fracture into more debris upon collision. Also, possible collisions with small debris can sever the tethers. This outlines two main problems that need to be investigated with EDT before implementation can be considered as described in Pardini (2009) [21]:

1. To determine the risk of tethers colliding with operating spacecraft, the risk posed by the tether fragments after it has been severed or hit by debris, and the chance of multiple tethers colliding with each other due to their large length
2. To evaluate the risk of a tether being cut during the mission by orbital debris and meteoroids.

The problem of tethers colliding with other tethers only arises as the number of tethers approaches 100 [21]. At 100 tethers distributed randomly between 500km and 1500km, the impact probability is on the order of 10^{-1} , requiring active control of the

tether. This active control requirement adds additional subsystems to the EDT de-orbit system and increases the complexity of the design.

Tethers are also extremely vulnerable to small debris hypervelocity impacts and can be cut by particles with a diameter of one third to one half of the tether diameter [21]. The impact probability of the tether with the space debris environment is no different than that of a spacecraft collision similar to Klinkrad (2006) [8]. Statistical approaches have been investigated and confirm that the risk of collision with debris is small, but not negligible; again requiring active control of the tether during the mission.

Since the collision with other tethers is currently not a problem, and collision with other spacecraft can be avoided through active control, the main constraint to determine the feasibility of using EDT is the collision probability with other space debris. Simulations were performed using ORDEM-2000 and the Gruen Model to analyze this constraint labeled IADC AI 19.1 test 1 and 2. Test 1 investigated 5km, 7.5km, and 10km single strand tethers and concluded results for several diameter classifications, outlined in Table 8. Simply increasing the diameter of the tether is not a solution since this will increase the mass of the tether substantially; therefore the second test was run to investigate the survivability of multi-strand tether designs as shown in Figure 14. The conclusions of the second test indicate that the survival probability increases considerably for a double-strand design. The term 'knot' is used to denote the point of intersection of

the two strands. The survival probability increases as the distance between knots increases, with an upper limit of about 95+% (ORDEM- 2000) with knot spacing of 6cm for a 1mm tether, varying slightly with orbital parameters [21]. These results, however, were found to vary significantly based on the space debris environment model that was used which makes the survivability analysis performed not applicable for proof of concept and implementation. Furthermore, to perform a more thorough analysis, hypervelocity impacts on EDT need to be performed in order to establish proper damage criteria. However, as the models improve, such an analysis can be redone to calculate the survivability for innovative tether designs to optimize mass and survivability.

Table 8: EDT Lifetime for single-strand varying diameters.

Tether Diameter	Estimated Lifetime
<1mm	<10 days
2.5mm	40-50 days
5mm	<1year
1cm	3.5-7.2 years (5km)
	2.3-4.8 years (7.5km)
	1.7-3.6 years (10km)
2.5-5cm	10-100 years (depending on length and orbit)

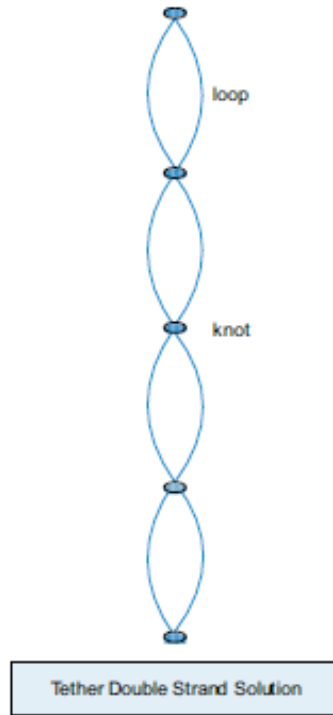


Figure 14: EDT Double-strand configuration.

2.2.2 Implementation

The EDT concept requires either previous installation on spacecraft as a means of future preventative measures, or a rendezvous craft to attach to the debris. Since this paper is addressing the removal of current space debris, the later scenario will be investigated. Since the underlying concepts behind EDT technology have been outlined, the principle of a rendezvous craft will now be investigated.

The following aspects of an EDT rendezvous mission are investigated in Ishige et al

(2004) [22]:

- Required time for removal operations
- Tether behavior during debris separation phase
- Orbital transfer strategy

The studied mission involves a ‘service satellite’ which rendezvous with a debris object, attaches to it, deploys an EDT, de-orbits to an altitude where the lifetime is 25 years (~630km), detaches the debris to naturally decay, then maneuvers to the next debris object. Figure 15 outlines the major phases of the proposed mission.

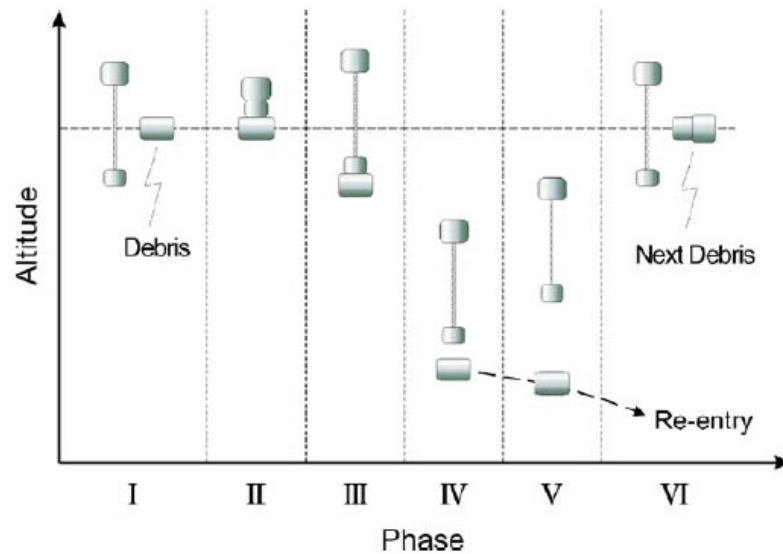


Figure 15: EDT Mission Phases.

The total removal operation time is dependant both on de-orbiting through the Lorentz drag force and the reverse EMF that can be generated in the EDT to raise the orbit to the initial altitude.

Given that the de-orbit time is directly proportional to tether length, the main variable in the total mission time is the tether length during re-orbit. By investigating two test cases as host satellites (Globalstar and ADEOS), Ishige et al (2004) [22] concluded that the total round-trip time was almost the same for tethers extended between 5 and 10km during orbit rise, even though the 10km tether produced the largest Lorentz force as shown in Figure 16. This is due to the fact that the force generated by the tether has diminishing returns with increased length. Therefore, from the aspect of limiting risk due to orbital debris, inter-EDT collisions, and power budget, the tether does not need to be extended to its maximum length during the orbit-rise phase (V). The second bullet of the mission design is investigating the tether behavior directly after separation. Given the scenarios of A (stable tether oriented along the local vertical, B (continuous tether current), and C (no current). Case A-C assume a service satellite mass of 1000kg, a subsatellite mass of 500kg, and a debris mass of 1000kg, and Case D repeats case C but lowers the service satellite mass to 100kg and raises the debris mass to 1400kg. The tether in-plane angle was modeled shown in Figure 17, and the tension for Case D is shown in Figure 18.

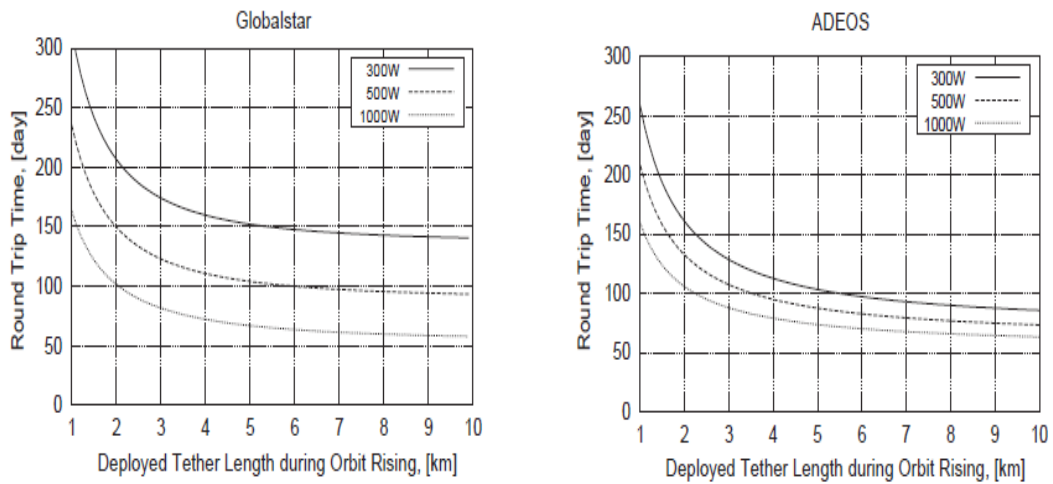


Figure 16: Round trip time for variable tether length during orbit-rise phase for Globalstar and ADEOS spacecraft.

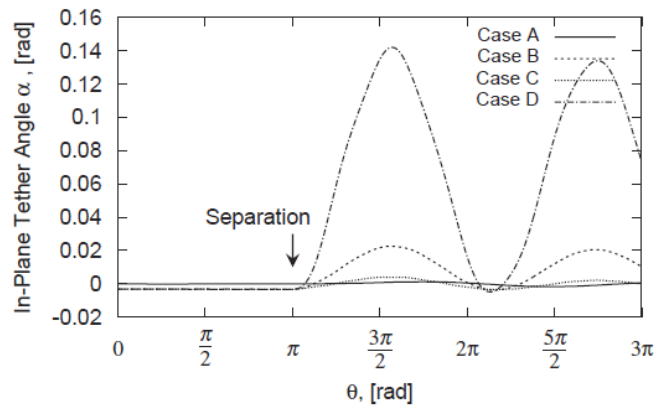


Figure 17: In-Plane tether angle vs. angle propagation in the earth frame.

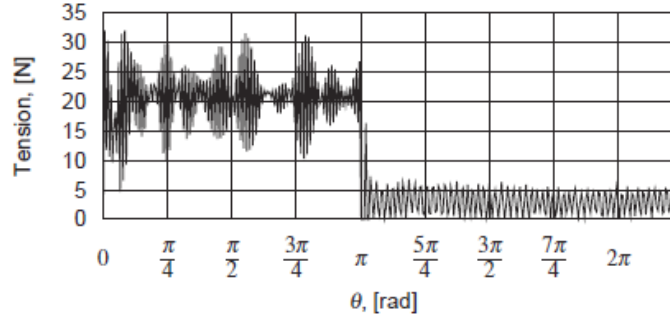


Figure 18: Tension in the tether for Case D vs. angle propagation in earth frame.

This stability criterion limits the objects that can be addressed depending on the mass of the service and subsatellite and the mass of the object. Also, an adaptive control system to orient the tether to the local vertical while reducing its extended length during re-orbit is needed.

Orbital transfers work such as plane changes work on the same principles outlined previously and a more in-depth discussion can be found in Ishige et al (2004) [22]. An important conclusion to note from Ishige et al (2004) [22] is that 215kg of propellant would be required to change a 1000kg service satellite's altitude from 1400km to 630km, and 57kg of mass for a 1 degree inclination change.

2.2.3 Advantages

The Electrodynamic Tether provides several advantages for space-based orbital debris removal:

- Requires no Fuel
- Requires a power supply as low as 300 Watts
- Can operate in any orbit given enough time for orbital parameter changes
- Multi-strand tethers reduce mass and increase survivability
- Tether can be retracted during re-orbit maneuver to decrease risk

2.2.4 Disadvantages

- Long tethers increase risk of collision with other satellites or tethers requiring active control of the tether during operation
- Tethers can be snapped by small orbital debris with a diameter $1/3-1/2$ of the tether diameter, and the tether diameter is kept small to fulfill mass budget.
- Limited to large debris objects diameter $>10\text{cm}$ due to physical coupling requirement
- Requires spacecraft rendezvous, which can be very time consuming (hundreds of days per object). Docking also poses a robotics challenge.
- Limited to low inclination orbits

- Object mass is limited based on spacecraft design. As Debris mass/Subsatellite mass increases, the tether becomes unstable and could snap from the tension oscillations.
- De-orbit temporarily increases debris density in lower orbits

2.3 Dust Cloud

The Dust Cloud theory focuses on removing very small debris that cannot be tracked by current technology, such as paint flakes. Technically speaking this technology focuses on debris less than 1cm in diameter. Many objects of this size can be generated by collisions or secondary debris generated from hypervelocity impacts. This debris poses a threat to spacecraft subsystems and precision instruments, as can be seen in Figure 19.

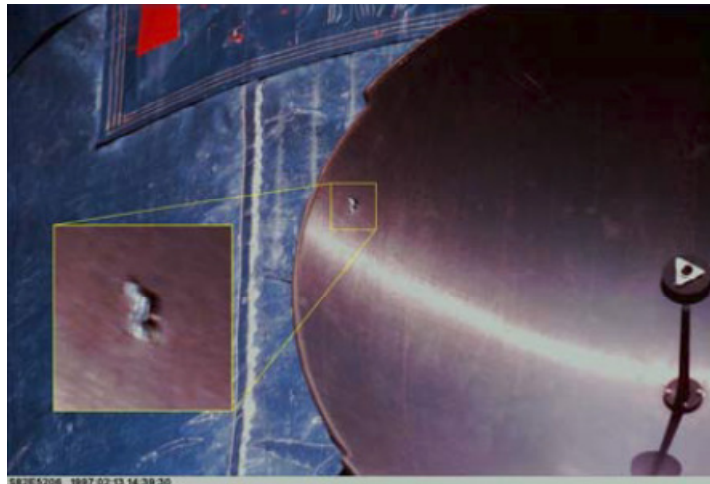


Figure 19: Debris impact on a Hubble Space Telescope Antenna resulting from an object of diameter <1cm [23].

2.3.1 Technical Aspects of Operation

Ganguli et al (2011) [23] suggests that the statistical distribution of small debris particles peaks at around 1000km, and therefore defines the mission parameters to reduce the orbit altitude from 1100km to below 900km. 900km corresponds to the altitude at which the lifetime of particles with a ballistic coefficient of 3-5kg/m² is 25 years or less. The drag on small debris particles due to an injected dust cloud is given by

$$\underbrace{\left(\frac{M}{A}\right)}_{\text{Ballistic Coef.}} \frac{dv}{dt} = - \underbrace{n_d m_d}_{\text{Dust}} \underbrace{(V - V_d)^2}_{\text{Relative Velocity}} * K - \underbrace{n_0 m_0}_{\text{Atmosphere}} V^2 \quad (2.6)$$

where V is the debris velocity, V_d is the dust velocity, n_0 is the atmospheric number density, m_0 is the particle mass, n_d is the dust number density, m_d is the dust particle mass, and

$$K = (1 + \sqrt{1 + f}) \quad (2.7)$$

$$f = \begin{cases} 1 & \text{Inelastic Collision} \\ 0 & \text{Elastic Collision} \\ > 0 & \text{loss of mass} \end{cases}$$

The total mass of dust required to de-orbit all debris with a ballistic coefficient (B) less than or equal to 5 from 1100km to below 900km in 10 years using 30 micrometer diameter tungsten dust particles with a layer thickness of 30km at 1100km is estimated to be 20 tons [23], calculated using the equation

$$M_d \sim \frac{\delta R \Delta R}{8 K N C} B \quad (2.8)$$

where K is defined in equation 2.7 (assumed to be 4 to be conservative), N is the number of debris revolutions in the dust (measure of time), δR is the change in orbital radius, ΔR is the dust layer width, B is the ballistic coefficient, and C is a correction factor assumed to be 1 in this scenario.

2.3.2 Implementation

The dust mass is proposed to be injected at nearly polar orbits in order to minimize the precession. The injection velocity would vary so that the dust forms a shell spreading in both directions, which means that when debris encounters this shell half of the dust will be counter-rotating with respect to the debris velocity vector. For hypervelocity impacts, debris particles are likely to experience instantaneous vaporization of some or all of its mass from shear energy transfer, providing local thrust on the debris. Ganguli et al (2011) [23] calculates that around $10m_d$ of mass will be evaporated if the collision has a relative velocity of $2V=15\text{m/s}$ for an aluminum debris, and about $300m_d$ of mass can be melted.

The dust mass is proposed to be injected with a width R , which is much smaller than the altitude layer t to be cleared, and synchronizing the decay rate of the dust shell and the debris since the debris will tend to decay much slower than the dust, shown in Figure 20.

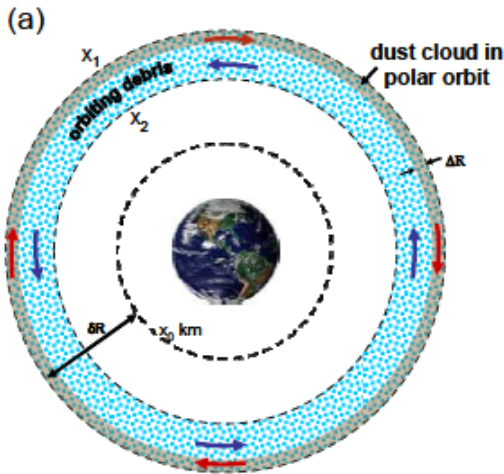


Figure 20: Dust cloud in polar orbit surrounding the orbital debris, acting as a 'snow plow' lowering the altitude of the debris [23].

The value of 20 tons was calculated using very conservative values and is likely to be lower, and can be injected in a series of installments. The size of 50 micrometers was chosen based on the effects of radiation pressure, gravity, and interactions with the near earth plasma environment which specifies a range of 20-50 micrometers as acceptable. This diameter is well within the design limits of current satellite materials [23].

2.3.3 Advantages

- No new technology development
- Removal of debris <1cm in diameter (untrackable)
- Does not pose a threat of impact, but could lower orbit of satellites
- Simple concept of operation and works autonomously

- Orbital lifetime of dust cloud below 600km is very brief
- No environmental impact

2.3.3 Disadvantages

- Limited to <1cm diameter debris
- Ten years operational lifetime and then 25 year orbital decay of debris
- The dust cloud might not increase risk to spacecraft, but the debris that is lowered does
- Requires possible maneuvering of active satellites to avoid micro debris impacts, costing fuel
- Mathematics on ballistic coefficient, K factor, and operational parameters need to be completed

2.4 Ion Beam Shepherd

The ion beam shepherd (IBS) technology has been suggested to provide docking-free de-orbiting of space debris by Bombardelli (2011) [19]. It suggests using a collimated ion beam with velocity up to 30 km/s to bombard the target. This technique would generate a de-orbiting momentum transfer orders of magnitude higher than that of the ORION laser system for the same power costs [19].

2.4.1 Technical Aspects of Operation

The IBS emits an ion beam out one end of its main payload which will intercept the target debris and provide a deceleration. The second, primary propulsion, system is required for stability to keep a constant distance between the IBS and the debris, as shown in Figure 21. The minimum divergence of the ion beam (φ_{min}) is given by

$$\varphi_{min} = \tan^{-1} \left(\frac{\sqrt{2 * q_e * \frac{T_{eV}}{m_i}}}{c} \right) \quad (2.9)$$

where q_e is the particle charge, T_{eV} is the temperature of the beam particles in eV, m_i is the ion mass, c is the exhaust velocity, and s is the cross sectional area of impact. The corresponding maximum separation distance between the IBS and the debris (d_{max}) is given by

$$d_{max} = \frac{s}{2 * \tan(\varphi_{min})} \quad (2.10)$$

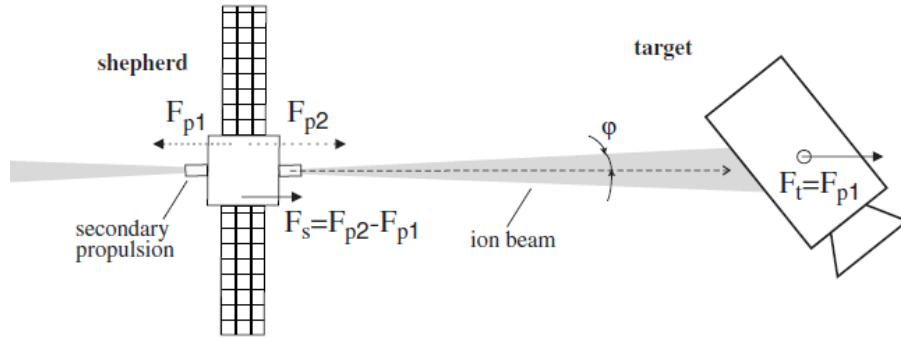


Figure 21: Ion Beam Shepherd (IBS) Operational Concepts [19].

The Irving-Stuhlinger characteristic velocity (c) of the beam [24]

$$c = \sqrt{\frac{2\eta\Delta t}{\alpha}} \quad (2.11)$$

where α is the inverse of the specific power, called specific mass of the power system (kg/W), η is the efficiency of the engine, Δt is the time of operation for the maneuver.

Equation 2.11 outlines one of the constraints of this system: the IBS needs to have a variable thruster exhaust velocity for multiple missions, to provide stable thrust depending on the time for the maneuver which varies with debris mass.

The optimal propellant mass (m_{fuel}) and spacecraft mass is shown to be obtained by summing up the structural and propellant mass, finding the optimal exhaust velocity, and simplifying [19]

$$m_{fuel} = F_p \sqrt{\frac{2\alpha\Delta t}{\eta}} \quad (2.12)$$

where F_p is the thrust of the engine, α is the specific mass of the power system, η is the efficiency of the engine, and Δt is the time of operation for the maneuver.

2.4.2 Implementation

Preliminary studies have been conducted to calculate the de-orbit time and IBS mass for an IBS system assuming circular orbit, constant tangential thrust, and an engine efficiency of 70%, shown in Figure 22 and Figure 23. Constant tangential thrust is desired such that all of the momentum transfer is used for reducing the orbiting perigee of the debris. Furthermore, non-tangential thrust can result in undesired attitude adjustments and could also affect the other orbital parameters, which is why significant effort is placed in maintaining a tangential leader-follower configuration later in this paper.

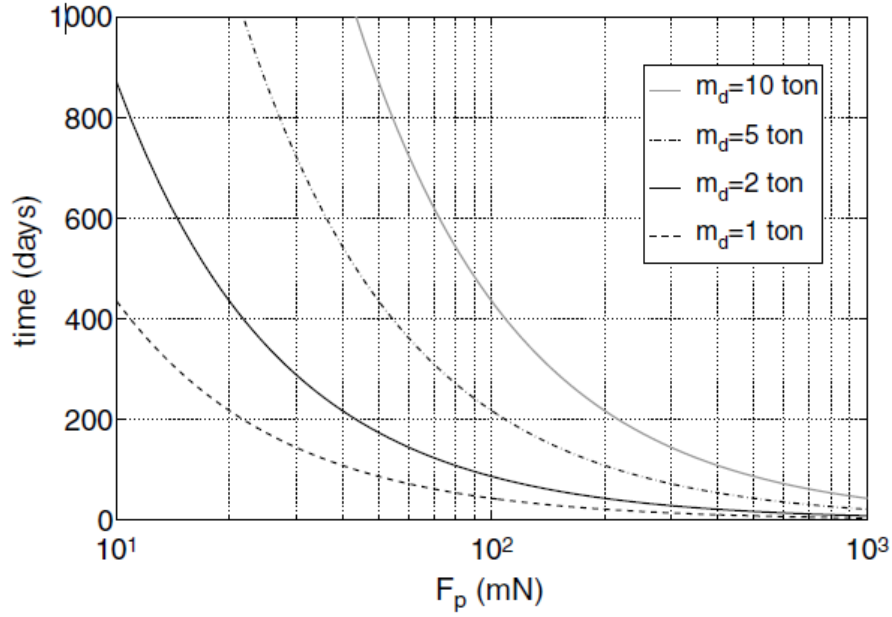


Figure 22: Time required for a transfer of varying debris masses from 1000km to 300km [19]. The force (x-axis) is related to the IBS mass as can be seen below in Figure 24.

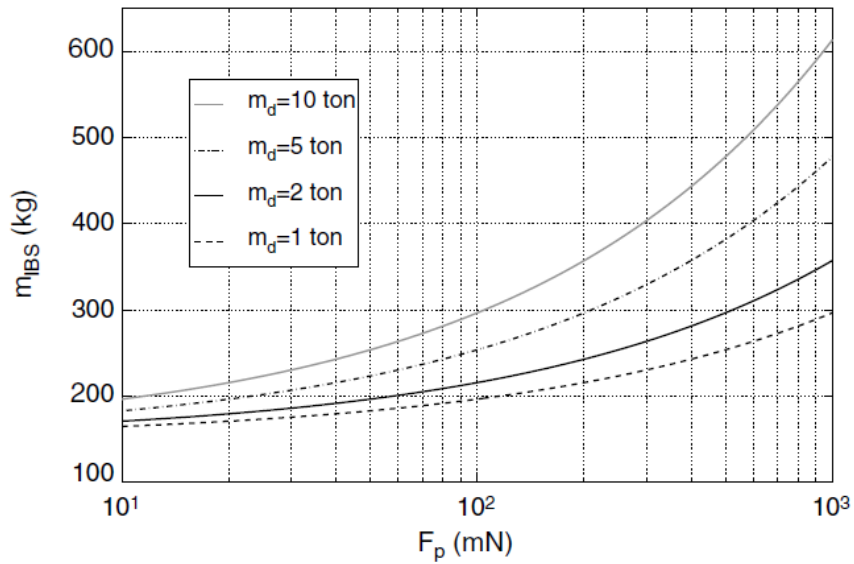


Figure 23: IBS mass for varying thrust and debris masses for a de-orbit from 1000km to 300km [19]. The time required for the force-mass configuration can be obtained from Figure 22.

2.4.3 Advantages

- Does not require contact with debris
- Orders of magnitude more momentum transfer compared to ORION for the same power consumption
- Technology exists

2.4.4 Disadvantages

- Requires fuel
- Limited to large debris >10cm in diameter (>1 ton in mass)
- Long mission time (hundreds of days for one-way)
- Complex formation flying control laws
- Inaccurate momentum transmission to target, could cause spin up of target and generation of centrifugal fragmentation.
- Required to be at a constant distance to the target
- Ion backscattering could damage IBS subsystems

2.5 Satellite Rendezvous with modular de-orbit device

The previously discussed space-based technologies require that the service satellite de-orbits along with the debris object. However, Castronuovo (2011) [25] outlines a design of a rendezvous spacecraft with modular thruster that can be attached to debris objects.

2.5.1 Technical Aspects of Operation

The technical aspects of the operation are outlined in Figure 24 and the proposed spacecraft design is outlined in Figure 25.

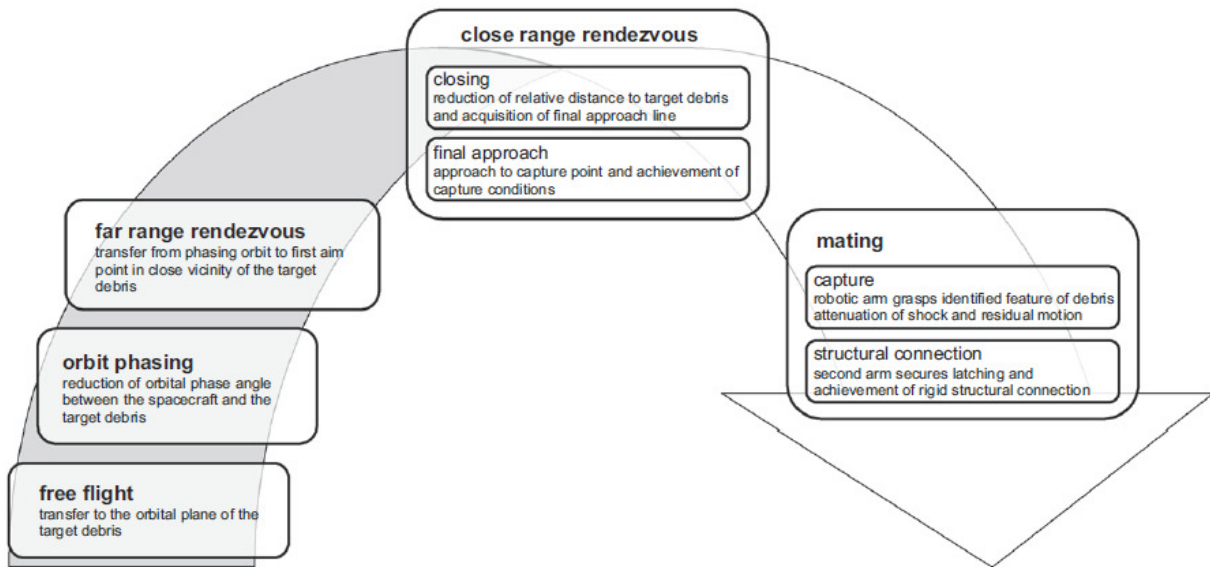


Figure 24: Operational objectives of the rendezvous satellite [25].

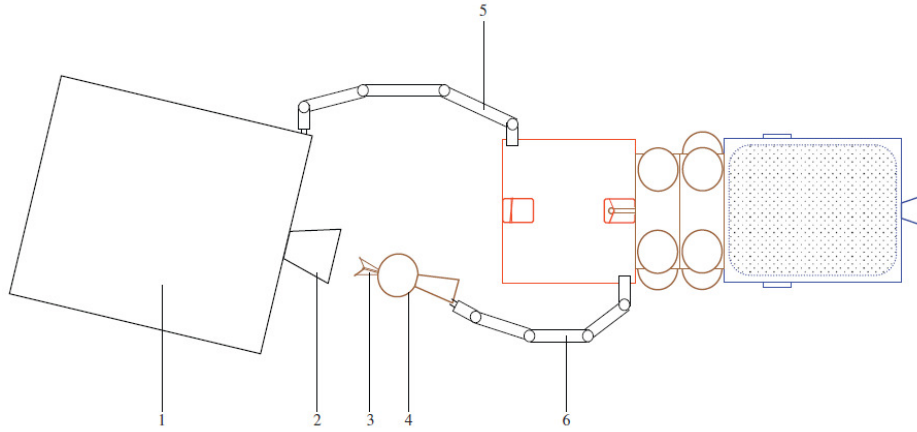


Figure 25: Spacecraft design. 1: Debris 2: Nozzle extension 3: Expanding Umbrella 4: Thruster 5: Front Arm 6: Rear Arm.

The modular thrusters would have to have variable thrust capabilities to compensate for varying ballistic coefficients and coefficient of drag. This means that a specific de-orbit sequence is required so that thrusters can be paired with objects of interest. Furthermore, since the spacecraft can only carry a limited number of thrusters, a re-supply operation is required.

2.5.2 Implementation

This design requires that the spacecraft maneuvers to a target object, captures the object with one arm, and attaches a thruster with a second arm. This poses a large problem if the target debris has an unstable attitude, which would make this mission impossible or require advanced control algorithms to match the attitude of the debris. The

thrust of the modular thrusters is chosen such that the debris enters a new orbit with an apogee that ensures decay within 12 months. The spacecraft mass evolution as it attaches thrusters to debris objects in the sequence determined in Castronuovo (2011) [25] is shown in Figure 26.

The proposed design is to remove 5 large objects per year, with a mission lifetime of 7 years including several re-supply operations. Castronuovo (2011) [25] defines a sample mission with a spacecraft mass of 2000kg having a dry mass of 600kg. This change in mass poses an issue with orbit transfers after separation with the debris object since the ballistic coefficient changes after every mission. This requires an adaptive control system to ensure no collisions with other spacecraft and so that the next debris can be appropriately targeted.

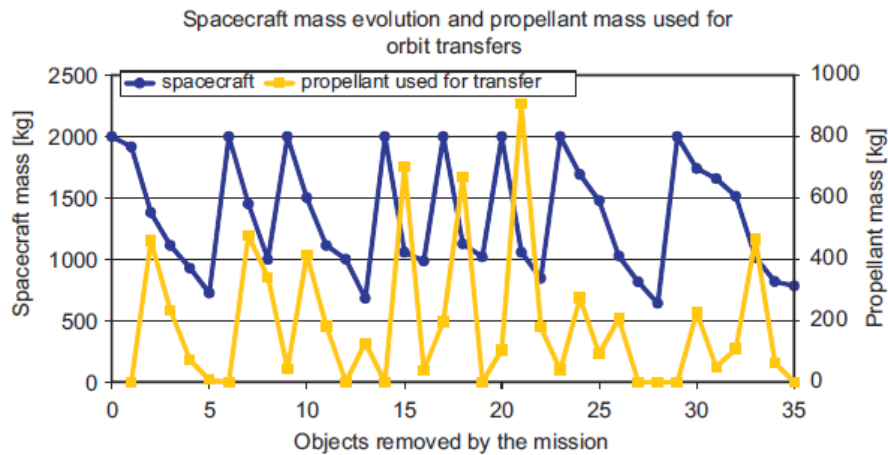


Figure 26: Spacecraft mass as objects are removed from orbit.

2.5.3 Advantages

- Does not require the service satellite to de-orbit with the debris
- Expected to clear 5 objects per year for 7 years
- Can de-orbit very large debris >10cm
- Orbit apogee decays to 700km within 12 months (ensures lifetime \ll 25 years)

2.5.4 Disadvantages

- Technical aspects of operation are limited to a general overview. Mathematical aspects of operation are not presented in Castronuovo (2011) [25]
- Debris are assumed to be stable for robot arm operation
- Requires re-fueling vehicle and operation
- Complex docking and exchange maneuvers in both debris and re-fueling vehicle using two robotic arms
- Post-mission spacecraft physical parameters change requiring robust controls

Chapter 3

Analysis and Design

The technologies outlined in chapter 2 can be broken down into two main categories; those that remove debris <10cm in diameter, and those that remove debris >10cm in diameter. From the group of technologies that removes <10cm diameter objects, the ORION laser system is by far the most mature technology and does not require any active space missions. It is the author's opinion that the ORION laser system dominates the small debris removal category and not enough information exists to compare the economics and feasibilities of the other <10cm removal technologies. Therefore, Chapter 3 will concentrate on analyzing the large debris removal technologies and developing new methods and designs based on the results of the analysis. Four main technologies are investigated: the modular de-orbit device, the electrodynamic tether, the ion-beam shepherd, and a new hybrid EDT+IBS system.

3.1 Impulsive Maneuvers

The modular de-orbit device design relies purely on impulsive maneuvers since all actions are performed by small chemical rocket engines. Therefore, this section serves to outline the main technical aspects of this technology. Impulsive maneuvers are defined by a change in velocity without a change in position. The chosen maneuvers are a bi-elliptical

transfer and a plane change maneuver which changes the RAAN and Inclination simultaneously.

Orbital altitude change maneuvers are performed at perigee and the required velocity ($V_{required}$), assumed tangential and instantaneous, is calculated by

$$V_{required} = \sqrt{\mu \left(\frac{2}{r_{current}} - \frac{1}{a_{transfer}} \right)} \quad (3.1)$$

where μ is the standard gravitational parameter for the earth, $r_{current}$ is the current orbital radius which is assumed to be circular, and $a_{transfer}$ is the transfer orbit semi-major axis. Once the satellite reaches the apogee of the transfer orbit, which serves as the perigee of the debris orbit, another impulsive maneuver is done to match the apogee of the debris orbit.

Upon arriving at the apogee of the debris orbit, a plane change maneuver is done in order to match the inclination and RAAN. The combined plane change angle (α) is given by

$$\alpha = \cos^{-1}(\cos(i_{init}) \cos(i_{final}) + \sin(i_{init}) \sin(i_{final}) \cos(\Omega_{final} - \Omega_{init})) \quad (3.2)$$

where i_{init} is the initial inclination angle, i_{final} is the desired inclination angle, Ω_{init} is the initial RAAN, and Ω_{final} is the desired RAAN. The corresponding change in velocity required (ΔV) is given by

$$\Delta V = 2V_{current} \sin\left(\frac{\alpha}{2}\right) \quad (3.3)$$

where $V_{current}$ is the current velocity and α is the plane change angle defined in equation 3.2. The corresponding propellant mass (M_p) is then calculated from the rocket equation

$$M_p = M_0 - \frac{M_0}{e^{\frac{\Delta V}{ISP}}} \quad (3.4)$$

where M_0 is the mass of the spacecraft before the maneuver, ΔV is the required velocity change, and ISP is the specific impulse of the spacecraft thrusters.

3.2 Astrodynamics of Satellites with thrust

In order to investigate the IBS and EDT technologies, non-impulsive maneuvers must be investigated. A spacecraft in orbit around a central body has the following equations of motion for the classical orbital parameters

$$\dot{a} = \left(\frac{2a^2}{h}\right) (e \sin(v) a_r + \left(\frac{p}{r}\right) a_t) \quad (3.5)$$

$$\dot{e} = \left(\frac{1}{h}\right) (p \sin(v) a_r + ((p+r) \cos(v) + re) a_t) \quad (3.6)$$

$$\dot{i} = \left(r \frac{\sin(\omega + v)}{h}\right) a_n \quad (3.7)$$

$$\dot{\Omega} = \left(r \frac{\sin(\omega + \nu)}{h \sin(i)} \right) a_n \quad (3.8)$$

$$\dot{\omega} = \left(\frac{1}{he} \right) (-p \cos(\nu) a_r + (p + r) \sin(\nu) a_t) \quad (3.9)$$

$$- \left(r \sin(\omega + \nu) \frac{\cos(i)}{h \sin(i)} \right) a_n$$

$$\dot{\nu} = \left(\frac{h}{r^2} \right) + \left(\frac{1}{eh} \right) (p \cos(\nu) a_r - (p + r) \sin(\nu) a_t) \quad (3.10)$$

where \mathbf{a} is the semi-major axis, e is the eccentricity, i is the inclination angle, Ω is the RAAN, ω is the argument of perigee, ν is the true anomaly, and p , h , and r are defined by

$$p = a(1 - e^2) \quad (3.11)$$

$$h = \sqrt{\mu p} \quad (3.12)$$

$$r = \frac{p}{1 + e \cos(\nu)} \quad (3.13)$$

These equations of motion have a singularity for circular orbits. However, since all of the satellites of interest are in slightly elliptical orbits, this singularity will not be relevant and a transformation to equinoctial coordinates is not required.

The radial, tangential, and normal accelerations due to the thrust are given by the variables a_r , a_t , and a_n . For the constant thrust case of the Ion Beam, assuming constant tangential thrust, these simply reduce to the following vector.

$$\begin{bmatrix} a_r \\ a_t \\ a_n \end{bmatrix} = \begin{bmatrix} 0 \\ T \\ m_{debris} \\ 0 \end{bmatrix} \quad (3.14)$$

where a_r is the radial acceleration (-nadir), a_t is the tangential acceleration, a_n is the orbital normal acceleration, T is the delivered thrust, and m_{debris} is the debris mass.

3.3 EDT Forces

Now that the basic orbital mechanics of all three technologies have been outlined, we take a look at a more applied approach with the electrodynamic tether (EDT) configuration. As stated previously in chapter 2, the EDT works on the foundation of the Lorentz force

$$\vec{F} = I\vec{L} \times \vec{B} \quad (3.15)$$

where I is the current in the tether, \vec{L} is the tether length vector, and \vec{B} is the magnetic field vector given by

$$\vec{B} = \frac{\mu_{mag}}{r^3} [\hat{e}_M - 3(\hat{e}_M, \hat{e}_R)\hat{e}_R]_{SC} \quad (3.16)$$

where μ_{mag} the magnetic moment of the earth is, r is the orbital radius, and \hat{e}_M, \hat{e}_R are unit vectors. An improvement over the standard dipole model would be to use the IGRF standard model for the earth's magnetic field [26]. To simplify the simulations, this method is not used for the preliminary results.

A coordinate transformation is needed to assess the magnetic field in the reference frame of the EDT given that the spacecraft is nadir pointing, which corresponds to the local z-axis [27].

$$[\hat{i} \ \hat{j} \ \hat{k}]_{ECI} \rightarrow [\hat{r} \ \hat{t} \ \hat{n}]_{SC} = \begin{bmatrix} \sin(\omega + \nu) \sin(i) \\ \cos(\omega + \nu) \sin(i) \\ \cos(i) \end{bmatrix} \quad (3.17)$$

$$\vec{B}(r, t, n) = \begin{bmatrix} -\frac{2\mu}{r^3} \sin(\omega + \nu) \sin(i) \\ \frac{\mu}{r^3} \cos(\omega + \nu) \sin(i) \\ \frac{\mu}{r^3} \cos(i) \end{bmatrix} \quad (3.18)$$

where r is the orbital radius, ω is the argument of perigee, ν is the true anomaly, and i is the inclination angle. Evaluating the Lorentz force vector (\vec{F}) in terms of the local radial, tangential, and normal reference frame yields the following forces in terms of the libration angles Θ and ϕ , which correspond to the attitude angles of the EDT in the local frame.

For a NADIR pointing tether, Θ and ϕ are both zero.

$$\vec{F} = \begin{bmatrix} IL(B_z \sin(\theta) \cos(\phi) - B_y \sin(\phi)) \\ IL(B_x \sin(\phi) - B_z \cos(\theta) \cos(\phi)) \\ IL(B_y \cos(\theta) \cos(\phi) - B_x \sin(\theta) \cos(\phi)) \end{bmatrix} \quad (3.19)$$

where θ and ϕ are the libration angles, I is the current in the tether, L is the length of the tether, and $B_{x,y,z}$ are the components of the magnetic field in the ECI reference frame.

Simply dividing by the mass of the object will give the EDT accelerations analogous to equation 3.14, where m_{debris} is the debris mass and m_{sc} is the spacecraft mass.

$$\begin{bmatrix} a_r \\ a_t \\ a_n \end{bmatrix} = \begin{bmatrix} \frac{IL(B_z \sin(\theta) \cos(\phi) - B_y \sin(\phi))}{m_{debris} + m_{sc}} \\ \frac{IL(B_x \sin(\phi) - B_z \cos(\theta) \cos(\phi))}{m_{debris} + m_{sc}} \\ \frac{IL(B_y \cos(\theta) \cos(\phi) - B_x \sin(\theta) \cos(\phi))}{m_{debris} + m_{sc}} \end{bmatrix} \quad (3.20)$$

3.4 EDT Current Laws and Control/Guidance Scheme

A large benefit of using EDTs is that they can change the orbital parameters of spacecraft without using propellant by simply modulating the current inside the tether.

Table 9 outlines the current laws required to change the respective orbital element [28] [29].

Table 9: Current Control Laws for a, e, i, and Ω .

Orbital Element	Current Law	Libration Angle θ (deg)
Semi-Major Axis	I	0
Eccentricity	$I \cos(v)$	0
Inclination	$I \cos(2(\omega + v))$	0
RAAN [29]	I	90
RAAN	$I \sin(2(\omega + v))$	0

It is shown in Burbach (2010) [29] that the 90 degree offset allows the RAAN to change with a secular nature in the other orbital elements. However, he also states that this would clearly require an attitude control system. The simplest and most cost effective control system to accomplish this would be a slewing maneuver using momentum wheels with simple state feedback. If this method does not give desirable results, then the control system required to perform this maneuver would most likely escalate in complexity and cost, and would therefore rule out this control scheme for cost effective EDT missions. The feasibility of this method is investigated in section 3.4.1.

3.4.1 Slewing Maneuver of EDT

Assuming that the EDT can be modeled as an Euler-Bernoulli beam, Figure 27 outlines the scenario at hand [30].

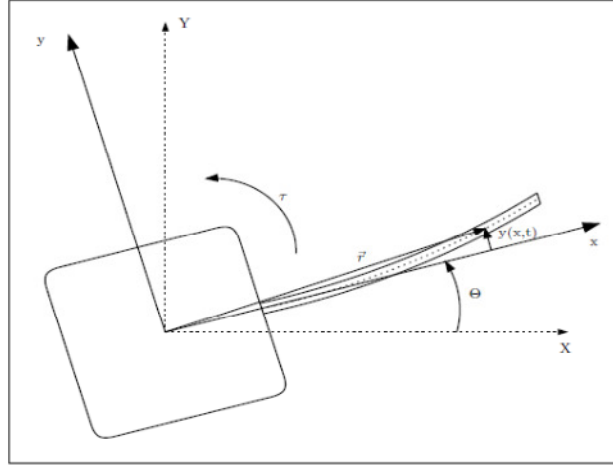


Figure 27: Satellite coordinate system and variable definition for flexible appendage slewing maneuver.

Here $y(x,t)$ defines the position of the tip of the beam from the base of the beam, and θ is the angle of rotation due to torque τ . The lagrangian of the maneuver is defined as

$$L = \frac{1}{2} I_z \dot{\theta}^2 + \frac{1}{2} \int_0^l \rho_1 \left\{ (y \dot{\theta})^2 + [(x + l_0) \dot{\theta} + \dot{y}]^2 \right\} dx - \frac{1}{2} EI \int_0^l (y'')^2 dx \quad (3.21)$$

where I_z is the moment of inertia of the tether, ρ_1 is the tether mass per unit length, x is the distance down the tether, θ is the angle between the internal x-axis and the appendage, y is the distance between the body-fixed x-axis and the appendage tip, l_0 is

the initial appendage length, and E is the tether modulus of elasticity. The deformation of the tether ($y(x, t)$) is defined as

$$y(x, t) = \sum_{k=1}^N \Phi_k(x) q_k(t) \quad (3.22)$$

$$\Phi_k(x) = 1 - \cos\left(\frac{k\pi x}{l}\right) + \frac{1}{2}(-1)^{k+1} \left(\frac{k\pi x}{l}\right)^2 \quad (3.23)$$

Here $\Phi_k(x)$ is the shape function of the appendage oscillations to degree k . This modifies the Lagrangian to

$$L = \frac{1}{2} I_t \dot{\theta}^2 + \frac{1}{2} m_q q^2 \dot{\theta}^2 + \frac{1}{2} m_q \dot{q}^2 + m_{\theta q} \dot{\theta} \dot{q} - \frac{1}{2} k q^2 \quad (3.24)$$

Defining the angular acceleration as the new control input, the equations of motion take the form

$$\ddot{\theta} = u \quad (3.25)$$

$$\ddot{q} + 2\xi\omega_n\dot{q} + \omega_n^2 q = -\alpha u + q\dot{\theta}^2 \quad (3.26)$$

$$\alpha = \frac{m_{\theta q}}{m_q} \quad (3.27)$$

$$\omega_n = \sqrt{\frac{k}{m_q}} \quad (3.28)$$

$$\xi = \frac{c}{2\sqrt{m_q k}} \quad (3.29)$$

Applying a notch filter for the $k=1$ vibration mode in order to avoid harmonics, a MATLAB/SIMULINK model produced the plots shown in Figure 28, showing the tip parameter q and the angle of rotation with time.

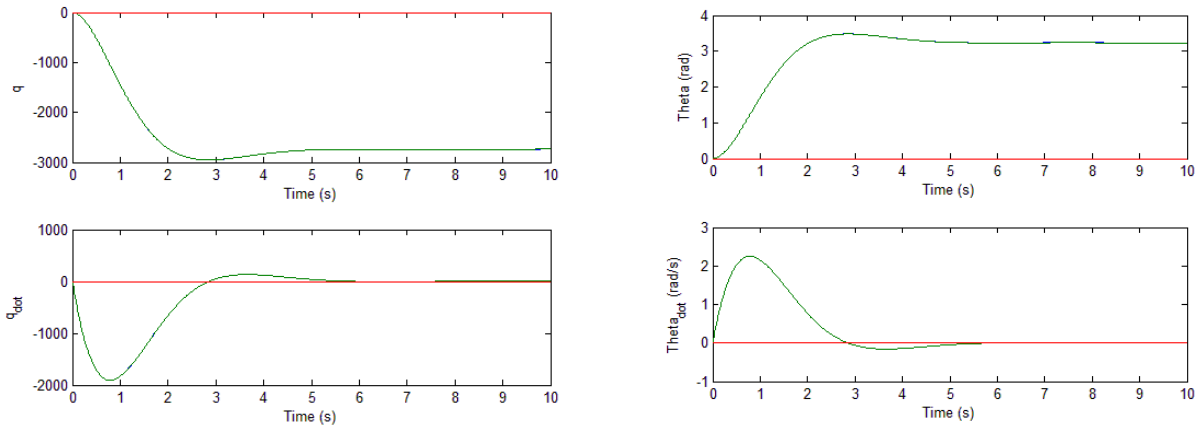


Figure 28: EDT Tip coordinate and EDT base angle with respect to time for a 90 degree slewing maneuver

As one can see from Figure 28, the spacecraft rotates to 90 degrees rather quickly; however, one can also see that the tether tip coordinate is a linear $\sim 2.7\text{km}$ away from the space-beam attached axis. This means that the tether wrapped itself around the satellite as it rotated, and the momentum was not transferred to the entire EDT. This is a result of the low modulus of elasticity compared to its momentum of inertia. As a result, the beam rigidity is very low and will not return to its $y(x, t) = 0$ state if the length becomes too long, as is the case with the EDT.

This type of maneuver might be possible with a much more rigid material for the tether, and a thicker diameter. The other options to maneuver the tether involve complex control systems with thrusters at the tip of the tether in order to coordinate a slewing maneuver with the tip of the tether in order to maintain tension and angular position.

This, however, limits the capability of the mission since its limiting factor becomes the fuel on the tether control system assuming tether libation is an integral part of the mission. Therefore, the control law of changing RAAN with 90 degrees libation can be deemed not feasible for the purpose of this paper.

3.4.2 Position-Optimal EDT orbit rendezvous

A large problem with the control laws outlined previously in this paper is that they all have coupled effects amongst the major orbital elements. Therefore, changing one orbital element at a time results in rather large errors in the state vector since the elements previously matched are changed with the next maneuver. In order to compensate for this problem, San (2002) [27] proposed a linear superposition of currents (I), which was corrected in his later publication [31] such that

$$I = I_{max}(X_1 + X_2 \cos(v) + X_3 \sin(v) + X_4 \cos(2(v + w)) + X_5 \sin(2(v + w))) \quad (3.30)$$

where I_{max} is the maximum allowable current for the maneuver considering all values of w and v , X represents the weighting factor for a given orbital parameter current law, w is the argument of perigee, and v is the true anomaly. The weighting factors follow the following relation

$$[A]t[X] = \Delta \quad (3.31)$$

$$A = \begin{bmatrix} 8Cacos(i) & 8Cae(\cos(i)) & 0 & 0 & 0 \\ 6Cecos(i) & 4Ccos(i) & 0 & Cecos(i) & Cecos(i)\cos(2w) \\ 4Cecos(i) & 0 & 4Ccos(i)/e & -Ccos(i)\sin(2w) & Ccos(i)(\cos(2w) + 1) \\ -2Csin(i) & 0 & 0 & -Csin(i) & 0 \\ 0 & 0 & 0 & 0 & -C \end{bmatrix} \quad (3.32)$$

and a is the semi-major axis, e is the eccentricity, i is the inclination angle, w is the argument of perigee, and

$$C = L \frac{\mu_m}{4mna^4} \quad (3.33)$$

where μ_m is the magnetic moment of the earth, and

$$\Delta = \begin{bmatrix} \Delta a \\ \Delta e \\ \Delta w \\ \Delta i \\ \Delta \Omega \end{bmatrix} \quad (3.34)$$

The matrix in equation 3.32 was derived using the forces on the EDT assuming a dipole model and the equations of motion outlined in equations 3.5-3.10 [27] [31] and serves as a closed form solution.

The current coefficients can therefore be calculated from equation 3.31

$$[X] = \frac{[A]^{-1}\Delta}{t} \quad (3.35)$$

This however, requires knowing the time of flight to rendezvous with the target orbit. This control scheme is implemented as shown in Figure 29.

This method allows rendezvous with target orbits without the coupled effects of the current laws. Using multiple loops of re-calculating the current coefficients based on the satellite's error vector has been shown to reduce the overall error [31].

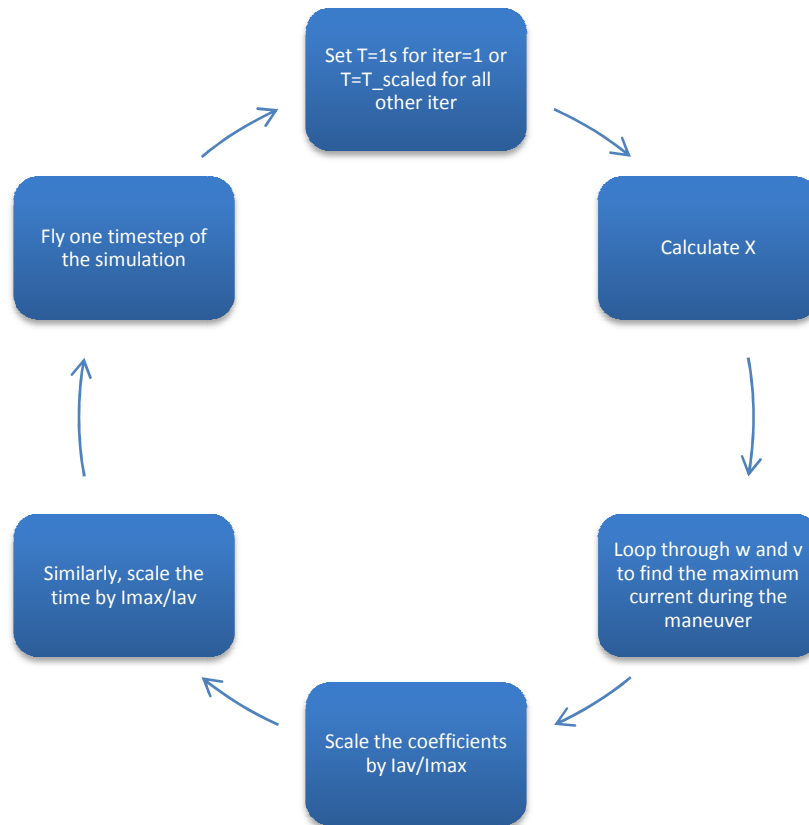


Figure 29: EDT current control scheme

Given the satellites addressed in this paper, using the control law for the full rendezvous was found to take a vast amount of time as the current is modulated to control the other elements and the inclination is very high. Therefore, for time effectiveness while maintaining accuracy, the individual current laws were used to match the orbital elements in order of semi-major axis, eccentricity, inclination, and RAAN. The order was chosen in order of importance to fuel cost for a correction in that orbital element. After the initial rendezvous, the remaining error can be easily corrected, while keeping the other elements constant using the Tragesser method. This adds additional time to the rendezvous but corrects a large piece of the error, saving fuel. The normalized current coefficients for a change in the semi-major axis only and inclination only using the maximum current available (+/- depending on positive change or negative change).

$$X_{SMA} = \pm \begin{bmatrix} -0.4467 \\ 0.0416 \\ 0.0194 \\ 0.8935 \\ 0 \end{bmatrix} I_{av} \quad (3.36)$$

$$X_{INC} = \pm \begin{bmatrix} 0 \\ -0.0123 \\ -0.0225 \\ -0.997 \\ 0 \end{bmatrix} I_{av} \quad (3.37)$$

where I_{av} is the maximum available current throughout the maneuver considering all values of w and v . The cyclical effects of these two current laws are shown in Figure 30 and Figure 32 respectively.

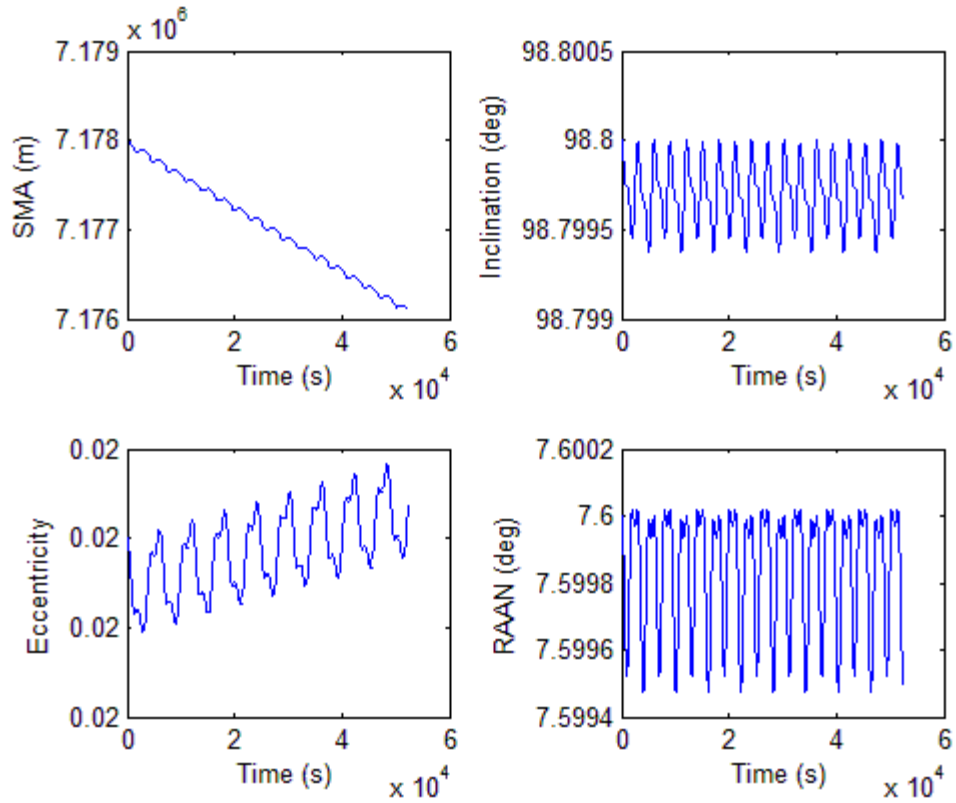


Figure 30: Sample simulation of the current control laws for a change in the semi-major axis of -2km and a time step of 10 seconds.

The cyclical nature of the other elements tends to drift when using larger time steps. Since this drift reduces with decreasing time step it is attributed to computational error, and is therefore ignored in the simulations in section 3.6 and all other elements are assumed to remain constant.

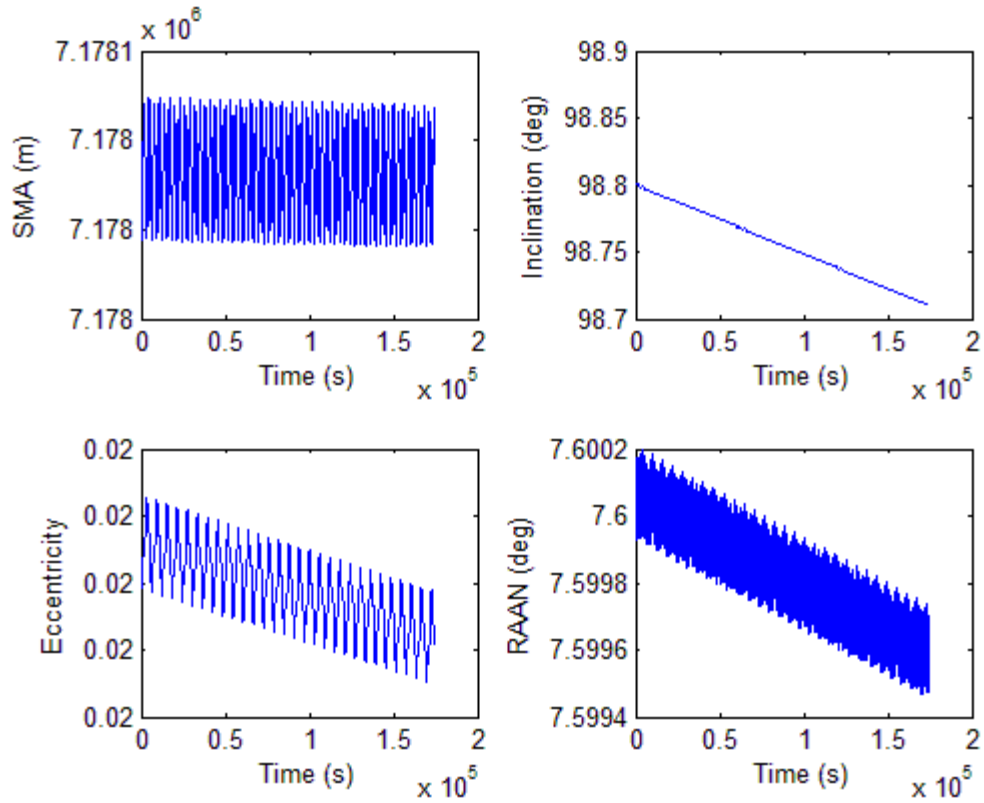


Figure 31: Sample test of the current control laws for an inclination change of -0.1 degrees and a time step of 1 second.

Therefore, the new proposed overall control strategy for the orbital rendezvous is outlined in Figure 32.

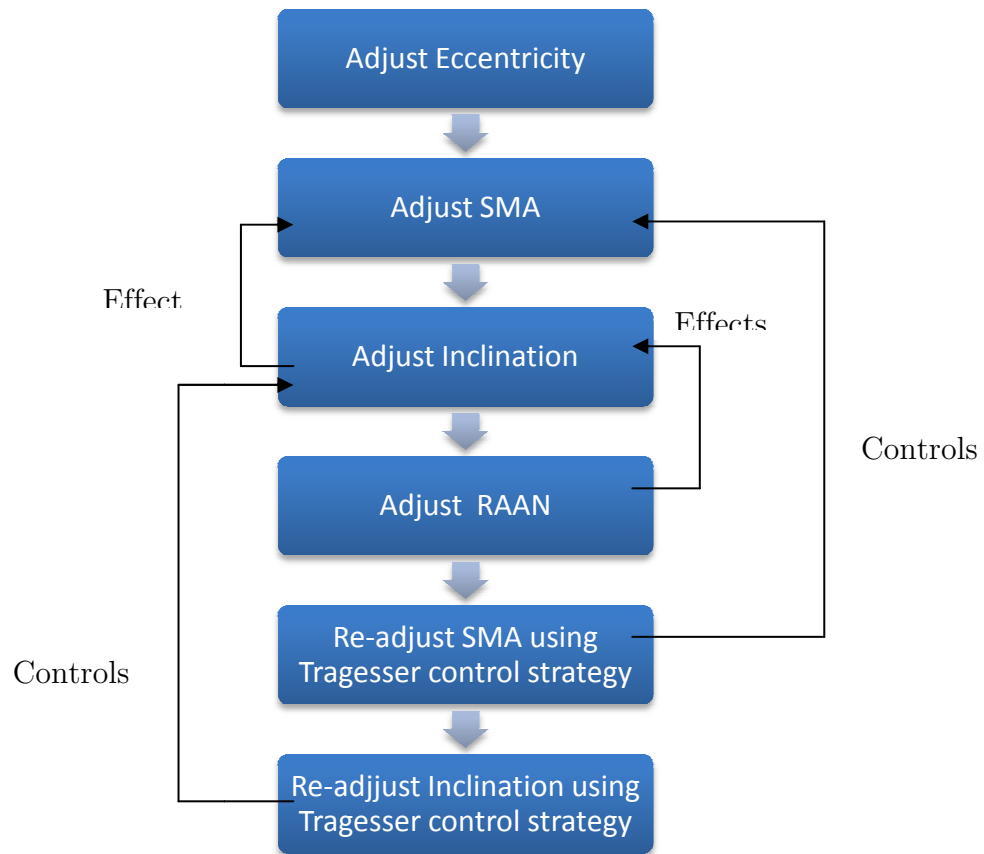


Figure 32: EDT Rendezvous Control Strategy.

This method is much faster to converge as only the final adjustments require the control strategy to 'close the loop'. The overall reward by implementing the final Tragesser control strategy is a much smaller error in the SMA and inclination error.

The traditional current law for de-orbiting is a simple DC current. However, this causes changes in other orbital elements, such as an increase in inclination towards the pole for sun-synchronous orbits. The Tragesser technique has been shown to accurately de-orbit debris while correcting for this drift and maintaining inclination, however the

time required is far too long for any practical implementation due to the high inclination of the orbit and given that the majority of the current is used to modulate the other COE components.

However, bringing the debris to a lower inclination prior to de-orbit providing a buffer zone to accommodate this effect was investigated. On the downside, this adds a considerable amount of time to the total de-orbit mission as a change from 98 degrees to a buffer zone of 105 degrees was required. Therefore, the de-orbit phase of this technology becomes its primary problem area. This problem is hoped to be circumvented using the IBS system for the de-orbit phase, which will be analyzed in the following sections.

3.5 Dynamics and fuel costs of de-orbiting debris using an ion beam

Now that the EDT concept has been evaluated in depth, we take a look at the IBS main aspect of operation; the ion beam. Bombardelli (2011) [19] assumes that the spacecraft mass is much less than that of the debris mass and this results in some simplifications. However, the scenarios investigated in this thesis are not in this regime since even a small satellite of 200kg mass will produce a ratio of 10% with the heaviest objects investigated. Therefore, the optimal exhaust velocity and fuel costs are re-derived below to include the spacecraft mass, as well as the change in the spacecraft mass during de-orbit.

In order to insure that the spacecraft and the debris de-orbit at the same rate, the two accelerations must be equal. From Figure 21 we can conclude that

$$\ddot{x} = \frac{F_{P2} - F_{P1}}{M_s} = E \frac{F_{P1}}{M_d} \quad (3.38)$$

where x is the relative position between the debris and IBS, F_{P1} is the thrust of the engine facing the debris, F_{P2} is the thrust of the engine facing away from the debris, M_s is the spacecraft mass, M_d is the debris mass, and E is the product of the view factor efficiency and the momentum transfer efficiency. The view factor efficiency is outlined in section 3.6 and the momentum transfer is assumed to be equal to 1 due to the high velocity of the exhaust stream

$$E = E_{view} E_{Prop} \quad (3.39)$$

Re-arranging equation 3.38 for $\frac{F_{P2}}{F_{P1}}$ yields

$$\frac{F_{P2}}{F_{P1}} = 1 + \frac{EM_s}{M_d} \quad (3.40)$$

Now given that

$$F_P = \dot{m}c \quad (3.41)$$

and

$$m_{fuel} = \int_{\Delta t} (\dot{m}_{P1} + \dot{m}_{P2}) dt \quad (3.42)$$

We can write the fuel cost in terms of the thrust and exhaust velocity

$$m_{fuel} = \int_{\Delta t} \frac{F_{P1}}{c} + \frac{F_{P2}}{c} dt \quad (3.43)$$

$$m_{fuel} = \int_{\Delta t} \frac{F_{P1}}{c} + \frac{F_{P1} \left(1 + \frac{EM_s}{M_d}\right)}{c} dt \quad (3.44)$$

$$m_{fuel} = \int_{\Delta t} \frac{F_{P1}}{c} \left(2 + \frac{EM_s}{M_d}\right) dt \quad (3.45)$$

$$m_{fuel} = \left(2 + \frac{EM_s}{M_d}\right) \frac{F_{P1}}{c} \Delta t \quad (3.46)$$

where c is the exhaust velocity and Δt is the time required for the maneuver. The mass of the propulsion system also needs to be calculated. Given that the power required for each thruster is proportional to the thrust output we have

$$\frac{P_{P2}}{P_{P1}} = 1 + \frac{EM_s}{M_d} \quad (3.47)$$

where P_{P1} is the power of the thruster facing the debris and P_{P2} is the power of the thruster facing away from the debris. Given the following relations

$$F_{P1} = \frac{2\eta P_{P1}}{c} \quad (3.48)$$

$$m_p = \alpha P \quad (3.49)$$

where α is the inverse of the specific power, called "specific mass" of the power system (kg/W). Now we can write the power system mass as

$$m_{power} = m_{P1} + m_{P2} \quad (3.50)$$

$$m_{power} = \alpha P_{P1} + \alpha P_{P2} \quad (3.51)$$

$$m_{power} = \alpha P_{P1} + \alpha P_{P1} \left(1 + \frac{EM_s}{M_d}\right) \quad (3.52)$$

$$m_{power} = \alpha P_{P1} \left(2 + \frac{EM_s}{M_d} \right) \quad (3.53)$$

$$m_{power} = \alpha \frac{F_{P1} c}{2\eta} \left(2 + \frac{EM_s}{M_d} \right) \quad (3.54)$$

The total spacecraft mass can then be written as

$$m_{ISB} = m_{fuel} + m_{power} + m_{structural} \quad (3.55)$$

$$m_{ISB} = \left(2 + \frac{EM_s}{M_d} \right) \frac{F_{P1}}{c} \Delta t + \alpha \frac{F_{P1} c}{2\eta} \left(2 + \frac{EM_s}{M_d} \right) + m_{structural} \quad (3.56)$$

Taking a derivative with respect to c and setting it equal to zero yields

$$\frac{dm_{ISB}}{dc} = - \left(2 + \frac{EM_s}{M_d} \right) \frac{F_{P1}}{c^2} \Delta t + \alpha \frac{F_{P1}}{2\eta} \left(2 + \frac{EM_s}{M_d} \right) = 0 \quad (3.57)$$

Solving for c gives the optimal exhaust velocity which corresponds to the Irving-Stuhlinger characteristic velocity

$$c = \sqrt{\frac{2\eta\Delta t}{\alpha}} \quad (3.58)$$

Plugging back into the equation for total spacecraft mass yields

$$m_{ISB} = \left(2 + \frac{EM_s}{M_d} \right) \frac{F_{P1}}{\sqrt{\frac{2\eta\Delta t}{\alpha}}} \Delta t + \alpha \frac{F_{P1} \sqrt{\frac{2\eta\Delta t}{\alpha}}}{2\eta} \left(2 + \frac{EM_s}{M_d} \right) \quad (3.59)$$

+ $m_{structural}$

$$m_{ISB} = \left(2 + \frac{EM_s}{M_d} \right) \left(F_{P1} \sqrt{\frac{\alpha\Delta t}{2\eta}} + F_{P1} \sqrt{\frac{\alpha\Delta t}{2\eta}} \right) + m_{structural} \quad (3.60)$$

$$m_{ISB} = 2 \left(2 + \frac{EM_s}{M_d} \right) \left(F_{P1} \sqrt{\frac{\alpha\Delta t}{2\eta}} \right) + m_{structural} \quad (3.61)$$

where the fuel mass is given by

$$m_{fuel} = \left(2 + \frac{EM_s}{M_d}\right) \left(F_{P1} \sqrt{\frac{\alpha \Delta t}{2\eta}}\right) \quad (3.62)$$

This equation, however, does not take into account the changing mass of the spacecraft as it propagates through the maneuver. Therefore, an estimate for the total mission time is found in Bombardelli et al (2011) [32] using the constant debris mass

$$\Delta T = \frac{\sqrt{r} - \sqrt{r_0}}{\epsilon \sqrt{r_0}} \quad (3.63)$$

$$\epsilon = \frac{EF_{P1}}{M_d \mu} \quad (3.64)$$

From this we can estimate the optimal exhaust velocity

$$c_{opt} = \sqrt{\frac{2\eta M_d \mu}{\alpha EF_{P1}} \left(\frac{\sqrt{r} - \sqrt{r_0}}{\sqrt{r_0}}\right)} \quad (3.65)$$

where M_d is the debris mass, μ is the standard gravitational parameter for earth, r is the desired orbital radius, and r_0 is the current orbital radius. This velocity can change depending on the mission parameters and debris mass. Therefore, for multiple mission usage, the largest exhaust velocity will determine the mass of the power system required for the overall mission lifetime. The exhaust velocity corresponding to the largest power supply required can then be used for all waypoints to minimize the fuel cost for the other waypoints since the power supply is already set to a specific value. From this point, the mass flow rates are found and summed at every time-step in the simulations to provide the actual change in satellite mass as it propagates.

$$\dot{m}_1 = \frac{F_{P1}}{c_{opt}} \quad (3.66)$$

$$\dot{m}_2 = \dot{m}_1 \left(1 + \frac{EM_s}{M_d} \right) \quad (3.67)$$

$$m_{fuel_{incremental}} = \frac{F_{P1}}{c_{opt}} \left(2 + \frac{EM_s}{M_d} \right) * timestep \quad (3.68)$$

$$m_{fuel} = \sum_{iteration=0}^{deorbit} \frac{F_{P1}}{c_{opt}} \left(2 + \frac{EM_s}{M_d} \right) * timestep \quad (3.69)$$

Ideally, the fuel cost equation 3.69 could be expanded to compensate for the difference in ballistic coefficients between the IBS and the debris. However, accurate drag coefficients for high altitude orbits are still under development.

3.6 Ion Beam Physics

An efficiency term E was previously defined in section 3.5. This term arises from the view factor between the ion beam and the debris object as well as other factors like charge exchange collisions and interactions with the background fields. The view factor is a function of the beam divergence, which will be analyzed with an analytical model.

background fields.

3.6.1 Ion Beam far-field plume divergence

As an ion beam leaves the thruster, it undergoes a transition period where it is still under the effects of the electromagnetic fields of the thruster, as well as plasma

inhomogeneities. These factors along with the grids and the neutralizing beam are primarily responsible for the initial expansion [33]. In the far-field region, the plasma expansion is primarily caused by the plasma's residual pressure and the internal ambipolar electric fields [33]. In order to investigate the divergence of the ion beam as it propagates through space, a MATLAB code was written based on the equations derived by Parks and Katz (1979) [34] and simplified by Bombardelli et al (2011) [32] and ESA (2011) [35].

The far-field plume model assumes an axis-symmetric plume which is far enough away from the thruster optics so that electromagnetic fields and non-uniformities resulting from the mixing of streams can be neglected. Therefore, the plasma can be modeled as a fluid obeying the equations

$$u_{zi} \frac{\partial \ln(n)}{\partial z} + u_{ri} \frac{\partial \ln(n)}{\partial r} + \frac{\partial u_{zi}}{\partial z} + \frac{1}{r} \frac{\partial (ru_{ri})}{\partial r} = 0 \quad (3.70)$$

$$u_{zi} \frac{\partial u_{zi}}{\partial z} + \frac{u_{ri} \partial u_{zi}}{\partial r} + \left(\frac{e}{m_i} \right) \frac{\partial \phi}{\partial z} = 0 \quad (3.71)$$

$$\frac{u_{zi} \partial u_{ri}}{\partial z} + \frac{u_{ri} \partial u_{ri}}{\partial r} + \left(\frac{e}{m_i} \right) \frac{\partial \phi}{\partial r} = 0 \quad (3.72)$$

$$\frac{1}{n} \nabla n T_e - e \nabla \phi = 0 \quad (3.73)$$

where u_{zi} is the ion velocity in the axial direction, u_{ri} is the ion velocity in the radial direction, r is the radial coordinate, n is the particle density, e is the charge of the ions,

m_i is the ion mass, ϕ is the electric potential, and T_e is the electron temperature. In Parks and Katz (1979) [34], the authors assumed that the axial velocity is constant, so that

$$u_z(r, z) = u_0 \quad (3.74)$$

A further assumption is that the flow is considered isothermal. The plasma density and radial velocity are derived in detail in Merino, Mario (2011) [33], and the result is

$$n(r, z) = \frac{n_0}{h(z)^2} \exp\left(-\frac{3r^2}{h(z)^2 R_0^2}\right) \quad (3.75)$$

$$u_r(r, z) = u_0 r \frac{h'(z)}{h(z)} \quad (3.76)$$

where $h(z)$ and $h'(z)$ are defined by the following self-similar function

$$\frac{dh}{dz} = \sqrt{\frac{12}{M^2} \ln(h) + h_0'^2} \quad (3.77)$$

$$h(0) = 1 \quad (3.78)$$

where M is the mach number of the ion beam. Given the ion engine attributes outlined in ESA (2011) [35], listed in Table 10, a MATLAB model was written and analyzed. The results of this simulation yielded Figure 33 plotting the ion density with respect to axial and radial distance. The ion beam is assumed to be perfectly symmetrical in the theta direction; therefore a 2D quadrant is sufficient to characterize the entire beam profile.

Table 10: Ion Thruster Parameters.

Initial radius (R0)	0.1m
Initial mean plasma density (n0)	2.6e16 m ³
Initial ion axial velocity	38000 m/s
Electron Temperature	5eV
Ion Kinetic Energy	5keV
Initial plasma mach number (M)	20
Initial Beam Divergence parameter	0.2

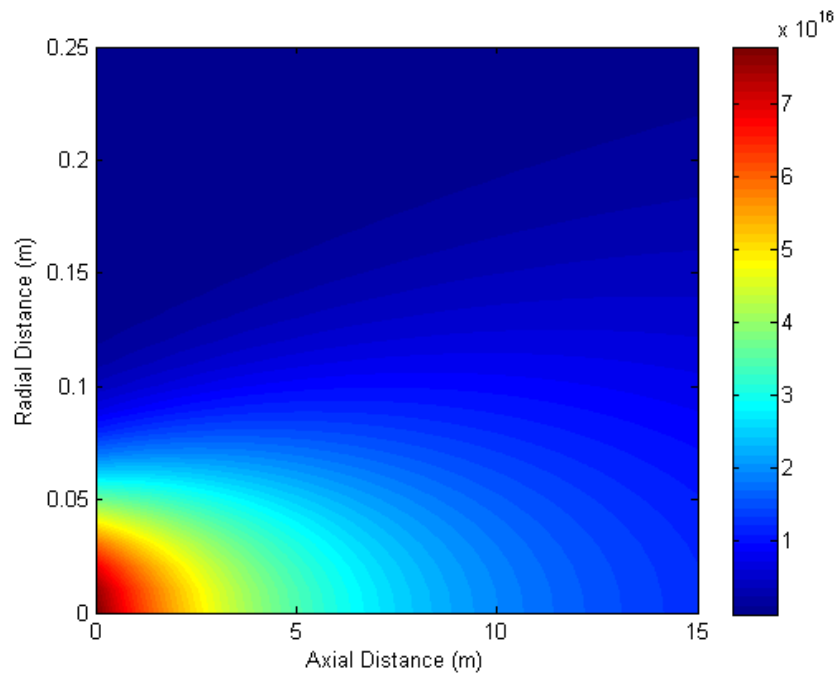


Figure 33: Parks and Katz model of far-field plume divergence via MATLAB simulation.

The question to be investigated is the amount of momentum transferred to the debris object by the beam. Ignoring collisions allows us to assume that the mass flow rate and flux of particles remain constant along the axial direction. Therefore the problem becomes a simple matter of how many particles are impacting the debris with respect to the total number of particles at any given radial cross section.

$$E_{view} = \frac{n_{impact}}{n_{total}} \quad (3.79)$$

This, naturally, depends on the size of the debris object

$$E_{view} = \frac{\int_A n dA}{n_0 * r_{thruster}} \quad (3.80)$$

where n_0 is the initial number density at the thruster exit, $r_{thruster}$ is the thruster radius, n is the number density of particles at the debris surface per unit area, and dA is the differential area element. In order to draw some preliminary conclusions about the separation distance where the beam divergence becomes noticeable, we take a look at the radial cross section profile of the density in Figure 34.

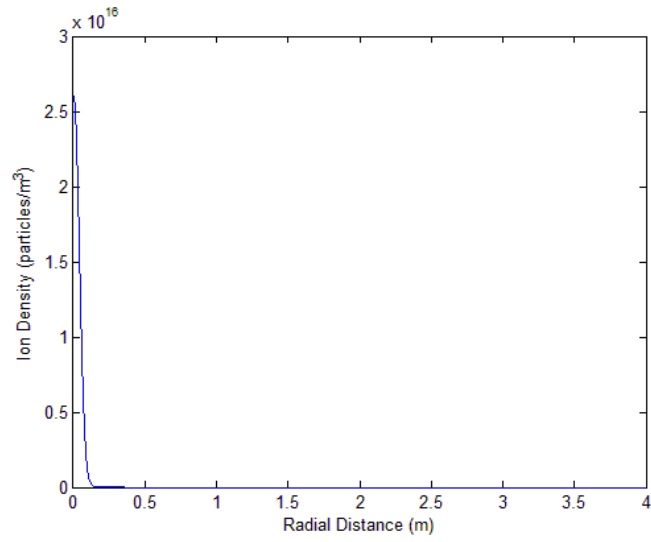


Figure 34: Ion density cross section at $z=0$.

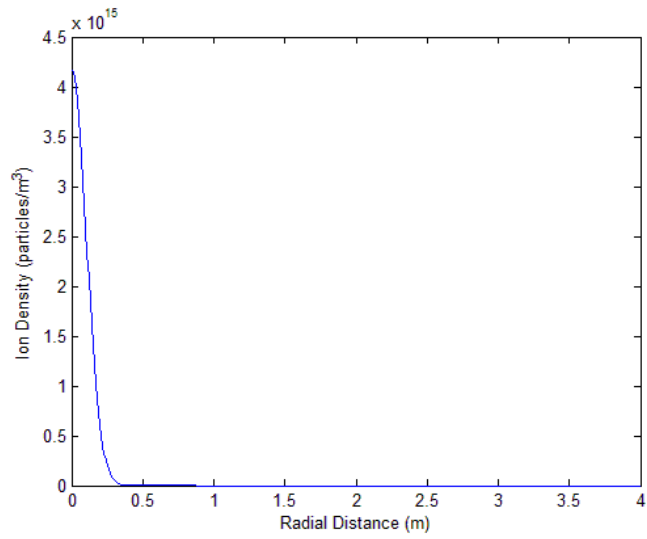


Figure 35: Ion density cross section at $z=5$ m.

We can see that this curve follows a Gaussian distribution, which means that $\sim 95\%$ of all of the particles will fall within $\pm 2\sigma$ of $r=0$. Furthermore, we can see how this profile changes similar to thermal expansion.

In order to get an idea of how the beam divergence effects the effective radius of the beam, defined by $r=2\sigma$, we take a look at the standard deviation over axial distance shown in Figure 36.

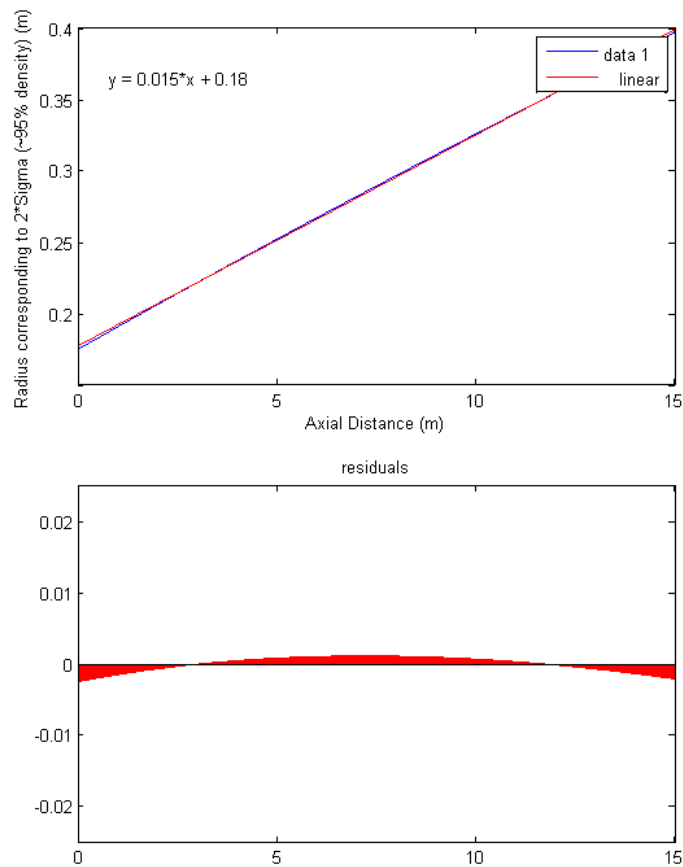


Figure 36: 2 sigma radius vs. axial distance of the plume.

From this plot, we can see that the 2σ radius evolves almost linearly with time at a slope of 0.015 m/m. Given the dimensions of the debris instigated in this report, the view factor does not become relevant until approximately $z=100\text{m}$ where the 2σ radius corresponds to 1.5m. Assuming that the IBS system operates well below this range, and that the pointing vector is perfectly aligned with the debris, it is concluded that $E_{view} = 1$ for the simulations in section 3.6. This effect becomes more significant with smaller debris dimensions, and the profile could significantly change with the inclusion of external and internal electromagnetic fields.

This P-K model neglects particle collisions, charge exchange, and external/internal fields. ESA (2011) [35] investigates some of these aspects such as background magnetic field and charge exchange collisions (CEX), but concludes that " a more detailed study of the plasma expansion with full simulation of induced field, electron inertia, 3D effects and the role of the Hall parameter is advised.". Given the scope of this research, the full models of the expansion interactions are left for future work.

3.6.3 CEX Collisions

A preliminary analysis of the charge exchange collisions is performed. During a charge-exchange collision (CEX), a fast moving Xenon ion collides with a slow moving neutral Xenon ion, exchanges velocity but keeps its charge

$$Xe_{fast}^+ + Xe_{slow} = Xe_{fast} + Xe_{slow}^+ \quad (3.81)$$

These slow moving ions are then subject to the radial potential drop across the beam and are accelerated outwards. Furthermore, if the CEX occurs close enough to the thruster exit, the thruster's fields cause significant charge buildup around the sides of the thruster. The average charge exchange ion production rate is given by Wang et al (2001) [36]

$$\frac{dn_{cex}}{dt} = n_b n_n v_b \sigma_{cex} \quad (3.82)$$

where n_b is the average beam ion density, n_n is the average neutral density, v_b is the beam velocity, and σ_{cex} is the collision cross-section. The cross section is estimated from fitting experimental data performed by Rapp, 1962, and Roy et al. 1996.

$$\sigma_{cex} = (k_1 \ln(v_b) + k_2)^2 10^{-20} \quad (3.83)$$

$$k_1 = -0.8821 \quad (3.84)$$

$$k_2 = 15.1262 \quad (3.85)$$

The neutral density is given by Roy (1995) [37] as

$$n_n(R, \Theta) = \left(1 - \frac{1}{\sqrt{2}}\right)^{-1} \frac{n_{n0}}{2} \left[1 - \sqrt{1 + \left(\frac{r_t}{(r^2 + (z+r_t)^2)^{\frac{1}{2}}}\right)^2}\right] \cos\left(\text{atan}\left(\frac{r}{z+r_t}\right)\right) \quad (3.86)$$

where n_{n0} varies between $3\text{E}16\text{m}^{-3}$ and $3\text{E}17\text{m}^{-3}$, r is the radial direction, and z is the axial direction.

However, for the purposes of this investigation we are only interested in an axial variation. Using the equations above, and given that the CEX production is a direct result of ion beam loss, we can state the equation for the change in ion density with respect to axial distance from Blandino (2000) [38]

$$\frac{dn_b}{dz} = -n_b n_n \sigma - n_b 2 \frac{\lambda}{r} \quad (3.87)$$

$$\lambda = \tan(\alpha) \quad (3.88)$$

where α is the beam half-angle and λ represents the loss of density due to expansion of the beam. Combining this equation with the previous model for the plume divergence given by Parks and Katz (1979) [34] allows the second term to be neglected and will give an ion density profile of the beam including CEX. For the aspect of momentum transfer, we do not care if the particle is neutral or an ion. However, this difference is important when considering the behavior of the plume as plasma. The primary force on the plume, with or without a magnetic field, is the Lorentz force; which is null for a neutral particle.

The change in ion density due to CEX could affect parameters such as plume divergence since the neutrals will not contribute to the charge density hence Poisson's equation will yield different potential and different forces. Furthermore, under the influence of magnetic and electric fields, these neutrals could follow a far different bulk motion than the ions, which could result in two separate streams of molecules.

Equation 3.87 is combined with equation 3.77 and 3.75 to produce the ion density variation with charge exchange collisions. The equation that was followed is shown below

$$n_{WithCEX}^{z,r} = n^{z-1,r} + \frac{dn_b(n_b^{z-1,r}, n_n^{z-1,r})}{dz} \underset{RK4}{+} \frac{dn_{noCEX}}{dz} \quad (3.89)$$

$$\frac{dn_{noCEX}}{dz} = n_{noCEX}^{z,r} - n_{noCEX}^{z-1,r} \quad (3.90)$$

The last term is responsible for the expansion of the plume due to the self-similar model, and the second term is responsible for the collisions. The initial condition at $z=0$ is such that the density with and without CEX is equal.

The contour profile of the neutral population given by equation 3.86, assuming a thruster population of $1e17 \text{ m}^{-3}$, is shown in Figure 37.

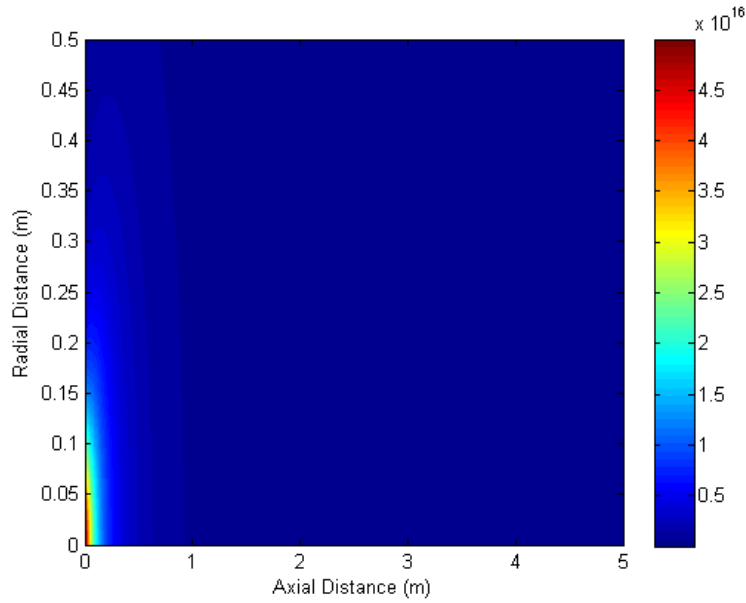


Figure 37: Neutral Density Profile.

One can see that the majority of the neutral population is centered around the thruster exit, and drops off very quickly with respect to both radial and axial distance. However, due to the exponential nature of the function, the neutral density doesn't reach zero at the boundaries of the box. This effect will become apparent when we look at the density profiles of the CEX model. The ratio of $\frac{n_{withCEX}}{n_{noCEX}}$ is shown in Figure 38.

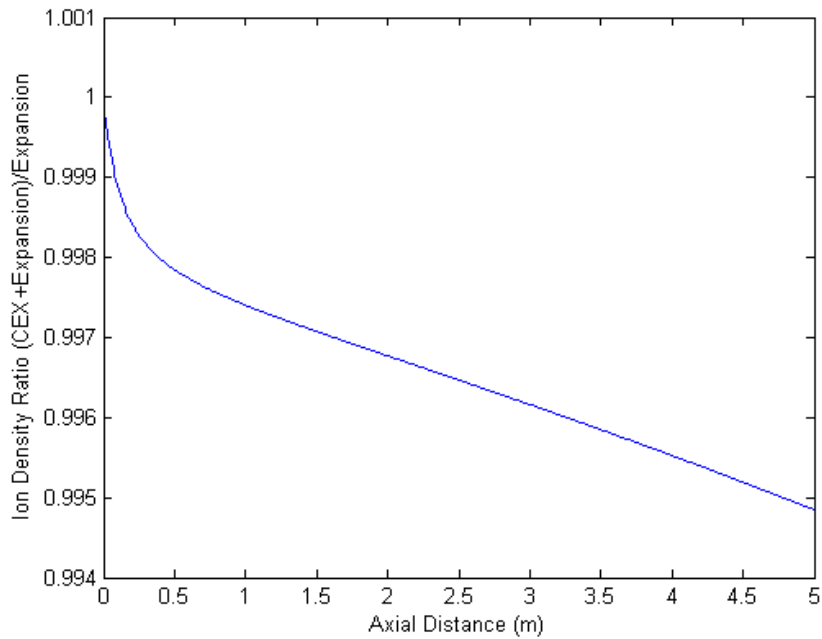


Figure 38: Ratio of Ion Densities with CEX to without CEX.

The constant gradient of the ratio is due to the almost constant neutral density profile far away from the thruster exit. This effect is due to an assumption that a constant ambient background pressure exists. After 5 meters, the beam has lost about 0.5% of its density due to collisions. Therefore at 10 meters, assuming the constant nature of the ratio, less than 1% of the ion density will be converted to neutrals. Assuming a worst case scenario of all of the neutrals missing the target, this effect will still be negligible in terms of momentum transfer. On the other hand, looking at the density of CEX ions generated, shown in Figure 39, we can see that the majority of the CEX ions are generated within 1 meter of the thruster exit.

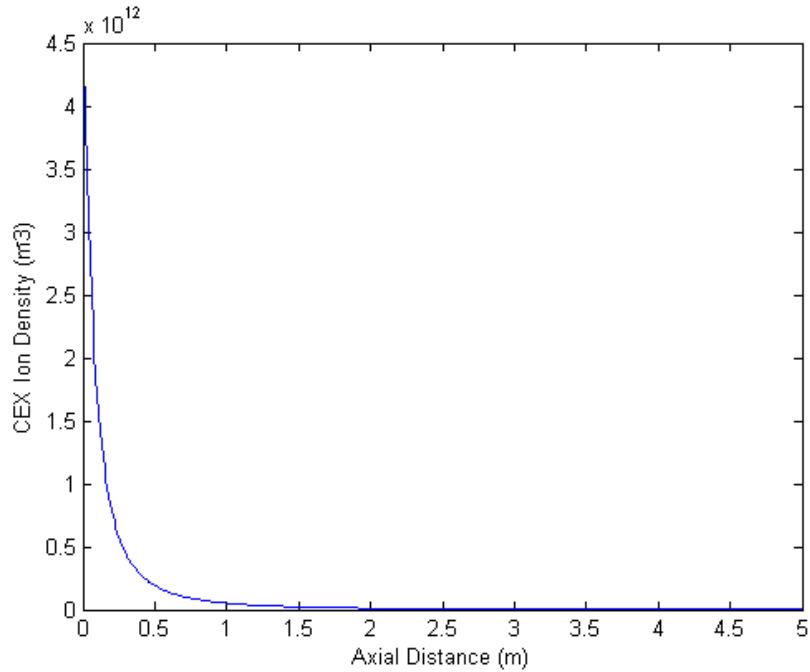


Figure 39: CEX density with respect to axial distance at $r=0$.

This poses an issue as in the order of 10^{12} xenon ions are now very close to the thruster exit moving at very slow speeds corresponding to the Maxwellian thermal velocity of the neutrals. These ions are subject to not only the electric field generated by the ion beam potential gradient, but also the thruster fields. This is a major cause of spacecraft charging, which will not be investigated in this report.

3.6.3 Beam-plasma instabilities

The last aspect to be investigated is the possibility of beam-plasma instabilities. Two or more interacting plasma streams can cause instabilities to grow due to the oscillations of the ions and electrons, which can create potential holes that grow over time. An example of such instability is the classic two-stream instability. The initial conditions and dispersion relation is given by Birdsall and Langdon (2005) [39] as Figure 40 and equation 3.91.

$$\omega = \pm \left(k^2 v_0^2 + \omega_p^2 \pm \omega_p (4k^2 v_0^2 + \omega_p^2)^{\frac{1}{2}} \right)^{\frac{1}{2}} \quad (3.91)$$

where ω_p is the plasma frequency, v is the group velocity, and k is a mode. This yields a frequency-mode phase space plot indicating the maximum growth rate is $\frac{\omega_p}{2}$ shown in Figure 41.

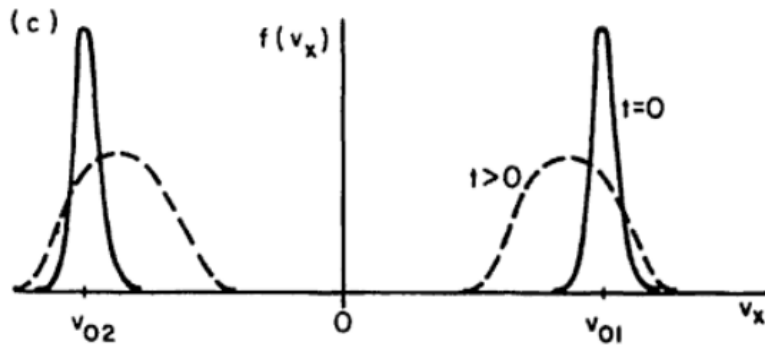


Figure 40: Two-stream instability initial conditions [39].

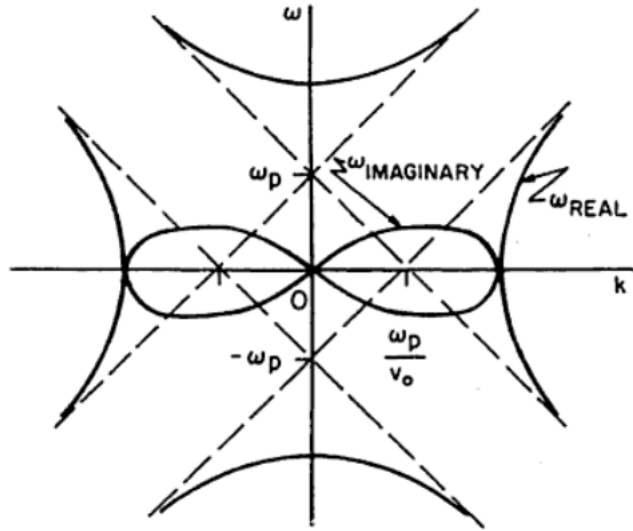


Figure 41: Dispersion relation for the two-stream instability [39].

However, this scenario assumes two opposing electron streams. Since the scenario of ion beam momentum transfer for de-orbit involves an ion stream in background plasma consisting of both electrons and ions, a more fitting scenario is that of the beam driven ion beam-plasma interaction. This instability is investigated by Treumann and Baumjohann (1997) [40] under the category of ion-acoustic waves. The initial conditions of the system are displayed in Figure 42.

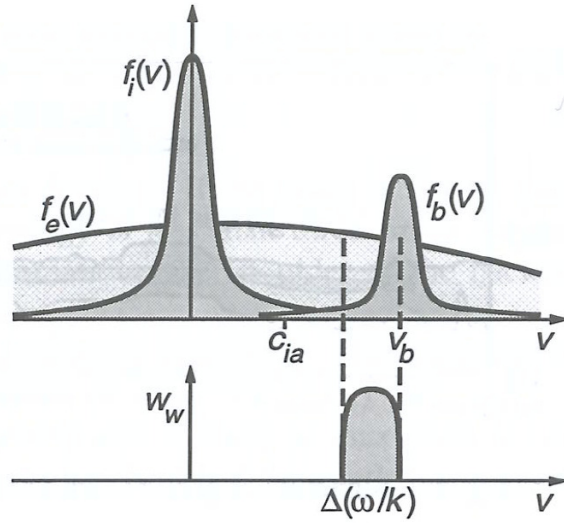


Figure 42: beam driven ion-acoustic-unstable velocity space distribution [40].

These kinds of instabilities are usually found in the auroral ionosphere during active auroras and sub storms [40]. However, ion-acoustic waves occur in most electric thruster plasmas [41]. The only part of Figure 42 that does not match the scenario at hand is the hot background electrons.

However, significant electron velocity dispersion can occur in an ion-beam-plasma instability as investigated in Rowe (1972) [42]. Figure 43 outlines the results of Rowe's simulation, particularly the dispersion of the background electron velocities as well as a slight perturbation in the beam ions.

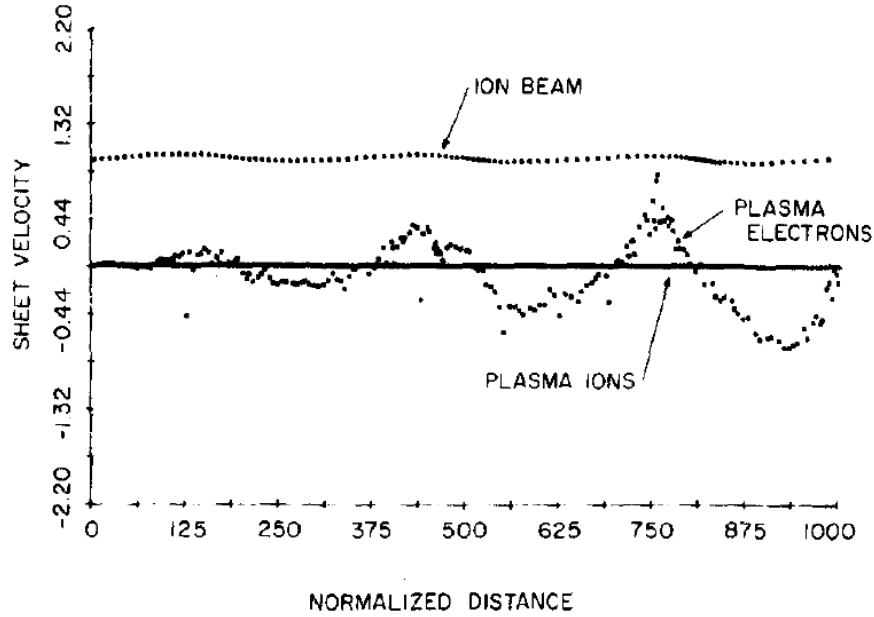


Figure 43: Ion-beam plasma instability ($t=120/wp_0$), $m_i/m_e=1000$, $L=3$ wavelengths [42].

This ion-beam plasma instability could give rise to the hot background electrons present in the beam-driven ion-acoustic instability shown in Figure 42. This gives rise to a hypothesis that there might exist a chain of instabilities starting with the ion-beam plasma instability which later develops into ion-acoustic instabilities.

Given that the desired profiles have been established, the growth rate of the beam driven ion-acoustic instability is given by Treumann and Baumjohann (2005) [40] as

$$\gamma_{iab} = \left(\frac{\pi}{8}\right)^{\frac{1}{2}} \frac{w^4}{w_{pi}^2 |k|^3 c_{ia} \lambda_D^2} \left\{ \frac{n_{ib}}{n_0} \left(\frac{T_e}{T_{ib}}\right)^{\frac{1}{2}} \left(\frac{kv_b}{w} - 1\right) \exp\left(-\frac{(w - kv_b)^2}{k^2 v_{thib}^2}\right) - \left(\frac{m_e}{m_i}\right)^{\frac{1}{2}} \exp\left(-\frac{w^2}{k^2 v_{the}^2}\right) \right\} \quad (3.92)$$

where w_{pi} is the ion plasma frequency, c_{ia} is the ion sound velocity, λ_D is the Debye length, k is the mode, n_{ib} is the ion beam density, n_0 is the background density, v_b is the beam group velocity, v_{thib} is the ion beam thermal velocity, T_e is the electron temperature, T_{ib} is the ion beam temperature, m_e is the electron mass, and m_i is the ion mass. Equation 3.92 follows the instability criterion of

$$v_{ib} > c_{ia} \quad (3.93)$$

These instabilities become an important factor in the IBS design, due to the fact that ion-acoustic waves generate density irregularities, which could alter the momentum transfer to the target. Furthermore, the beam-plasma instability might reduce the average velocity of the beam and hence the momentum carried by the beam which has direct impact on its efficiency. Further investigation into this topic is out of scope for this thesis and is recommended for further research.

3.7 State-feedback control system for relative position holding and rendezvous

So far we have outlined the technical concepts and investigations of all the separate technologies. A more detailed look at the operational aspects of the desired mission yields some common difficulties. For instance, as with all technologies that are investigated within this paper, the spacecraft requires a near-perfect rendezvous. Unfortunately, due to the oscillatory nature of the orbital elements while using EDTs, the rendezvous capabilities of the EDT are limited to large-scale maneuvers. Therefore, we take a moment here and analyze the system required for impulsive thruster final rendezvous and relative position holding which are applicable to all technologies.

A control system is outlined and designed in this section to maintain constant separation between the spacecraft and the debris. In order to satisfy the operational requirements of the IBS, the out-of-plane motion is minimized so that the ion thruster always faces its target. If this were not the case, this would result in an off-center force to the debris, causing unwanted attitude effects as well as lowering the efficiency of the de-orbit engine.

When the separation between the two satellites becomes very small, as shown in Figure 44, the governing equations of the relative motion are given by the Clohessy-Wiltshire equations [43].

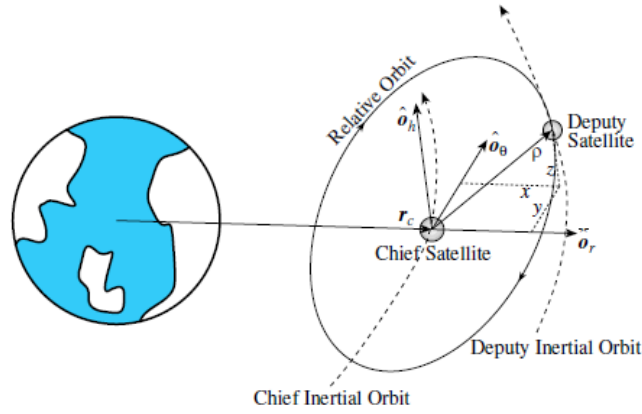


Figure 44: IBS-Debris problem formulation [44].

In our previous discussion on plume divergence we determined that the divergence is irrelevant at distances less than 100m. Taking this 100m limit as an operational requirement, the linearized C-W equations are satisfactory, especially since the position holding is within the same orbit [44]. A further criterion is the circular orbit of the leader and follower. This is a justified assumption due to the small rate of decay allowing the orbit to evolve quasi-circularly.

$$\ddot{x} - 2n\dot{y} - 3n^2x = 0 \quad (3.94)$$

$$\ddot{y} + 2n\dot{x} = 0 \quad (3.95)$$

$$\ddot{z} + n^2z = 0 \quad (3.96)$$

where x , y , and z are target-body-fixed coordinates. In order to start formulating a control scheme for these equations, we define the control inputs and equations of motion as

$$U = \begin{bmatrix} u_x \\ u_y \\ u_z \end{bmatrix} \quad (3.97)$$

$$\ddot{x} - 2n\dot{y} - 3n^2x = \frac{u_x}{m} \quad (3.98)$$

$$\ddot{y} + 2n\dot{x} = \frac{u_y}{m} \quad (3.99)$$

$$\ddot{z} + n^2z = \frac{u_z}{m} \quad (3.100)$$

where u_x , u_y , and u_z are the control inputs, m is the chase mass, and n is the orbital rate. From this point, we can define the relative position control system in state-space form in terms of the control feedback inputs u , and the state vector $x(t) = [x \ y \ z \ \dot{x} \ \dot{y} \ \dot{z}]^T$

$$\dot{x}(t) = Ax(t) + Bu(t) \quad (3.101)$$

$$y(t) = Cx(t) + Du(t) \quad (3.102)$$

$$u(t) = Kx(t) \quad (3.103)$$

where A is the equations of motion matrix corresponding to the LHS of equations 3.94-3.96, B is the control inputs corresponding to the RHS of equations 3.94-3.96, C is the output matrix, and D is the feed-forward matrix. In order to obtain the A and B matrix, we analyze equation 3.104

$$\dot{x}(t) = \begin{bmatrix} \dot{x} \\ \dot{y} \\ \dot{z} \\ \ddot{x} \\ \ddot{y} \\ \ddot{z} \end{bmatrix} = A \begin{bmatrix} x \\ y \\ z \\ \dot{x} \\ \dot{y} \\ \dot{z} \end{bmatrix} + B \begin{bmatrix} u_x \\ u_y \\ u_z \end{bmatrix} \quad (3.104)$$

By creating a 6x6 matrix A, and a 6x3 matrix B, this equation can be satisfied.

The top 3x3 section of matrix B is empty due to the fact that control forces act on the accelerations only in correspondence with Newton's laws of motion.

$$A = \begin{bmatrix} 0 & 0 & 0 & 1 & 0 & 0 \\ 0 & 0 & 0 & 0 & 1 & 0 \\ 0 & 0 & 0 & 0 & 0 & 1 \\ 3n^2 & 0 & 0 & 0 & -2n & 0 \\ 0 & 0 & 0 & -2n & 0 & 0 \\ 0 & 0 & -n^2 & 0 & 0 & 0 \end{bmatrix} \quad (3.105)$$

$$B = \begin{bmatrix} 0 & 0 & 0 \\ 0 & 0 & 0 \\ 0 & 0 & 0 \\ \frac{1}{m} & 0 & 0 \\ 0 & \frac{1}{m} & 0 \\ 0 & 0 & \frac{1}{m} \end{bmatrix} \quad (3.106)$$

The C matrix is chosen based on the output variables of the state-space problem.

It is assumed that the full set of six state variables can be measured by navigation systems making C a 6x6 identity matrix. D is chosen as a 6x6 null matrix. Now that the state-space problem has been formulated, the question of controlling the system remains.

A common practice for solving multiple-input-multiple-output (MIMO) problems such as this is the Linear Quadratic Regulator (LQR) method. The gain matrix K in equation 3.103 can be found by minimizing the linear quadratic performance index [43]

$$J = \frac{1}{2} \int_0^{\infty} (x^T Q x + u^T R u) dt \quad (3.107)$$

where Q and R are state and control input weighting matrices. K is obtained by solving the algebraic Riccati equation [43]

$$0 = A^T X + X A - X B R^{-1} B^T X + Q \quad (3.108)$$

MATLAB has a built-in function "LQR(A,B,Q,R)" which performs this optimization for the user and outputs the gain matrix K . Four conditions are outlined in Wie (2008) [43] so that a unique positive-definite solution of the Riccati equation exists

1. Q must be symmetric and positive semi definite
2. R must be symmetric positive definite
3. The pair (A,B) must be controllable
4. The pair (A,H) must be observable where $H^T H = Q$ and $\text{rank } H = \text{rank } Q$

In order to easily satisfy requirements 1, 2, and 4 the Q and R matrices are chosen to be the appropriately sized identity matrix. To test the controllability of the (A,B) matrix pair, we define a matrix R

$$R = [B \ AB \ A^2 B \ \dots \ A^{n-1} B] \quad (3.109)$$

If this matrix R has full rank, then the system is controllable. This can easily be verified using the MATLAB "rank(A)" function. For the given scenario we have

$\text{rank}(R)=6$ which is equal to the number of inputs, therefore it is full rank and satisfies the third requirement.

We developed a Simulink model employing state-feedback control and utilizing the LQR gain matrix from the MATLAB function, shown in Figure 45. A saturation block was implemented to constrain the thrust applied to the spacecraft to the maximum output of the proposed thrusters.

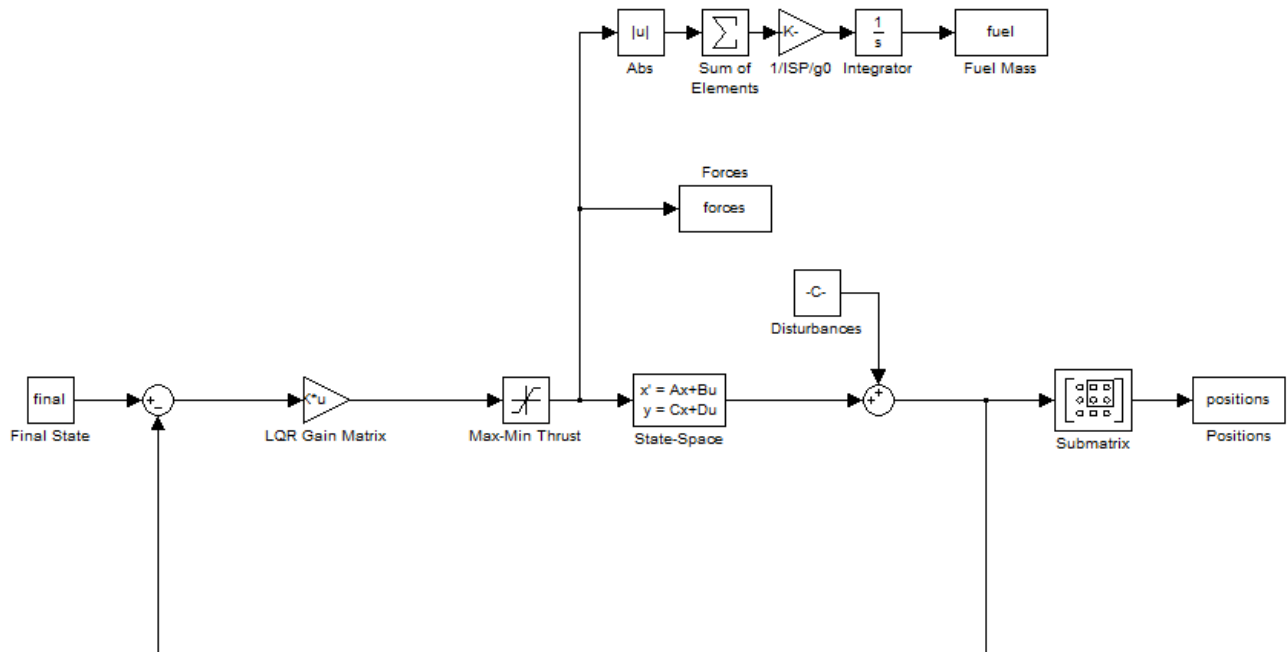


Figure 45: Simulink block diagram for state-feedback system using LQR for relative spacecraft position control.

Furthermore, a branch was added at the top of the model to calculate the cumulative fuel usage to perform the final rendezvous and position holding for investigational purposes. The fuel usage was based on the equation for ISP

$$F = ISP\dot{m}g_0 \quad (3.110)$$

$$m = \int \frac{F}{ISP * g_0} \quad (3.111)$$

where \dot{m} is the mass flow rate, ISP is the specific impulse, and g_0 the acceleration due to earth's gravity.

3.7.1 Control system simulation results using LQR gain matrix

The control thrusters were assumed to be MR-106 Redmond hydrazine monopropellant rocket engines [45], having a maximum thrust of

$$u_{\max} = 27N \quad (3.112)$$

To simulate the final stages of the rendezvous the initial state, final state, and disturbances were set to

$$x_0 = [-100 \quad 20 \quad -50 \quad 0 \quad 0 \quad 0]^T \quad (3.113)$$

$$x_f = [0 \quad -50 \quad 0 \quad 0 \quad 0 \quad 0]^T \quad (3.114)$$

$$x_d = [0 \quad 0 \quad 0 \quad 0 \quad 0.1 \quad 0]^T \quad (3.115)$$

where \mathbf{x}_0 is the initial position of the chase with respect to the target, \mathbf{x}_f is the final relative position, and \mathbf{x}_d is the disturbance displacement. The spacecraft mass and altitude were set to a 200kg and 800km, giving an angular rate of

$$n = \sqrt{\frac{3.986E14}{7178000^3}} = 0.001rad/sec \quad (3.116)$$

The LQR resultant K matrix is calculated as

$$K = \begin{bmatrix} 1.0006 & 0 & 0 & 20.0350 & -0.4000 & 0 \\ 0 & 1 & 0 & -0.4000 & 20.2900 & 0 \\ 0 & 0 & 0.9980 & 0 & 0 & 20.0230 \end{bmatrix} \quad (3.117)$$

The 3-components responses of the relative position between the spacecrafts are shown in Figure 46. The corresponding thrust components are shown in Figure 47, and the cumulative fuel usage is shown in Figure 48. Figure 49 and Figure 50 show the 3-D rendezvous path in the target spacecraft (debris) reference frame. We can see that this proves to be an effective method of controlling the last stages of the orbital rendezvous as well as holding the in-plane separation between the IBS and the debris constant while minimizing the out-of-plane component errors. Further research has been done such as accounting for thruster nonlinearities [46] and H_∞ robust control [47]. The K matrixes obtained in both cases are similar to that obtained herein.

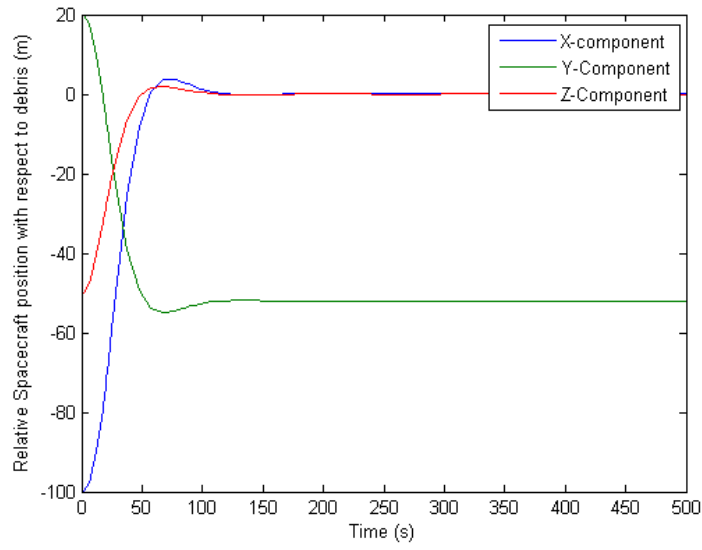


Figure 46: 3-component response for the state-feedback control system using the LQR gain matrix.

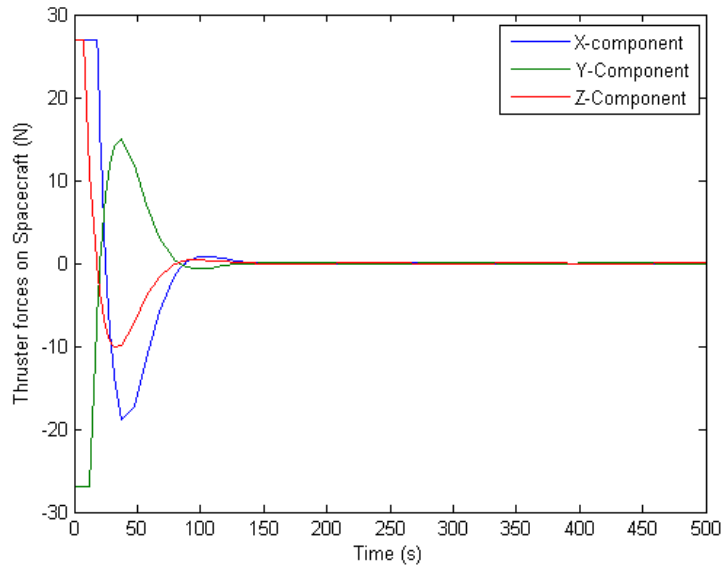


Figure 47: 3-component thruster force response for the state-feedback control system using the LQR gain matrix.

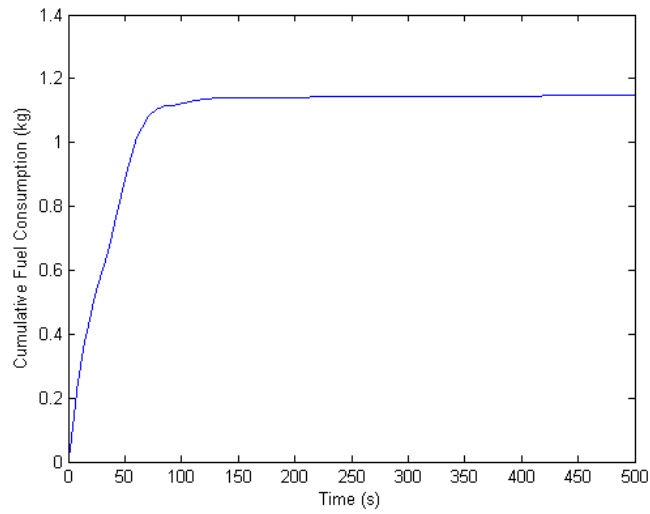


Figure 48: Cumulative fuel mass consumption for the controller using the LQR gain matrix.

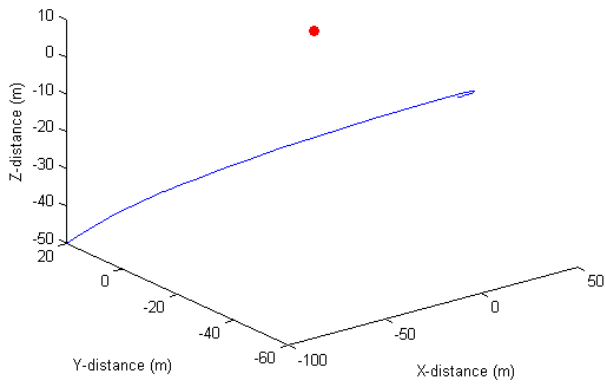


Figure 49: 3-D path of chaser satellite relative to target satellite (red) using the LQR gain matrix.

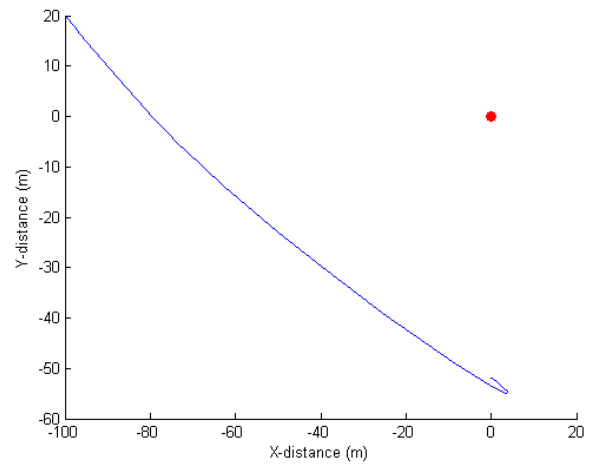


Figure 50: 2-D path of chaser satellite relative to target satellite (red) using the LQR gain matrix.

3.7.2 Control system simulation results using H_∞ gain matrix

The H_∞ response seems to be critically damped for the X and Z component, whereas the standard LQR method is slightly under damped and follows a second order response. The lack of overshoot slightly improves the problem in terms of time, as shown in Figure 51 and Figure 52. However, the fuel cost increases slightly due to the higher thrusts, shown in Figure 53. Figure 54 and Figure 55 show the relative position in the target (debris) reference frame. The K gain matrix using this method becomes [47]

$$K_{H_\infty} = \begin{bmatrix} -7.12 & 0 & 0.008 & -117.11 & 0 & 0.02 \\ 0 & -7.12 & 0 & 0 & -76.15 & 0 \\ 0.008 & 0 & -7.12 & -0.02 & 0 & -76.15 \end{bmatrix} \quad (3.118)$$

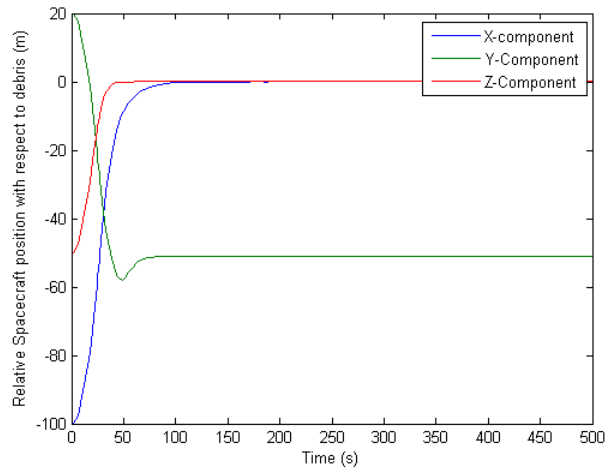


Figure 51: 3-component response for the state-feedback control system using the H_∞ gain matrix.

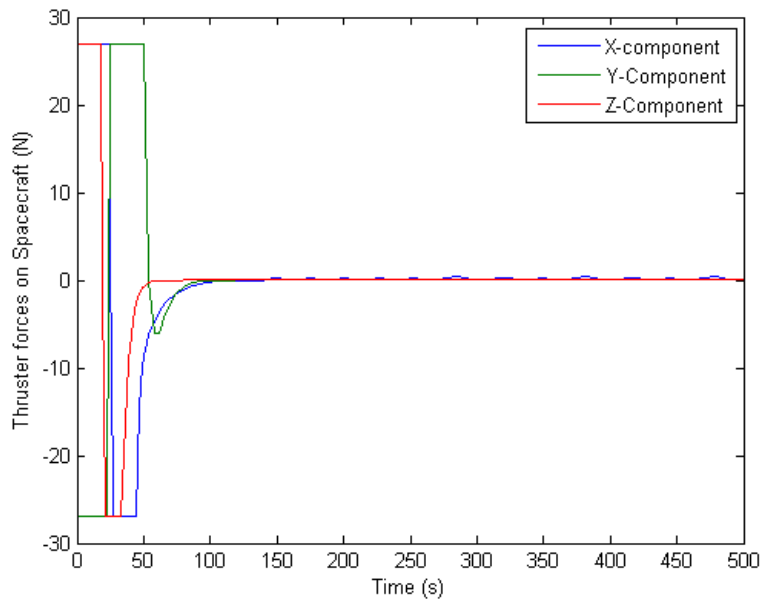


Figure 52: 3-component thruster force response for the state-feedback control system using the H_∞ gain matrix.

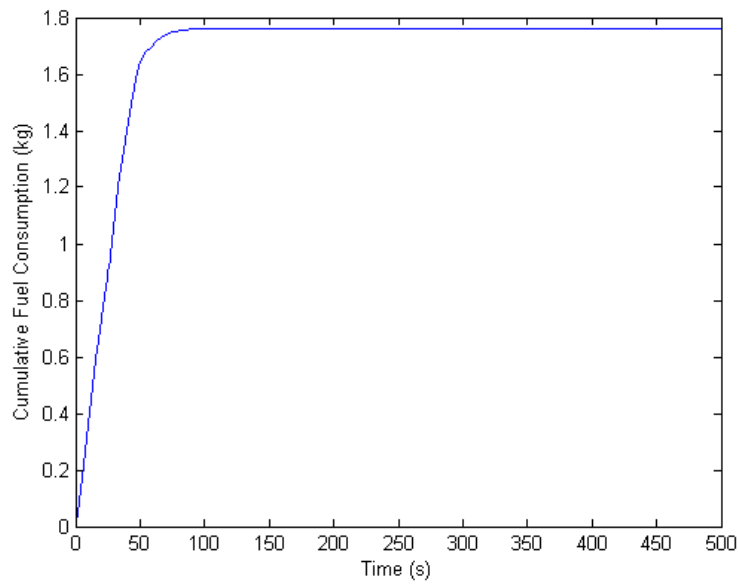


Figure 53: Cumulative fuel mass consumption for the controller using the H_∞ gain matrix.

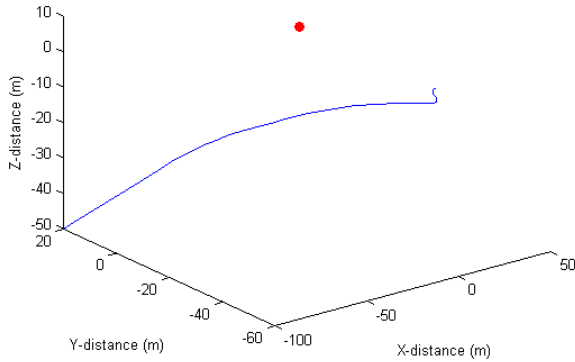


Figure 54: 3-D path of chaser satellite relative to target satellite (red) using the H_∞ gain matrix.

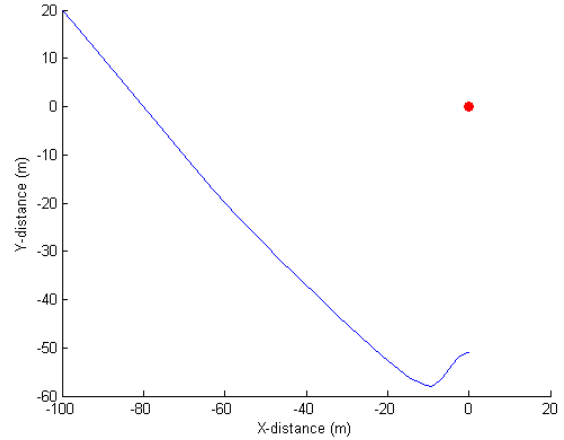


Figure 55: 2-D path of chaser satellite relative to target satellite (red) using the H_∞ gain matrix.

3.8 Attitude Control

In this section we take a look at the attitude control requirements for all the technologies. Attitude control is required in all four technology scenarios: accurate attitude control for the robotic arm in the modular de-orbit device technology, a nadir-pointing EDT so that it can operate properly, and pitch and yaw control to keep the pointing vector of the IBS aligned with the debris, and the combined EDT+IBS requirements for the EDT+IBS system.

The first analysis will be for the Euler angle control, since this does not involve the electromagnetic forces of the EDT. In this section we analyze the effectiveness of keeping the

satellite pointing towards the target using gravity gradient attitude control and additional momentum wheels. The torque on the spacecraft due to the gravity gradient force is given by Wie (2008) [43]

$$\vec{M} = -\mu \int \frac{\vec{\rho} \times \vec{R}_c}{|\vec{R}_c + \vec{\rho}|^3} dm \quad (3.119)$$

where \vec{M} is the gravity gradient torque, μ is the standard gravitational parameter of the earth, $\vec{\rho}$ is the density of the object at a given point, \vec{R}_c is the distance to the center of mass, and dm is the differential mass element. The un-controlled linearized equations of motion for roll, pitch, and yaw assuming a rigid body in circular orbit are given by

$$J_1 \ddot{\theta}_1 - n(J_1 - J_2 + J_3) \dot{\theta}_3 + 4n^2(J_2 - J_3) \theta_1 = 0 \quad (3.120)$$

$$J_2 \ddot{\theta}_2 + 3n^2(J_1 - J_3) \theta_2 = 0 \quad (3.121)$$

$$J_3 \ddot{\theta}_3 + n(J_1 - J_2 + J_3) \dot{\theta}_1 + n^2(J_2 - J_1) \theta_3 = 0 \quad (3.122)$$

where J_1 , J_2 , and J_3 the primary axis moments of inertia and θ_1 , θ_2 , and θ_3 are the Euler angles of the spacecraft. Equations 3.120-3.122 turn into the following controlled equations of motion [43]

$$J_1 \ddot{\theta}_1 - n(J_1 - J_2 + J_3) \dot{\theta}_3 + 4n^2(J_2 - J_3) \theta_1 = -u_1 + d_1 \quad (3.123)$$

$$J_2 \ddot{\theta}_2 + 3n^2(J_1 - J_3) \theta_2 = -u_2 + d_2 \quad (3.124)$$

$$J_3 \ddot{\theta}_3 + n(J_1 - J_2 + J_3) \dot{\theta}_1 + n^2(J_2 - J_1) \theta_3 = -u_3 + d_3 \quad (3.125)$$

$$\dot{h}_1 - nh_3 = u_1 \quad (3.126)$$

$$\dot{h}_2 = u_2 \quad (3.127)$$

$$\dot{h}_3 + nh_1 = u_3 \quad (3.128)$$

where h_1 , h_2 , and h_3 represent the angular momentum of the momentum control wheels and d_1 , d_2 , and d_3 are the disturbance torques. Assuming a cylindrical configuration for the satellite, the moments of inertia for the system will be similar to those given by the matrix J . These values are solely for simulation and validation purposes and the simulation should be re-run once an accurate J matrix has been evaluated from the detailed structural design. The momentum wheel inertia matrices are assumed to be given by JW ,

$$J = \begin{bmatrix} 1000 & 0 & 0 \\ 0 & 1000 & 0 \\ 0 & 0 & 100 \end{bmatrix} \quad (3.129)$$

$$JW = \begin{bmatrix} 1E-7 & 0 & 0 \\ 0 & 1E-7 & 0 \\ 0 & 0 & 1E-7 \end{bmatrix} \quad (3.130)$$

For the IBS technology, roll control is irrelevant as the beam is assumed axis-symmetric. The common choice for small spacecraft attitude control is momentum wheels, which are spun up or down to control the angular momentum of the spacecraft.

In the case of the combined IBS+EDT design, when the tether is extended to its full length of 5km and the momentum wheels are placed in the main satellite body, the situation becomes more complex since the momentum wheels are not acting on the principle axis of the satellite. Therefore, for simplicity and to avoid complex torsion and libration of the tether, we suggest that the tether is retracted during the final approach so that the momentum wheels are aligned with the principle axis of the satellite.

Left uncontrolled, given certain stability criterion outlined in Wie (2008) [43], the satellite will follow a pendulum motion along the yaw axis with an amplitude equal to its initial error from the nadir direction due to the gravity gradient torque. The active controls hope to reduce this pendulum error to a smaller magnitude, at the same time controlling the other errors due to disturbance torques.

The pointing accuracy is very important to ensure that the ion beam momentum transfer remains efficient and that the grappling of the modular de-orbit device is effective. We developed a SIMULINK/MATLAB code to simulate the attitude dynamics of a standard spacecraft subject to gravity gradient and control torques. To test the simulation, an unstable moment of inertia configuration was tested and is shown in Figure 56. After showing that the simulation follows the expected conditions, the stable uncontrolled gravity gradient torque simulation is shown in Figure 57 and the effect of the active control is shown in Figure 58. Figure 59 shows the angular momentum of the three wheels, and Figure 60 shows the corresponding RPM.

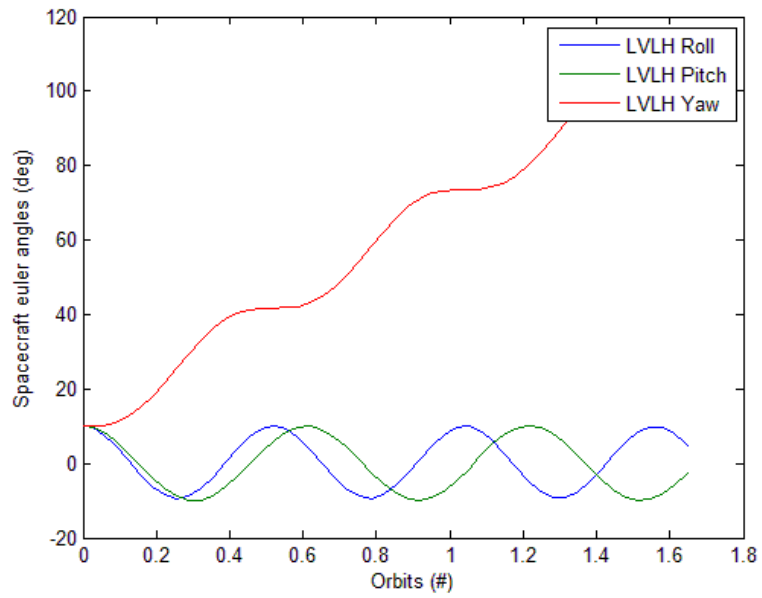


Figure 56: Unstable gravity gradient configuration.

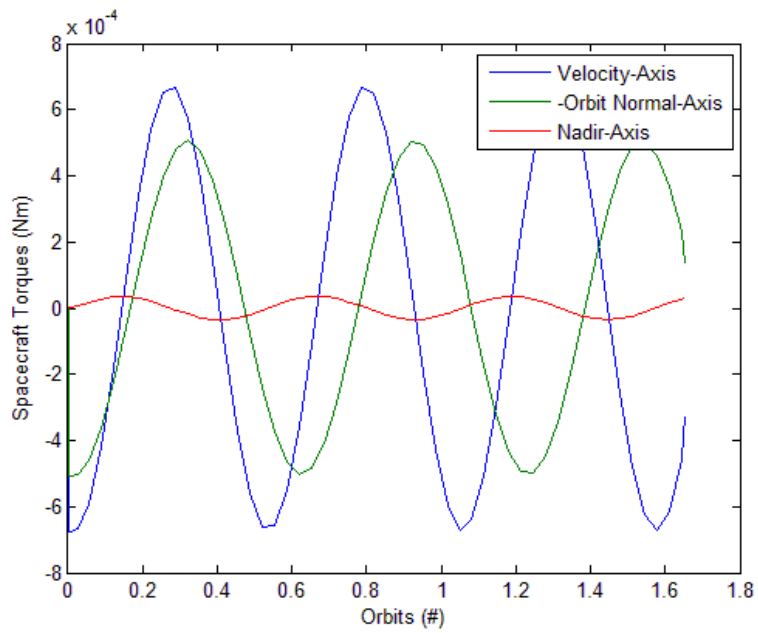


Figure 57: Gravity Gradient Torques.

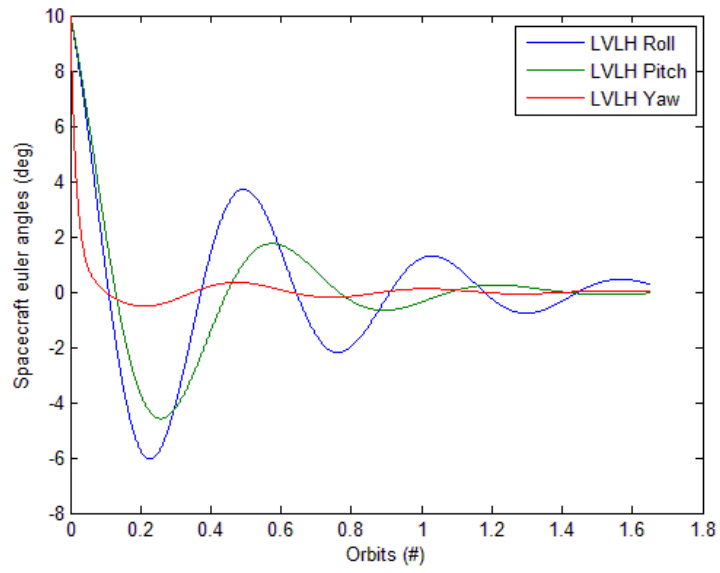


Figure 58: SC Euler angles with active attitude control.

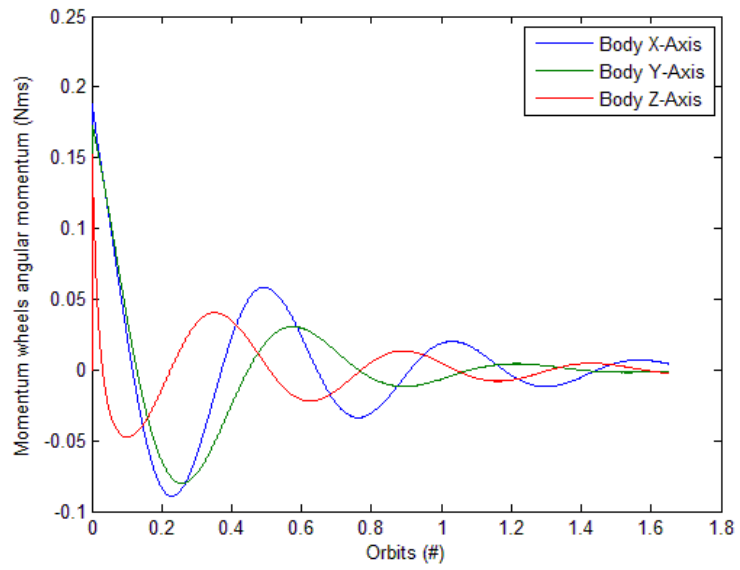


Figure 59: SC Momentum wheel angular momentum.

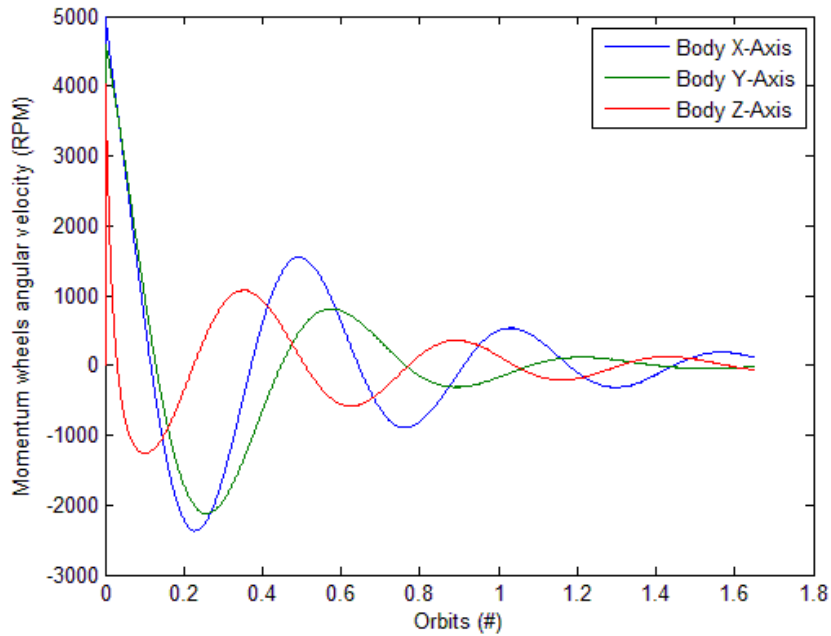


Figure 60: SC Momentum wheel RPM.

This simulation serves to show that active attitude control of the satellite is possible to ensure accurate pointing vector, be it nadir-pointing or debris-pointing, employing momentum wheels that fall within the operational limits of today's technology.

The attitude control during descent using the EDT is slightly more complicated. Clearly, since it is of key importance during this phase, the tether is extended here. However, constant current EDT systems have a tendency to build up energy and greatly alter the libration angle of the tether, thus decreasing the efficiency of the design. However, Corsi and Iess (2001) [48] have hypothesized and simulated a control scheme based on the Lyapunov energy method and an on-off switch control approach. Simply put,

when the energy of the system increases beyond a defined threshold, the system shuts off and allows for energy to dissipate, at which point it turns back on. Using this method, Corsi and Iess (2001) [48] was able to successfully contain the libration angle within a reasonable limit, as shown in Figure 61 and Figure 62.

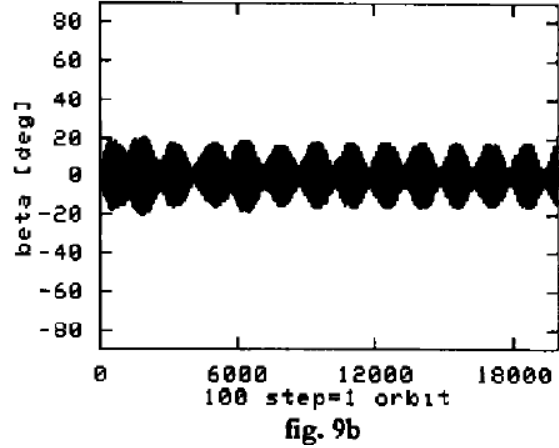
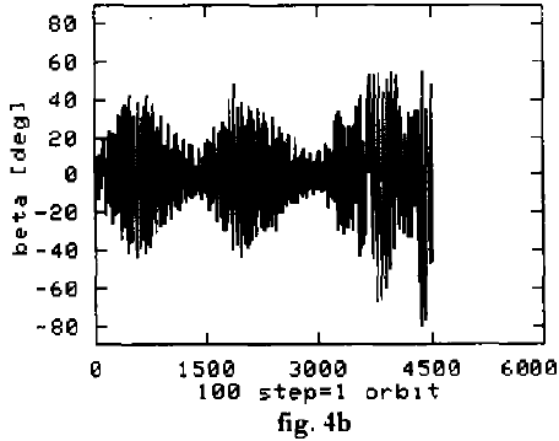
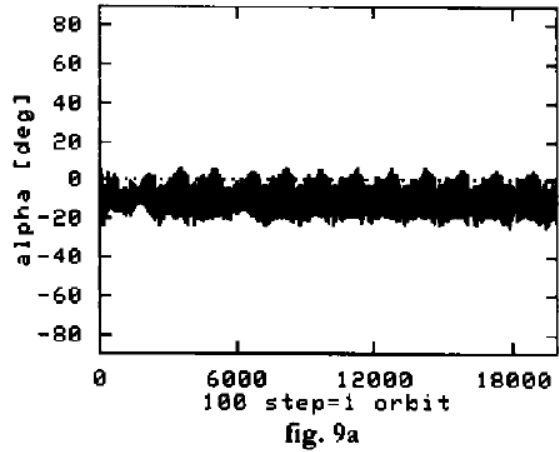
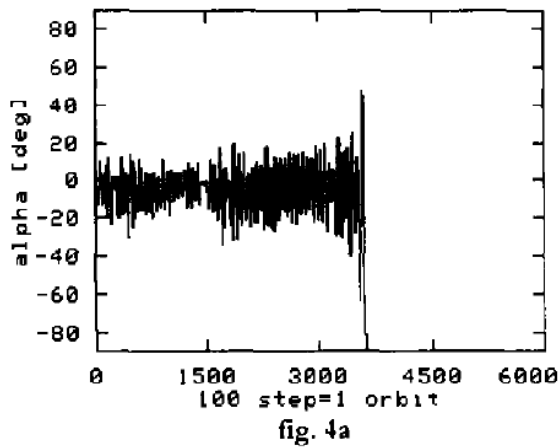


Figure 61: Libration angles without control [48].

Figure 62: Libration angles with active on-off switch control [48].

3.9 Active debris removal technology tradeoff simulation results

Now that a large portion of the technological aspects of all the technologies have been reviewed, we apply these theories into a simulation in order to test the technologies against each other in terms of fuel cost and time.

The equations of motion in equations 3.5-3.10 were used and integrated using a Runge-Kutta-4 integration scheme. Initial simulations were run to determine the individual descent rate and fuel burn of different technologies with respect to debris size and altitude. Thereafter, these technologies were simulated to perform a waypoint list multiple de-orbit mission using a combination of different orbit-rising and de-orbit technologies.

3.9.1 Descent Rate and Fuel Burn for varying debris size and altitude

Figure 63 and Figure 64 show the propellant mass and de-orbit time required to de-orbit orbital debris from varying altitudes and masses using traditional 'impulsive' thrusters.

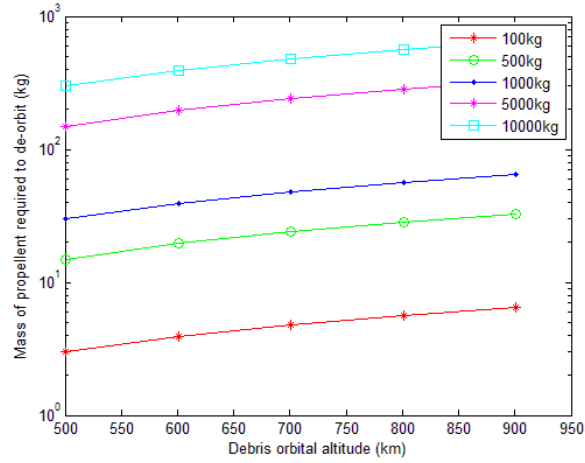


Figure 63: Propellant mass required to de-orbit orbital debris of different masses from a series of orbital altitudes to a perigee of 200km using instantaneous thrusters

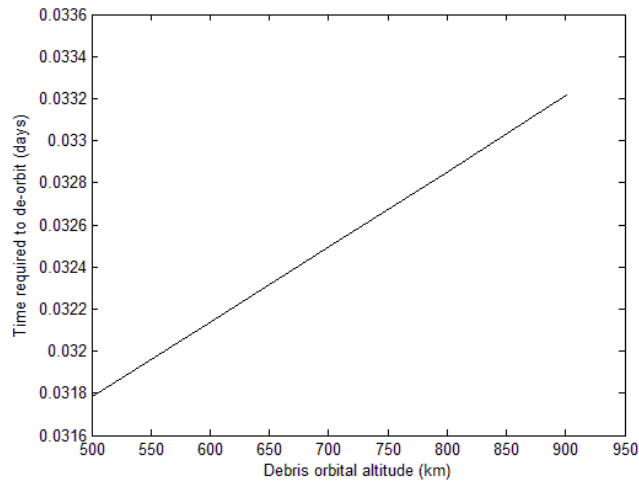


Figure 64: Time required de-orbiting debris from varying altitudes. This plot is independent of debris mass because the maneuvers are 'impulsive' and therefore share an instantaneous common transfer orbit to 200km perigee.

Figure 65 and Figure 66 show the propellant mass and time required to de-orbit debris of varying mass at varying altitudes to 200km perigee using the Ion Beam shepherd method assuming a constant thrust of 200mn.

Figure 65 has some unique non-linear characteristics. This is most likely due to the effect of adding the ratio of the IBS mass to the debris mass into the fuel cost calculation. This is an additional factor that is superimposed on the simple trend of debris mass vs. altitude. One can see that the curves seem to 'flatten out' as the debris mass increases and this term becomes less significant.

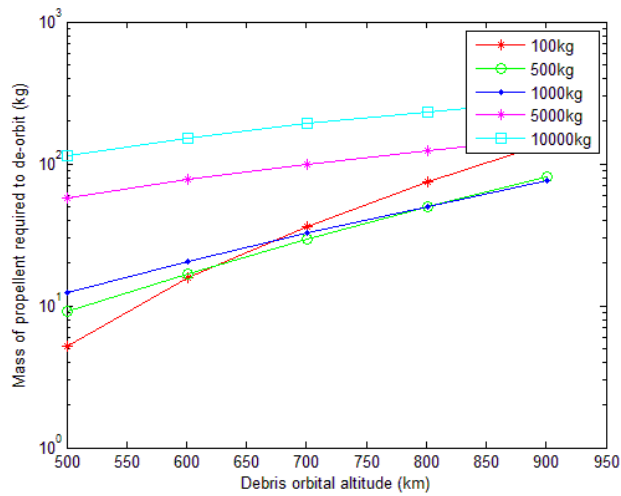


Figure 65: Propellant mass required to de-orbit orbital debris of different masses from a series of orbital altitudes to a perigee of 200km using an Ion Beam with constant thrust of 200mn.

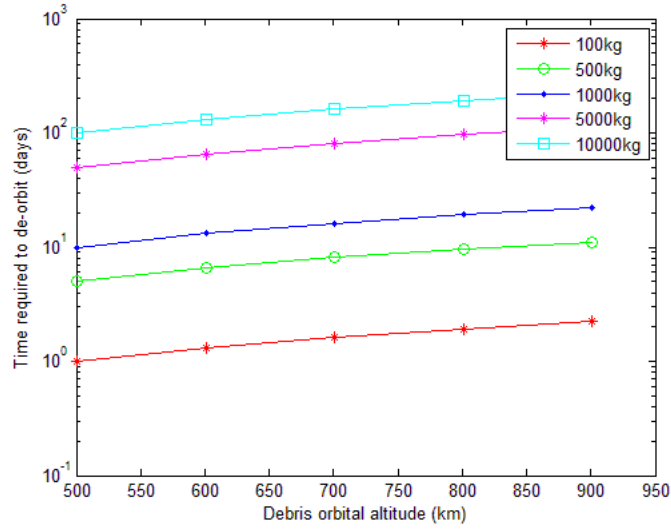


Figure 66: Time required de-orbiting orbital debris of different masses from a series of orbital altitudes to a perigee of 200km using an Ion Beam with constant thrust of 200mn.

Figure 67 shows the time required to de-orbit debris of varying mass at varying altitudes to 200km perigee using the Electrodynamic tether method assuming a dipole magnetic field. Since the force generated by the EDT is in multiple directions, some of the orbital parameters are coupled depending on which control law is used. For the case of DC current for semi-major axis control, the inclination is also affected. With a decrease in altitude, the inclination seems to 'drift' towards a polar orbit. Unfortunately as the satellite approaches 90 degrees inclination, the z-component of the dipole model of the earth's magnetic field reverses direction. If the current is left un-modulated, then the force on the EDT will reverse and it will rise in altitude and continue to drift in its current direction. If the EDT current is reversed when the z-component is reversed, then the EDT

will once again drift towards this reversal point as it attempts to descend in altitude, resulting in oscillation around the z-component reversal inclination and altitude. Given that the objects of interest were in a sun-synchronous orbit, they were brought to an inclination of 105 degrees prior to descent. This allowed enough inclination and altitude change to avoid the pole ward drift problem. This pre-descent maneuver does not cost any fuel; however, it does add time to the mission if the EDT is used for de orbit. The fuel cost of the total de orbit is zero for all combinations of mass and altitude.

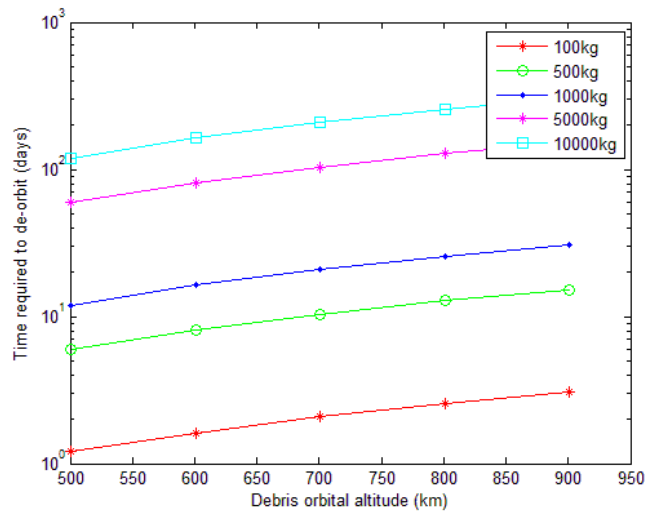


Figure 67: Time required to de-orbit orbital debris of different masses from a series of orbital altitudes to a perigee of 200km using an Electrodynamics Tether of length 5km and max current of 5 amps.

Figure 68 and Figure 69 compare the three technologies for a common altitude of 1000km at varying debris mass in terms of propellant mass and time required to de-orbit to a perigee of 200km.

Figure 68 shows the importance of including the spacecraft mass to debris mass ratio in the fuel cost calculations. The simulation used a spacecraft mass of 2000kg so this effect is heavily emphasized. However, even with a small 200kg variant, this effect would add more than 10% fuel cost given the debris objects under investigation weigh a maximum of 2000kg.

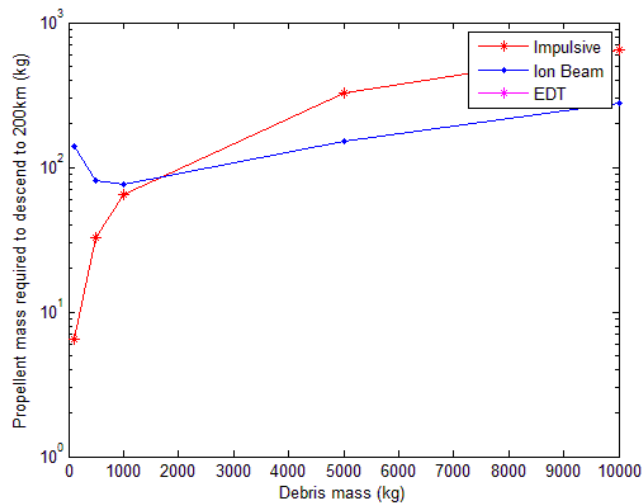


Figure 68: Propellant mass required to de-orbit debris of varying mass from an orbit of 1000km to a perigee of 200km using the three technologies.

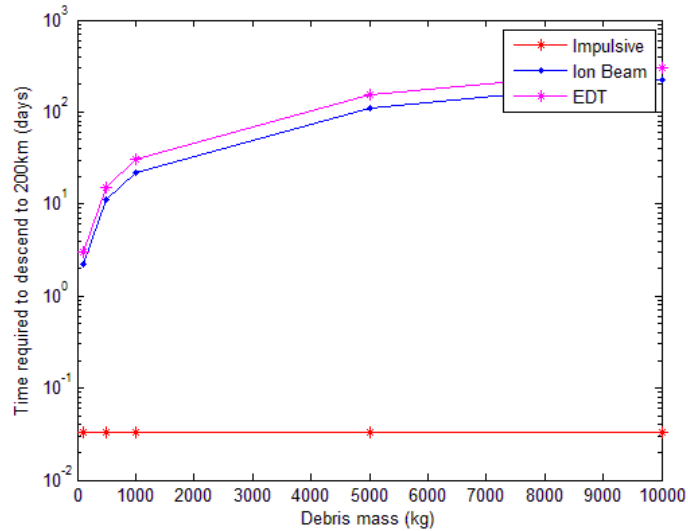


Figure 69: Time required to de-orbit debris of varying mass from an orbit of 1000km to a perigee of 200km using the three technologies.

The trend shown in Figure 68 makes sense due to the fact that the acceleration on a small mass satellite is much greater than the host spacecraft and the secondary engine needs to compensate a large amount to match the accelerations in order to keep a relatively constant orbital separation assuming that the debris mass $>$ spacecraft mass.

It is clear that the EDT method for debris removal is the most fuel effective method as it requires no fuel to change orbital parameters. However, this method is not automatically the best option. The ion beam shepherd requires almost as much time as the thruster method to de orbit debris, assuming 200mn thrust. However, when comparing its fuel costs to that of the impulsive maneuvers, one can see that it is far superior

assuming that the spacecraft mass is not many times greater than that of the debris. This is a fair assumption given that the debris objects in question are very large weighing up to 2000kg. Comparing the Ion Beam to the EDT, one can claim that the advantage of contactless debris removal outweighs the small cost of propellant and increase in overall mission time as it greatly reduces mission risk. Mating to a piece of space debris can be very risky due to unknown attitude dynamics of the debris. Attempts of docking could result in a variety of effects including explosions, breaking of the docking device, and the generation of more debris.

3.9.2 Multiple debris object de-orbit mission analysis

Lastly, to simulate a real life mission using these technologies, Castronuovo (2011) [25] outlines a waypoint list of large debris objects based on the following justifications:

- Large commercial interest in sun-synchronous orbit debris
- >10cm diameter objects pose the most risk to satellites in terms of destruction
- ordered by increasing values of RAAN to minimize fuel costs

The first six large debris objects outlined in this list are shown in Table 11 below. The reason the list was limited to the first six objects is due to the fact that after the sixth object, the satellite proposed by Castronuovo (2011) [25] has no more fuel left.

Therefore, in order to simply compare the orbital maneuvering technologies with each other without the need of secondary refueling stations, the simulation was ended here since further waypoints would simply multiply the cost of the technologies.

Table 11: Debris Waypoint List.

Name	Apogee (km)	Perigee (km)	Inclinatio n (Deg)	RAAN (deg)	Mass (kg)	Disposal Orbit Perigee (km)
IRS-P2 R/B	877	807	98.74	1.3	912	238
SL-6 R/B	807	790	98.58	7.6	892	285
THOR BURNER 2 R/B	848	781	98.98	11.8	65	320
ARIANE 40+R/B	774	758	98.49	13.2	1764	295
ARIANE 40 R/B	799	777	98.62	13.3	1764	295
ARIANE 40 R/B	777	743	98.64	22.4	1764	294

The parameters and algorithm of the simulation are outlined below

- Four permutations of removal technologies
 - Traditional Thrusters as for rendezvous and de-orbit shown in Castronuovo (2011) [25]
 - Traditional Thrusters for rendezvous and Ion Beam for de-orbit as shown in Bombardelli (2011) [19]

- Electrodynamic Tether (EDT) for rendezvous and de-orbit
 - Electrodynamic Tether (EDT) for rendezvous and Ion Beam for de-orbit
- Traditional Thrusters are modeled as impulsive maneuvers
 - ISP of 288 for rendezvous
 - ISP of 300 for de-orbit
 - All impulsive maneuvers initiated at apogee
- EDT rendezvous is successful when all 6 classical orbital parameters have an absolute error of less than
 - 100m for semi-major axis
 - 0.0001 for eccentricity
 - 0.001 degrees for inclination
 - 0.001 degrees for RAAN
- De-orbit is successful when the perigee of the debris' orbit is lowered to the disposal orbit shown in Castronuovo (2011) [25]
- Ion Beam Parameters
 - Constant tangential thrust of 200mN
 - 5kg/kW power supply rating
 - variable exhaust velocity
 - Efficiency of 70%
- EDT Parameters
 - 5km Length
 - Max current of 5amps
- Phase angle is ignored in order to be consistent with Castronuovo (2011) [25]
- Impulsive maneuvers are done at apogee and perigee for fuel optimization
- 2000kg initial spacecraft mass for all perturbations

- Time step of 100 seconds

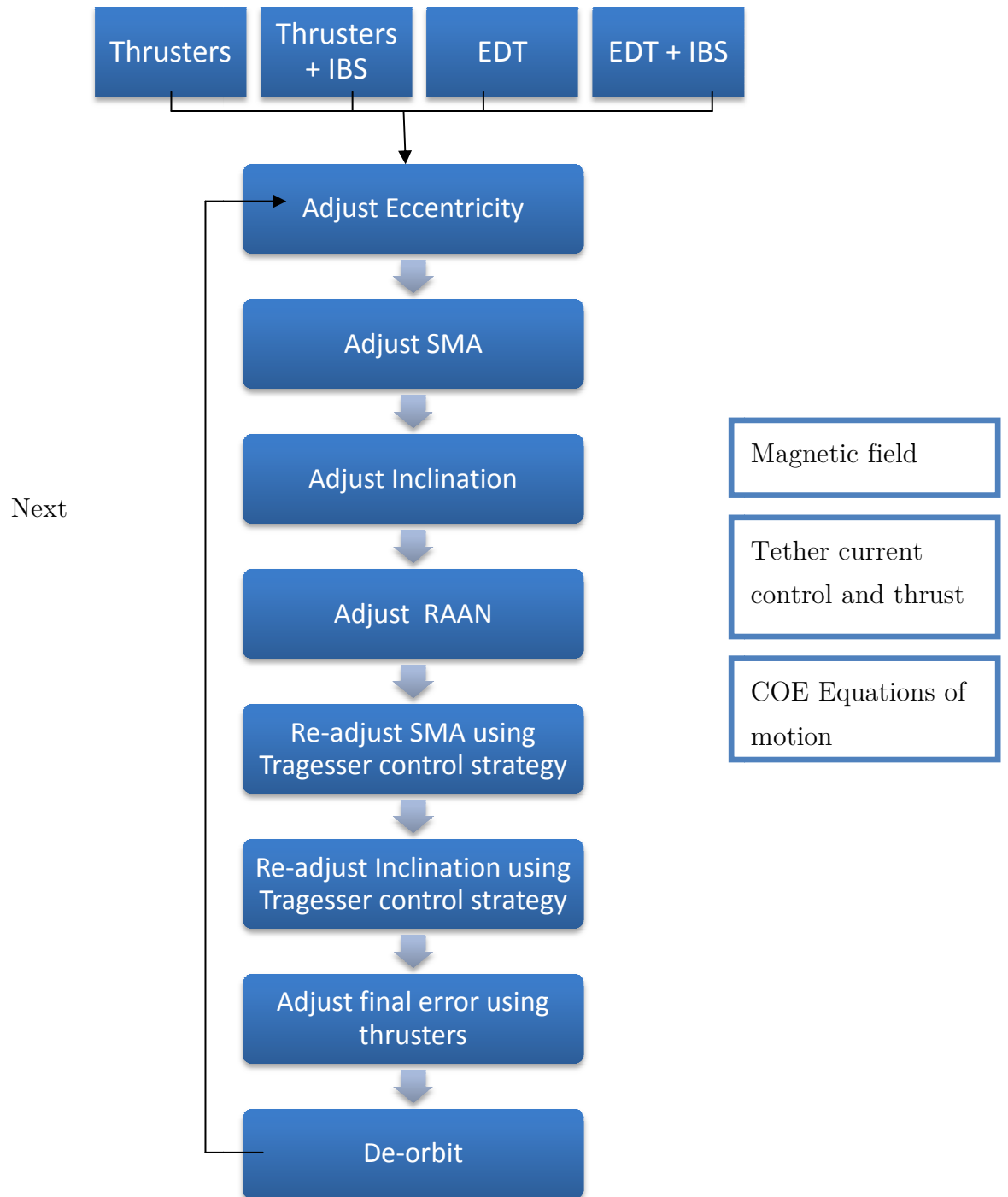


Figure 70: Rendezvous mission algorithm.

Bringing all of the knowledge gained from conducting this thesis together, and simulating the respective technology combinations produces some interesting results, starting with Figure 71. Figure 71 shows the overall spacecraft mass varying over time and waypoint number. From a first look, the IBS system seems to perform worse than the traditional thruster design since it requires more fuel to de-orbit the debris. This effect is due to the high cost of fuel when changing orbital inclination and RAAN. However, by using the EDT for the majority of the orbital rendezvous maneuvers, traditional thrusters for the fine-tuning of orbital elements, and the IBS for the actual de-orbit, the fuel cost is greatly reduced to consuming only 13.4% of its initial 2000kg mass after 6 waypoints.

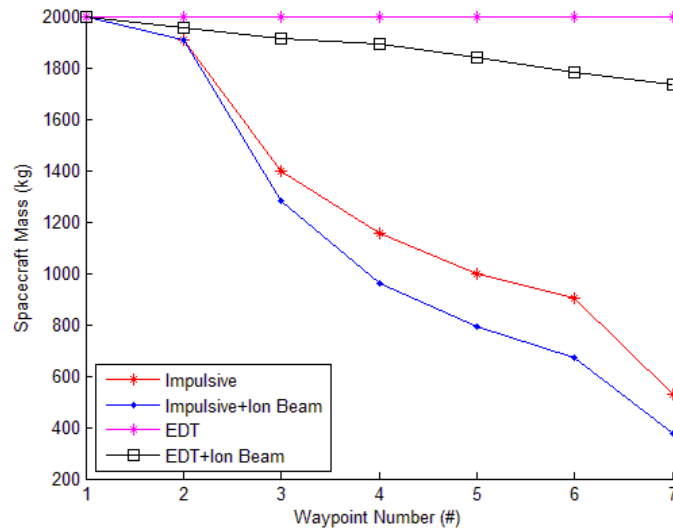


Figure 71: Spacecraft mass vs. waypoint number comparing the different technology combinations.

The EDT seems to outperform all of the other designs in terms of fuel cost. However, one must remember from the earlier discussion on the EDT that the de-orbit phase using the EDT is problematic due to pole ward drifts at high inclination. This drift can be corrected two ways: using an inclination buffer zone or using the Tragesser method to control the inclination during descent. However, both of these methods add considerable time to the overall mission. Moreover, in order for the EDT to be used for de-orbit it would require physically grappling the debris which adds risk to the overall mission due to unknown factors such as debris attitude.

One can note that the fuel used by the EDT is non-zero. This is due to the fact that an exact orbit match could not be performed due to the cyclical co-dependency of the orbital elements when using an EDT. The implementation of the control scheme has greatly reduced this value from earlier simulations which used only the single current control laws separately. The error that remains is corrected using traditional thrusters which accounts for the fuel used in the EDT method. Examples of the final state errors are shown in Table 12 for the EDT+IBS system.

Table 12: Sample state vector error resulting from EDT rendezvous and associated propellant mass required.

Waypoint	S.M.A (m)	Eccentricity	Inclination (deg)	RAAN (deg)	Total adjustment (km/s)	Propellant Mass (kg)
1	97.16	0.00007	0.00082	0.00098	0.00042	0.29
2	96.50	0.00013	0.00093	0.00090	0.00062	0.44
3	96.69	0.00008	0.00086	0.00094	0.00046	0.30
4	97.28	0.00013	0.00080	0.00095	0.00065	0.40
5	93.75	0.00004	0.00093	0.00093	0.00034	0.21
6	94.78	0.00001	0.00095	0.00094	0.00022	0.13

Other than having the advantage of contactless debris removal, the EDT+IBS system does not encounter the problems of co-dependent orbital elements during de-orbit, such as pole ward drift during descent. This reduces the overall mission time by a significant amount. For example, Figure 72 shows the perigee altitude and inclination evolution of the satellite as it progresses through the waypoints using the EDT+Ion Beam System. Figure 73 acts as a key to distinguish between the different segments of the rendezvous. One can observe the co-dependent effects of these two elements during the orbit raising section since the de orbit is performed via ion thrusters not the EDT.

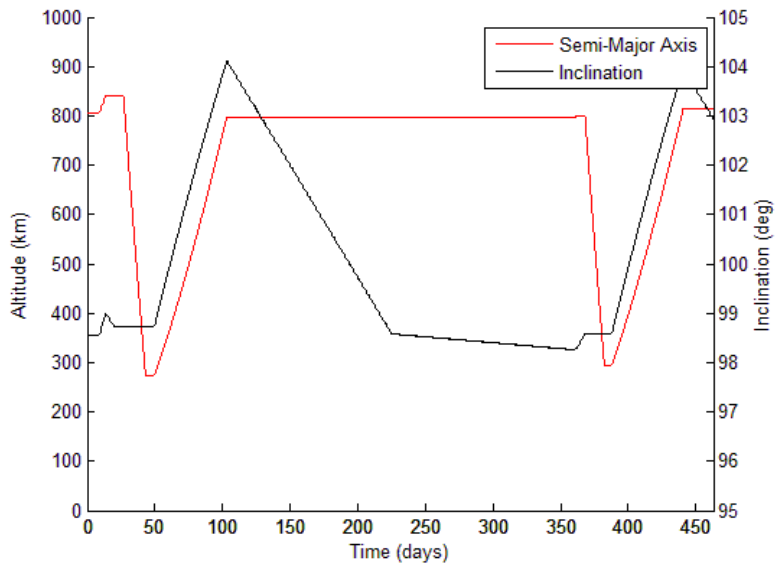


Figure 72: Perigee and inclination evolution over time for the EDT+Ion Beam System.

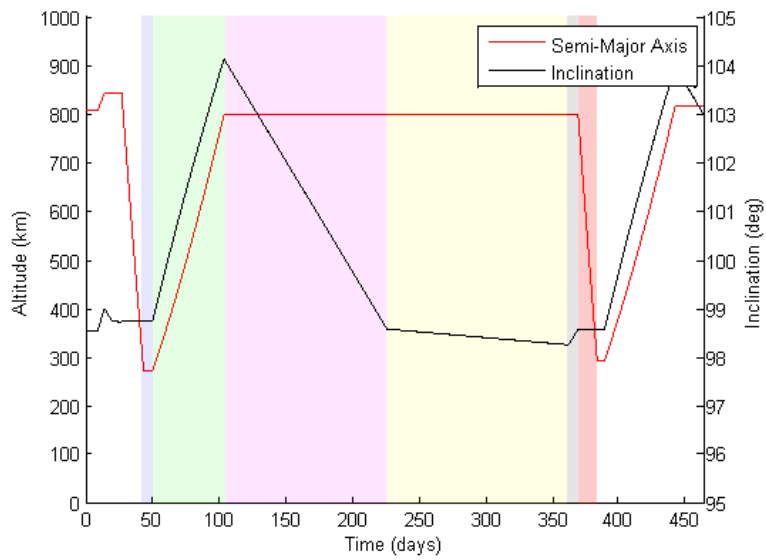


Figure 73: A breakdown of the orbital maneuvers.

Table 13: Color codes for the breakdown of the orbital maneuvers shown in Figure 73.

Background Color	Maneuver
Blue	Match Eccentricity
Green	Match Semi-Major Axis
Magenta	Match Inclination
Yellow	Match RAAN
Grey	Control SMA+Inclination
Red	De-orbit

Figure 74 shows the evolution of the spacecraft mass with respect to time. Knowing that the spacecraft only changes mass during the de orbit maneuver since the other maneuvers are done using the EDT, one can conclude that the majority of the time contribution is due to the orbital rendezvous. This time is very large due to the small forces produced by the EDT and the large mass of the host spacecraft in this simulation (2000kg). Since we cannot change the magnitude of the force generated by the EDT due to constraints on the maximum current in the tether, the only variable to change is the spacecraft mass. In order to reduce the time needed to de orbit these debris objects, a smaller 200kg variant of the IBS+EDT design is investigated in section 3.10.

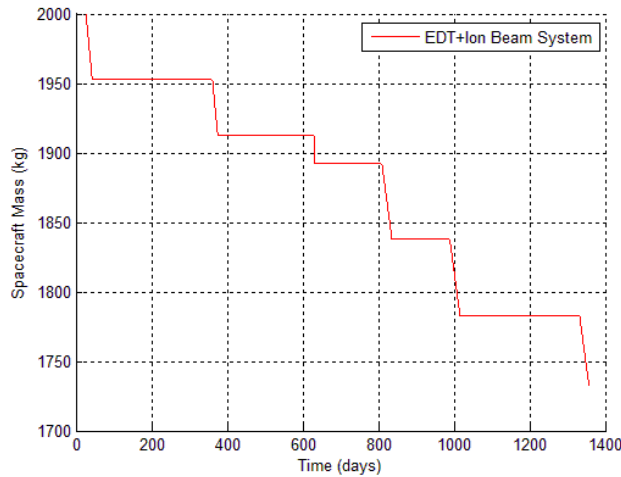


Figure 74: Spacecraft mass vs. time for EDT+IBS system assuming $m_0=2000\text{kg}$.

3.10 Proposed Small Satellite using Ion Beam and Electrodynamic Tether technologies

In order to fully explore the mission capabilities of this EDT+Ion Beam shepherd design, a small satellite of 200kg total mass is proposed in hopes of reducing the time required to de orbit the debris, making this technology even more useful. The waypoint is expanded to include debris objects until the proposed satellite runs out of fuel. Since the fuel cost greatly depends on the ratio between the debris mass and the satellite mass, reducing the satellite mass should impact the overall mission fuel cost as well. The reduction in mission time can be seen in Figure 75 Figure 76 compared to Figure 74. One can see that the overall mission fuel cost is slightly reduced from the 2000kg variant due to the smaller spacecraft to debris mass ratio. However, more importantly, the time

required for the de orbit is significantly reduced. We can see in Figure 76 that the mission time is no longer dominated by the orbital rendezvous, rather by the de orbit. The 200kg satellite completes the same mission as the 2000kg satellite with an 85% reduction in mission time.

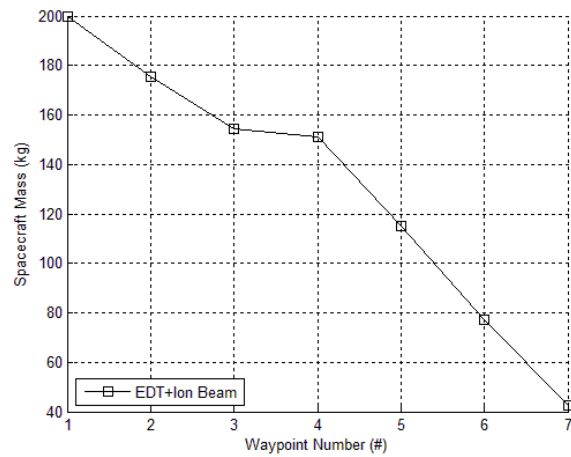


Figure 75: Spacecraft mass vs. waypoint for EDT+IBS system assuming $m_0=200\text{kg}$.

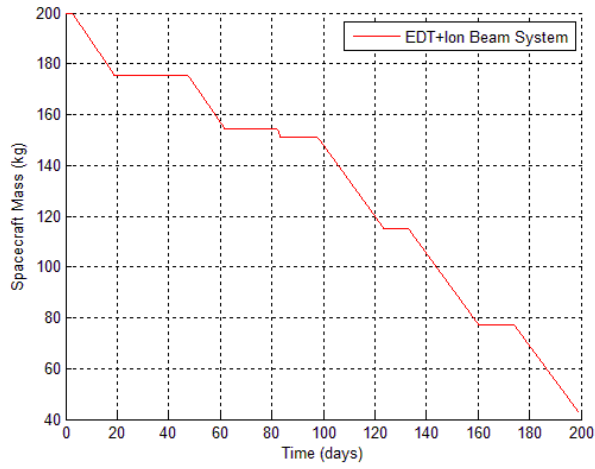


Figure 76: Spacecraft mass vs. time for EDT+IBS system assuming $m_0=200\text{kg}$.

Another interesting point of discussion is the effect of the tether length on the time required to complete the mission. The same 6-waypoint mission was simulated for 5km, 10km, and 15km tethers and the results are shown in Figure 77.

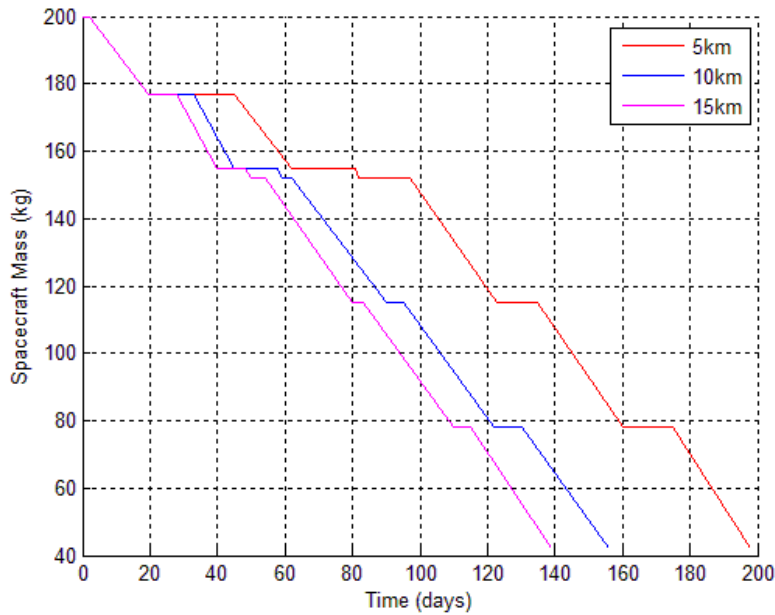


Figure 77: Spacecraft mass vs. time for EDT+IBS system assuming $m_0=200\text{kg}$ for 5km, 10km, and 15km tether lengths.

One can see that the total time for de-orbiting the six debris objects of interest decreases with increasing tether length with a decreasing marginal rate of return. However, the mass consumed by the system remains the same. This is expected as the EDT system does not consume fuel however produces more force per unit length. The decrease in de orbit time can be identified by the decrease in length of the horizontal portions of the graph. The satellite is of course not solely made of fuel. Therefore to get a more accurate picture of the mission capabilities of a 200kg total mass satellite, a systems analysis of the possible configurations of an EDT+IBS satellite system need to be analyzed. Knowing the overall dry mass and using Figure 75, Figure 76 and Figure 77,

one can determine the mission capabilities of a small 200kg class satellite both in terms of debris objects removed and in time taken. The launch cost of a 200kg satellite at the current \$10,000 per kg would be roughly 2 million dollars with additional development cost. If approximately half of the satellite consists of subsystem masses, then the satellite would be able to remove about 5 objects during its mission, which corresponds to a metric of \$400,000 per object. Therefore, in order to remove all of the 35 objects in the list presented in Castronuovo (2011) [25], this would require 7 EDT+IBS systems of the 200kg variant with a total cost of 14 million dollars with additional development cost. This falls far cheaper than the single 2000kg spacecraft using traditional thrusters and orbital refueling station alternative. The risk factor of the EDT+IBS system is much lower due to the contactless momentum transfer between satellite and debris due to the ion beam. However, if multiple of these satellites are to operate at the same time, proper coordination is an absolute requirement as several 5km-10km tethers all operating in roughly the same orbits gives rise to possible collisions between tethers.

Chapter 4

Summary

Orbital debris is a growing problem in the space environment as it poses a direct threat to current and future space missions. Many solutions have been proposed, but few ideas have come to fruition. The problem of space debris is a self evolving environment of hazardous material which will continually grow if untreated, eventually making the space surrounding our planet un-usable for satellites and space missions. This paper has outlined some of the main candidates for small and large debris removal. The large active debris removal technologies (EDT, IBS, Thrusters) were analyzed, both individually as well as combined permutations of the three methods. The Ion Beam Shepherd (IBS) and the electrodynamic tether (EDT) were investigated in detail.

The largest advantage of an EDT system is the low fuel cost of orbital maneuvers due to the fact that the EDT works off the principle of electromagnetism to generate thrust and hence does not consume any traditional chemical fuel. On the other hand, it does require the use of a power supply and other components, which can add to the complexity, cost, and weight of the satellite. Furthermore, the technology's weak point is that it is very inefficient while operating in sun-synchronous orbits due to the vector geometry of the tether with respect to the magnetic field of the earth. This is an issue as a

large portion of debris fall within this region and the sun-synchronous orbit is a highly desirable orbit. Another drawback is that the standard current laws for the EDT result in undesired shifts in orbital elements. At high inclination orbits, these shifts can make the satellite drift pole-wards at which point the tether is unable to function. A correction buffer zone of 105 degrees inclination has been shown to provide enough room to avoid this error, but at the cost of a large increase in operational lifetime per debris object. Therefore, the issue of co-dependent orbital elements is addressed using a current control law to reduce the error during orbital rendezvous by changing the semi-major axis and the inclination independent of the other orbital elements. This is achieved by modulating the current as a superposition of several wave forms which allows you to keep all of the orbital elements in check as you modify the desired element. However, the total time to achieve the desired state is increased. Lastly, an EDT current control strategy was outlined using both the standard control currents and the super positioned currents, which leads to a very small error in the final orbital elements while reducing the overall rendezvous time.

The Ion Beam Shepherd's strongpoint is the fact that it can provide contactless debris removal through the use of an ion beam to transfer momentum to a debris object in order to lower its orbit to a point of natural decay due to drag. In order for efficient momentum transfer, the IBS has to remain in leader-follower formation at a relatively

close distance during the entire de-orbit phase in order to avoid efficiency loss due to beam divergence. Furthermore, the error in the pointing vector of the IBS must be minimized in order to reduce risk of induced attitude changes and debris spin-up, which could result in the production of secondary fragments. These secondary fragments would both increase the debris population in the given orbit as well as endanger the IBS itself.

In order to determine the maximum efficient operating distance of the IBS, plume divergence simulations have been performed using self-similar models and the results show that the electrostatic beam divergence becomes significant at a distance of about 100m using the parameters defined. Therefore, if the operating range of the IBS system is maintained below 100m, then the momentum transfer efficiency only depends on appropriate pointing of the thrusters. Both the leader-follower position and the pointing vector have been shown to be controllable using standard state-feedback control systems to maintain minimal error. The IBS's main drawback is the fuel usage in performing a large amount of orbital rendezvous, particularly large changes in the right ascension of the ascending node. Further problems exist such as charge exchange collisions resulting in spacecraft charging, back scattering from the ion beam impact, and possible particle beam instabilities which need to be investigated further.

It seems that these two technologies can be combined in order to eliminate the weakness of the other, and simulations have shown that a combination of these two technologies greatly improves the effectiveness of both concepts for debris removal. This is achieved by utilizing the EDT for orbital rendezvous, which eliminates the large fuel cost of the IBS, and the de-orbit capabilities of the IBS, which has no co-dependent orbital elements, to decrease the overall de-orbit time. Simulations show that this combined technology far outperforms the other permutations investigated, consuming only 13.4% of its original 2000kg mass after 6 waypoints whereas the other permutations consumed almost all of their fuel. The EDT as a stand-alone technology was the only one to outperform the hybrid design in terms of fuel cost. However, it falls short in terms of overall mission time. Therefore, the hybrid design takes the best of both worlds and greatly reducing the mission time compared to just the EDT, at the cost of only minimal fuel usage increase. The main risk factor involved with this design is the survivability of the tether due to debris impacts and the unknown beam-debris interactions outlined previously. Since the tether is very long, up to 10km, it sweeps out a large section of space making it vulnerable to both debris impacts and impacts with other tethers. This risk can be reduced by using creative tether designs such as double-strand tethers, which provide a backup strand in case of an impact, and through proper planning and communication between tether implementing satellites.

Since the EDT and IBS must move not only the debris, but also the satellite itself, the overall mission time is largely dependent on the spacecraft mass due to the small forces produced by the EDT during rendezvous. Therefore, a small satellite variant of this hybrid technology was investigated to see if it was necessary to carry so much fuel mass. Simulations show that a 200kg variant, as opposed to the initial 2000kg design, decreases the overall mission time by about 85%. Simulations show that a single 200kg satellite can remove 6 large debris objects in approximately 200 days using a 5km tether. This is particularly useful since the cost of satellite development is directly proportional to the mass of the satellite due to launch costs. By reducing the weight by factor ten from the 2000kg variant, there could potentially be a small fleet of these satellites launched simultaneously to de-orbit debris from multiple orbits, which would increase your yearly active debris removal rate significantly compared to that of the other proposed technologies.

Recommendations for further research include: a full 3D field model of the earth's upper atmosphere to investigate plume divergence, investigation into CEX spacecraft charging as well as its effect on an emitted ion beam, possible beam-plasma instabilities with the earth's upper atmosphere, and a full systems analysis of the 200kg variant of the EDT+IBS system in order to determine accurate performance and cost metrics.

Works Referenced

- [1] ESA, "Detecting, Tracking and Imaging Space Debris," European Space Agency, 2002.
- [2] Air Force Space Command, "Space Situational Network," 2012. [Online]. Available: <http://www.onorbitwatch.com/briefing/space-situational-network>.
- [3] NASA, "Handbook 8719.14: Limiting Orbital Debris," National Aeronautics and Space Administration, Washington, 2008.
- [4] P. Krisko, "NASA's new orbital debris engineering model, ORDEM2010," NASA, Houston, 2010.
- [5] Parliamentary Office of Science and Technology, "Space Debris," *Postnote*, pp. 1-2, March 2010.
- [6] W. K. Stuckey, "Lessons Learned from the long duration exposure facility," Space and missile systems center air force materiel command, Los Angeles, 1993.
- [7] Donald J. Kessler, "Origin of orbital debris impacts on LDEF's trailing surfaces," NASA, Houston, Tx.
- [8] H. Klinkrad, *Space Debris: Models and risk analysis*, Darmstadt: Springer, 2006.
- [9] NASA Langley Research Center, "Impact Damage of LDEF Surfaces," 15 November 2011. [Online]. Available: http://setas-www.larc.nasa.gov/LDEF/MET_DEB/md_impact.html.
- [10] J. L. Hyde, E. L. Christiansen, D. M. Lear and T. G. Prior, "Overview Of Recent Enhancements To The Bumper-II Meteoroid and Orbital Debris Risk Assessment Tool," NASA, 2006.
- [11] D. J. Kessler, "Collisional Cascading: The limits of population growth in low earth orbit," *Advances in Space Research*, vol. 11, no. 12, pp. 63-66, 1991.

- [12] B. Iannotta, "Space.com," 2009. [Online]. Available: <http://www.space.com/5542-satellite-destroyed-space-collision.html>. [Accessed 2012].
- [13] T. Hanada, "Using NASA Standard Breakup Model to Describe Low-Velocity Impacts on Spacecraft," *Journal of Spacecraft and Rockets*, vol. 42, no. 5, pp. 859-864, 2005.
- [14] J.-C. Liou, "An Active debris removal parametric study for LEO environment remediation," *Advances in space research*, vol. 47, no. 11, pp. 1865-1876, 2011.
- [15] N. Johnson, "NASA's New Breakup Model of Evolve 4.0," *Advances in Space Research*, vol. 28, no. 9, pp. 1377-1384, 2001.
- [16] N. L. Johnson, "A sensitivity study of the effectiveness of active debris removal in LEO," NASA, Houston, 2007.
- [17] National Research Council, "Limiting Future Collision Risk to Spacecraft: An Assessment of NASA's Meteoroid and Orbital Debris Program," National Academies Press, Washington, 2011.
- [18] J. Campell, "Project ORION: Orbital Debris Removal Using Ground-Based Sensors and Lasers," NASA, 1996.
- [19] C. Bombardelli, "Ion Beam Shepherd for Contactless Space Debris Removal," *Journal of Guidance, Control and Dynamics*, vol. 34, no. 3, p. 13, 2011.
- [20] NRL, 2007, "NRL Developing Space "Tow Truck" Technology For Satellite Operations," 27 August 2007. [Online]. Available: <http://www.nrl.navy.mil/pao/pressRelease.php?Y=2007&R=47-07r>. [Accessed 2012].
- [21] C. Pardini, T. Hanada and P. H. Krisko, "Benefits and risks of using electrodynamic tether to de-orbit spacecraft," *Acta Astronautica*, vol. 64, no. 5-6, pp. 571-588, 2009.
- [22] Y. Ishige, S. Kawamoto and S. Kibe, "Study on electrodynamic tether system for space debris removal," *Acta Astronautica*, vol. 55, no. 11, pp. 917-929, 2004.
- [23] G. Ganguli, C. Crabtree, L. Rudakov and a. S. Chappie, "A concept for elimination of

small orbital debris," Plasma Physics Division, Naval Research Laboratory, Washington, 2011.

- [24] E. Stuhlinger, *Ion Propulsion or Space Flight*, New York: McGraw-Hill, 1964.
- [25] M. M. Castronuovo, "Active space debris removal - A preliminary mission analysis and design," *Acta Astronautica*, vol. 69, no. 9-10, pp. 848-859, 2011.
- [26] National Oceanic and Atmospheric Administration, "International Geomagnetic Reference Field," 2012. [Online]. Available: <http://www.ngdc.noaa.gov/IAGA/vmod/igrf.html>.
- [27] H. San, "ORBITAL MANEUVERING USING ELECTRODYNAMIC TETHERS," Air force institute of technology, Dayton, 2002.
- [28] A. F. Carlson, "OPTIMAL ORBIT MANEUVERS WITH ELECTRODYNAMIC TETHERS," Naval Postgraduate School, Monterey, 2006.
- [29] J. Burbach, "LEO Space Debris Removal Utilizing Electrodynamic Tethered Propulsion," Colorado University, Colorado, 2010.
- [30] M. Reyhanoglu, "Advanced Spacecraft Controls Project Report," Embry-Riddle Aeronautical University, Daytona Beach, 2010.
- [31] S. G. Tragesser and H. San, "Orbital Maneuvering with Electrodynamic Tethers," *Journal of Guidance, Control, and Dynamics*, vol. 26, no. 5, pp. 805-810, 2003.
- [32] C. Bombardelli, H. Urrutxua, M. Merino, E. Ahedo and J. Palaez, "Dynamics of ion-beam-propelled space debris," European Space Agency, Keplerlaan, 2011.
- [33] M. Merino, "Hypersonic Plasma Plume Expansion In Space," in *32nd International Electric Propulsion Conference*, Wiesbaden, 2011.
- [34] D. Parks and I. Katz, "A Preliminary Model of Ion beam Neutralization," AIAA, Princeton, NJ, 1979.

- [35] ESA, "Ariadna Call for Ideas: Ion Beam Shepherd for contactless debris removal," European Space Agency, 2011.
- [36] J. Wang, D. Brinza, R. Goldstein, J. Polk and M. Henry, "Deep Space One Investigations of Ion Propulsion Plasma Interactions: Overview and initial Results," 2001.
- [37] S. Roy, "Numerical Simulation of Ion Thruster Plume Backflow for Spacecraft Contamination Assessment," MIT, 1995.
- [38] J. Blandino, "Low energy sputter yields for diamond, carbon-carbon composite, and molybdenum subject to xenon ion bombardment," ELSEVIER, 2000.
- [39] C. Birdsall and A. Langdon, Plasma physics via computer simulations, Institute of Physics, 2005.
- [40] R. A. Treumann and W. Baumjohann, Advanced Space Plasma Physics, 1997.
- [41] D. Goebel and I. M. Katz, Fundamentals of Electric Propulsion: Ion and Hall Thrusters, 2009.
- [42] J. Rowe and A. T. Lin, "Simulation of the Beam-Plasma Instability in a Finite-Length System," University of Michigan, 1972.
- [43] B. Wie, Space Vehicle Dynamics and Control, Reston: American Institute of Aeronautics and Astronautics, 2008.
- [44] H. Schaub, "Incorporating secular drifts into the orbit element difference description of relative orbits," in *13th AAS/AIAA Space Flight Mechanics Meeting*, Ponce, 2003.
- [45] Astronautix, "Encyclopedia Astronautica," [Online]. Available: <http://www.astronautix.com/engines/mr106.htm>. [Accessed 8 May 2012].
- [46] X. Yang, W. Wang and H. Gao, "Limited-Thrust relative position holding for adjacent spacecraft with thruster nonlinearity," in *IEEE Conference on Decision and Control and European Control Conference (CDC-ECC)*, Orlando, 2011.

- [47] G. Shan and H. Yanhua, "Relative position control based on H8 robust control for spacecraft rendezvous final approach," in *Measuring Technology and Mechatronics Automation*, Shanghai, 2011.
- [48] L. I. J. Corsi, "Stability and Control of Electrodynamic Tethers for de-orbiting applications," *Acta Astronautica*, vol. 48, no. 5-12, pp. 491-501, 2001.